Doklady Physics, Vol. 49, No. 11, 2004, pp. 617–621. Translated from Doklady Akademii Nauk, Vol. 399, No. 2, 2004, pp. 180–184.

PHYSICS

Low-Frequency Noise and Impedance Spectral Characteristics of Solid-State Structures

I. V. Lebedev, I. N. Miroshnikova, and D. V. Chuprov

Presented by Academician Yu.V. Gulyaev April 23, 2004

Received April 29, 2004

Low-frequency noise is an important parameter allowing one to reveal and predict the quality and reliability of semiconductor electronic devices [1–3]. In recent years, many publications have been devoted to the problems of noise spectroscopy and the physical enigmas arising therein, corresponding international conferences being regularly arranged [1].

It is possible to note a similarity in the approaches used in the field of noise spectroscopy and conventional optical spectroscopy that has existed for a long time [4, 5]. This similarity is surprising, despite the sharp distinction in both the technical means used and frequency and wavelength ranges inherent in optical and noise spectra. Electric-current and voltage fluctuations observed at radio frequencies, and even in the infralow-frequency range (10^6–1 Hz and lower down to 10^{-5} Hz), are peculiar analogs of emission optical spectra.

One feature of noise-emission spectra is their very low intensity as compared to optical spectra. It is important to understand whether it is possible to reduce the difficulties associated with investigations of low-intensity noise?

It is known that absorption analysis based on studies of absorption spectra [5] is commonly used in the optical wavelength range alongside the emission spectral analysis that replaces and supplements the former. However, until now, the problem of the use of certain frequency characteristics, which are similar in a physical sense to the absorption spectra, has not been posed for the same purposes in the low-frequency range.

As we show below, the low-level low-frequency electric impedance measured on the input terminals of an object is such a frequency characteristic replacing the direct noise measurements.

It is reasonable to analyze all types of low-frequency spectra in radio-electronic devices in terms of classical single-mode electric circuits with lumped parameters. In the simplest case, the object under study is a linear electric two-terminal network. In terms of emission spectroscopy, it is a lumped noise-voltage or noise-current generator. In terms of absorption spectroscopy, the same object is a passive absorber, the impedance in the series representation of which can be written as $Z(f) = R_s(f) + iX_s(f)$. To reveal this impedance, it suffices to use a harmonic probing signal generated in the continuous mode by an independent generator with frequency f, which is scanned or discretely varied within the range of interest. Thus, the probing generator plays the role similar to that of an optical monochromator. The absorption-spectrum analyzer can be a bridge or other electric circuit measuring the values of $R_s(f)$ and $X_s(f)$ on the basis of Ohm's law, taken in its complex form.

Amplitudes U_m of the probing signal should be reasonably low so as to exclude nonlinear effects leading to modifications in the electric and thermodynamic parameters of the object. It is desirable that the value of U_m be lower than the thermal potential $U_T = kT/e$, which attains about 26 mV at the temperature T = 300 K. (Here, k is the Boltzmann constant and e is the elementary electric charge.) Nevertheless, the test-signal amplitude can exceed by several orders of magnitude the mean-square value of the intrinsic-noise voltage of the object in the frequency range being analyzed. By virtue of this fact, the conditions of realization of impedance absorption measurements are essentially facilitated compared to measurements of the generated noise.

The real part of the low-level (differential) impedance $Z(f)$ determined by the indicated method is phenomenologically caused by a joint action of all the types of dissipative processes that occur if a probing signal is imposed on the object. It is necessary to attribute to these processes those depending not only on the electrical conduction of a material (with allowance made for the concentration and mobility of all types of charge carriers), but also on all macroscopic and microscopic relaxation phenomena in the bulk and on the surfaces of the object.

We denote the spectral-density function of voltage fluctuations at the open poles of a two-terminal network under consideration as $S_U(f)$ (expressed in units

Moscow Power Institute (Technical University), ul. Krasnokazarmennaya 14, Moscow, 111250 Russia
e-mail: LebedevIV@mpei.ru

1028-3358/04/4911-0617$26.00

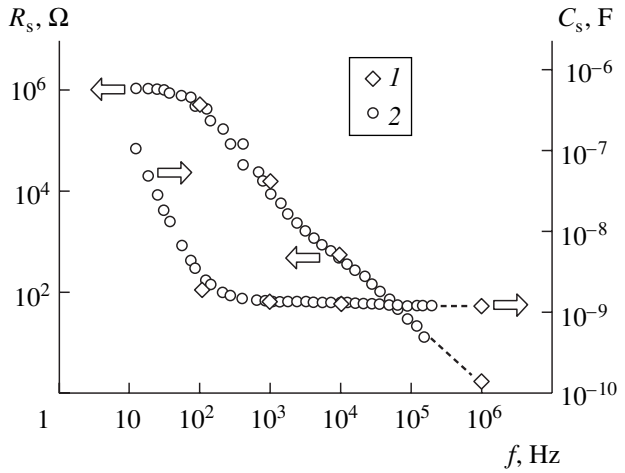

Fig. 1. Low-frequency impedance spectral characteristics $R_s(f)$ and $C_s(f)$ for sample 2 (2D213A diode) measured by (*1*) E7-14 and E7-12 devices and (*2*) ICP RAS device.

of V^2/Hz). Then, according to the Nyquist theorem [6], we assume that the ratio between the quantity $S_U(f)$ and the resistance $R_s(f)$ under the condition of thermodynamic equilibrium of the object is independent of both the frequency and the physical-body structure and equal to $4kT$, where T is the absolute temperature:

$$\frac{S_U(f)}{R_s(f)} = \text{const} = 4kT. \quad (1)$$

Equation (1) can be considered a similarity relation between the impedance-frequency spectra and noise spectra. There is a clear similarity between this dependence and Kirchhoff's law, which is well-known in thermodynamics and electrodynamics. This similarity implies the constancy of the ratio between the radiating and absorptive capacities of physical bodies irrespective of their nature under the given conditions in an arbitrarily wide wavelength range [7].

As was noted above, the resistance $R_s(f)$ entering into Eq. (1) phenomenologically describes all types of the dissipative processes proceeding in the two-terminal network under consideration. For this reason, in conditions of thermodynamic equilibrium, the thermal-fluctuation emission spectrum $S_U(f)$, being essentially similar to the spectrum $R_s(f)$, includes all real acting dissipative factors irrespective of their origin (including deep levels, surface states, etc.) to the same degree.

Thus, the measurement of the frequency dependence for the series resistance $R_s(f)$ at a fixed temperature T can serve as an alternative to direct measurements of the noise emission spectrum $S_U(f)$. Modern measuring electronic equipment opens up reasonably ample opportunities for such investigations.

Below, we give a brief description of the experiments aimed at the direct verification of these concepts.

Objects for the investigations are two-electrode structures differing in type of semiconductor material, in level and profile of doping, and in type of junctions. The impedance spectra were investigated mainly with E7-12 and E7-14 low-level immittance meters and a PC-based impedance meter–analyzer developed in the Institute of Control Problems (ICP), Russian Academy of Sciences (RAS) [8]. The sine-wave-signal generators and electronic units involved in the E7-14 and E7-12 devices make it possible to measure the impedance and admittance at discrete frequencies of 10^2, 10^3, 10^4, and 10^6 Hz with probing-signal amplitudes of 40 and 25 mV. The use of a measurement device of the ICP, RAS, considerably extended the potentialities of the experiment, owing to a step variation of the frequency within the limits of $10–2 \times 10^5$ Hz (the probing-generator frequency is determined from the expression $2 \times 10^6/N$ Hz, where N is an integer).

The major part of the measurements was performed at a temperature close to 300 K, although, in certain cases, we used liquid nitrogen (T = 77 K) for cooling the structures. No direct-current bias voltage was usually fed to the structures, but comparative experiments were also carried out with feeding direct and back bias.

The results of the impedance measurements using the measuring setup described in [9] were compared with the emission noise spectra for the same semiconductor structures. The setup involved a nanovoltmeter of the Unipan-273 type operating in the broadband mode with a preamplifier (having the input resistance of 10^8 Ω and the input capacitance of 2 pF). The nanovoltmeter was connected to a U7-1 broadband amplifier having a built-in low-frequency filter with discretely varied cut-off frequencies equal to 10, 10^2, 10^3, 10^4, and 10^5 Hz. The noise spectrum was processed and recorded by a computer with the use of a frequency–time Fourier series calculated by the algorithm of the fast Fourier transform. The spectral density of the noise-signal voltage represented in V^2/Hz units was detected within the frequency range $1–10^5$ Hz.

In Fig. 1, we show the typical results of measuring the low-level resistance for a 2D213A silicon rectifying diode. The direct-current bias voltage is equal to zero. Attention is drawn to the plateau and the abrupt rise (by more than five decimal orders of magnitude) of the resistance R_s with decreasing the frequency within the range between 1 MHz and 100 Hz. The capacitance C_s also increases not less sharply, the rise region of the characteristic $C_s(f)$ being shifted with respect to the characteristic $R_s(f)$ toward lower frequencies.

The extremely abrupt increase in the resistance R_s and capacitance C_s of the diode structure at low frequencies is of principal importance for the subsequent analysis. The indicated behavior of $C_s(f)$ and $R_s(f)$ curves is associated with neither an increase in the barrier capacitance within the low-frequency range nor

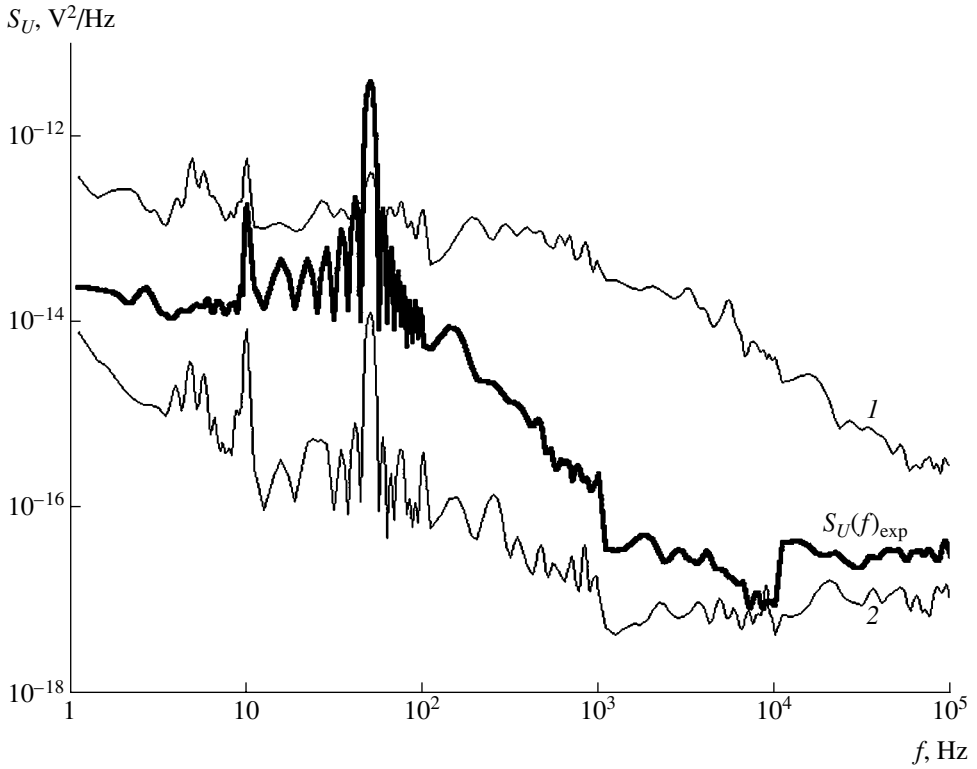

Fig. 2. Low-frequency noise spectrum $S_U(f)_{exp}$ for sample 2 (2D213A diode) measured by the setup described in [9] and the calibration noise spectra in (*1*) open-circuit and (*2*) short-circuit modes.

other physical anomalies. As shown in [10], these are frequency dependences that are predicted with allowance made for the existence of two discrete spatial regions in a solid-state structure: the space-charge region and quasi-neutral base region. The same impedance spectra are generally intrinsic not only to semiconductor diodes, but also to other two-terminal networks with macroscopic electrical or technological lamination.

The results of measurements of the noise spectrum $S_U(f)_{exp}$ for the same Si-diode sample are shown in Fig. 2. To illustrate the features of the used measuring setup [9] and the effect of external factors, the calibrated noise spectra are presented in the same figure. These spectra were detected in the case of open (no-load) and short-circuited terminals to which the object under study was connected. It is seen that the fluctuation-voltage spectrum of the diode has a pronounced ascending portion within the frequency region 100–10^5 Hz, which is similar to the rise in the impedance spectrum $R_s(f)$ shown in Fig. 1.

The quantitative comparison between the measured spectra shown in Figs. 1 and 2 seems to be the most interesting. For improving the accuracy of this comparison, it is necessary to consider the inevitable distinctions in the measurement conditions for the $S_U(f)$ and $R_s(f)$ spectra in the case of the same object under investigation and identical temperatures. The equipment used in the impedance measurements detects the true values of the resistance and capacitance with a small relative error (usually lower than 0.5–1%) and is virtually free of effects of external fields. Therefore, the values of $S_U(f)$ [determined from Eq. (1) on the basis of the measured spectrum $R_s(f)$ after its multiplication by the factor $4kT$] correspond to the noise spectrum of the object under consideration for the ideal disconnection of its poles. At the same time, the experimentally observed spectrum $S_U(f)_{exp}$ is affected by both extraneous electric and magnetic fields and the intrinsic noise of the measuring setup, as well as by its finite input resistance. At certain frequencies, the latter can be comparable to the object resistance R_s. It should also allow for the effects of the input shunting capacitance and the connecting cable. The latter capacitance can attain 100 pF at a cable length of about 1 m. These factors should be taken into account by adding the frequency-dependent term $F(f)$ into Eq. (1). The calculation of this term was performed using the spectra $S_U(f)$ obtained in the open-circuit (no-load) and short-circuit regimes of the object (see Fig. 2) on the basis of the principle of superposition of mean-square values for noise voltages and currents [11].

In Fig. 3, open circles and rhombuses repeatedly show the results of the above measurements of the impedance spectrum $R_s(f)$ (Fig. 1) multiplied by the factor of $4kT$. The plot obtained in such a manner satis-

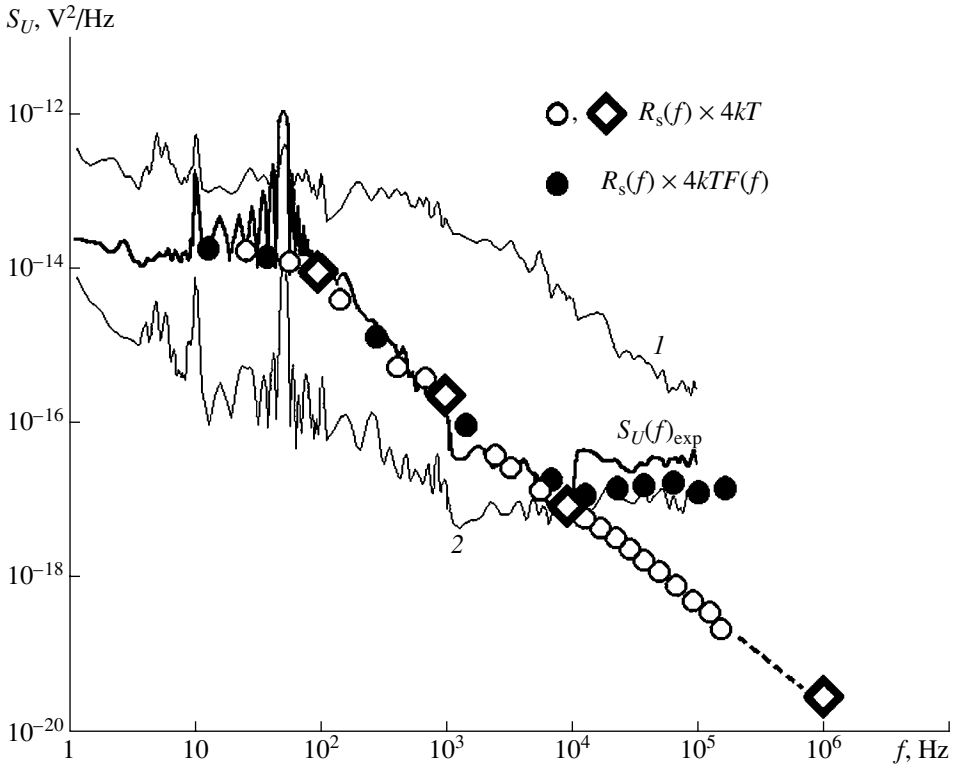

Fig. 3. Comparison of the measured noise spectrum shown in Fig. 2 with the noise spectrum of the same diode sample, which was obtained on the basis of the impedance-measurement results (Fig. 1) using similarity relation (1). Closed points are plotted with allowance made for the effect of both the intrinsic noise of the measuring setup and the connecting-cable capacitance. For *1* and *2* see Fig. 2.

fies similarity relation (1) and represents the voltage-fluctuation spectrum that would be observed on the open poles of the diode under consideration, provided that an ideal voltmeter was used. Closed circles in Fig. 3 show the calculated adjustment using the correction factor $F(f)$. An effect of external circuits and the intrinsic noise of the measuring setup in the case under consideration manifests itself at frequencies above 10 kHz. Here, this renders it impossible to measure the noise with a spectral density below, approximately, 10^{-17} V^2/Hz, although the spectrum $S_U(f)$ of the given diode attains at least about 10^{-20} V^2/Hz, the factor $F(f)$ becoming distinct from unity.

We impose on this plot the measured noise spectrum $S_U(f)_{exp}$ from the same diode sample as shown in Fig. 2. It is seen that, except for the portion close to the industrial frequency of 50 Hz, this spectrum virtually coincides with the spectrum $S_U(f)$ recalculated from the impedance spectrum $R_s(f)$. Our attention is engaged by the fact that, for $f < 10^4$ Hz, the coincidence of the spectra exists even without the use of the calculated correction. In the region $f > 10^4$ Hz, the experimental spectrum is distorted more and more strongly and approaches the plot for the short-circuit noise.

The same close quantitative correspondence of impedance and noise spectra has been established in experiments with other types of silicon structures and cooled InSb-based photoresistances without an external bias. Alongside investigations of single structure samples, we performed measurements with sets of devices, each being up to 30 units. The results have shown that the sensitivity of impedance measurements to the parameter spread is not worse than the sensitivity of noise tests.

Thus, the experiments carried out in the framework of the present study confirm the qualitative similarity and numerical correspondence of the independently measured noise spectra $S_U(f)$ and low-level impedance spectra $R_s(f)$ determined from Eq. (1) without an external bias and under conditions of thermodynamic equilibrium. This conformity manifests itself on plateau segments that resemble white noise and in regions of excess noise in which the fluctuation density $S_U(f)$ increases by five to six orders of magnitude with decreasing frequency.

The spread of parameters from sample to sample for the same type of solid-state structures, which is efficiently revealed according to distinctions in levels of intrinsic low-frequency noise [1–3], is unambiguously described by a variance of the resistances $R_s(f)$. For this reason, the impedance low-level measurements can be considered as a source of information that is compa-

rable to—and, for a number of attributes, even surpasses—the noise measurements.

REFERENCES

1. L. K. J. Vandamme, *XVII Int. Conf. on Noise and Fluct.* (Prague, 2003), p. 735.
2. V. S. Pryanikov, *Forecasting of Failures in Semiconductor Devices* (Énergiya, Moscow, 1978).
3. E. Ya. Finkel'shteĭn, *Maintenance of Reliability of Elements by Parametric-Control Methods* (Zinatne, Riga, 1979).
4. G. S. Landsberg, *Optics* (Nauka, Moscow, 1976).
5. M. A. El'yashevich, *Atomic and Molecular Spectroscopy* (Editorial URSS, Moscow, 2000).
6. A. van der Ziel, *Noise in Solid-State Devices and Structures* (Wiley, New York, 1986).
7. M. L. Levin and S. M. Rytov, *Theory of Equilibrium Thermal Fluctuations in Electrodynamics* (Nauka, Moscow, 1967).
8. Yu. R. Gamalov, D. A. Bobylev, and V. J. Kneller, Izm. Tekh., No. 6, 56 (1996).
9. S. A. Sokolik, A. M. Gulyaev, and I. N. Miroshnikova, Izm. Tekh., No. 1, 57 (1997).
10. I. V. Lebedev and M. Yu. Polyakov, Dokl. Akad. Nauk **368**, 181 (1999) [Dokl. Phys. **44**, 592 (1999)].
11. V. Zhalud and V. N. Kuleshov, *Noise in Semiconductor Devices* (Sov. Radio, Moscow, 1977).

Translated by V. Bukhanov

Doklady Physics, Vol. 49, No. 11, 2004, pp. 622–624. Translated from Doklady Akademii Nauk, Vol. 399, No. 2, 2004, pp. 185–187.

PHYSICS

Direct Observation of Short-Range-Order Anisotropy in $Fe_{1-x}Si_x$ (x = 0.05–0.06) Single Crystals with Induced Magnetic Anisotropy

B. K. Sokolov*, Yu. P. Chernenkov, V. A. Lukshina*, V. I. Fedorov**, and N. V. Ershov***

Presented by Academician V.M. Schastlivtsev May 14, 2004

Received June 2, 2004

Iron–silicon alloys with high iron contents are the basis for the production of electrical-sheet steels. An improvement in their magnetic properties is attained by thermomagnetic or thermomechanical treatment. As a result, a uniaxial magnetic anisotropy appears that has an axis coinciding with an easy-magnetization axis. In this direction, a decrease in the coercive force occurs, the remanent induction increases, and the hysteresis loop becomes more rectangular [1]. To explain the induced uniaxial anisotropy in substitutional solid solutions as a result of thermomagnetic treatment, the theory of directed ordering of atoms was developed about 50 years ago [2–4].

According to this theory, the axial orientation of local properties in substitutional solid solutions with a cubic lattice can be caused by uniaxial defects representing pairs of identical atoms predominantly oriented along one of crystallographic direction. At temperatures sufficient for diffusion, but lower than the Curie point T_C, the atomic pairs occupy the lattice sites, providing a minimal angle between the pair axis and the magnetization vector of a sample. The directional ordering after cooling to room temperature is frozen by virtue of the low diffusion mobility of the atoms. Uniaxial anisotropy appears with an axis coinciding with the direction of the external magnetic field acting in the process of annealing.

This theory excellently explained the occurrence and temperature stability of uniaxial magnetic anisotropy. In addition, it has a number of consequences that have been repeatedly confirmed in experiments, for example, that no pair ordering occurs in pure metals and alloys with an isotropic long-range order and that the treatment temperature should be lower than T_C but sufficient for diffusion of atoms. Quenching from temperature higher than T_C or annealing in a rotating magnetic field must suppress the directional ordering.

The atomic structure and properties of soft magnetic alloys based on iron were intensely investigated for many years [5–10]. However, there were no experimental studies that would either prove or rule out the theory of directed ordering. Therefore, we have formulated the task of confirming or ruling out by direct structural investigations the existence of uniaxial anisotropic defects in bcc single crystals of a soft magnetic iron–silicon alloy having, as a result of treatment, an induced magnetic anisotropy.

Single-crystalline samples in the form of thin disks with the (100) plane cubic orientation were cut from a single crystal grown by the Bridgman method. Samples with the (110) Goss' orientation were cut from grains of sheet industrial steel.

The samples were treated to induce or suppress magnetic anisotropy in the entire volume. Under annealing and cooling in a permanent magnetic field, i.e., under thermomagnetic treatment (TMT), one of the easy-magnetization axes lying in the sample plane (namely, the [001] axis) was isolated in a sample with cubic orientation, and a magnetically isotropic state was obtained by quenching at a temperature of 800°C. Thermomechanical treatment (TMechT) with loading applied along the easy-magnetization direction increased the magnetic anisotropy in the [001] direction, while transverse loading maximally destroyed the anisotropy. The efficiency of the treatment performed was estimated according to both the domain structure and the shape of the hysteresis loops [11]. In samples with a cubic orientation, both magnetic anisotropy along one of the [001] easy-magnetization axes and an isotropic state were obtained after quenching. In samples with Goss' orientation, maximal anisotropy after

* *Institute of Metal Physics, Ural Division, Russian Academy of Sciences, ul. S. Kovalevskoĭ 18, Yekaterinburg, 620219 Russia*
e-mail: sokolov@imp.uran.ru

** *Konstantinov Institute of Nuclear Physics, Russian Academy of Sciences, Gatchina, Leningrad oblast, 188300 Russia*
e-mail: yucher@mail.pnpi.spb.ru

1028-3358/04/4911-0622$26.00 © 2004 MAIK "Nauka/Interperiodica"

TMT and TMechT was observed along the [001] easy-magnetization direction, whereas minimal anisotropy was detected after application of a transverse alternating magnetic field or mechanical loading.

X-ray diffraction structure measurements were carried out with a laboratory diffractometer equipped with a four-circle goniometer. The long-range-order structure and the quality of single-crystal samples were determined from analysis of Bragg-reflection profiles, and the local atomic structure was identified from a weak diffusive scattering measured between the principal reflections. To separate static and dynamic structural features, measurements were performed at room temperature and at a temperature of 190 K. It was shown that diffusive planes and rods that occur due to phonon scattering become several times less intense at low temperatures.

The profiles of the basic reflections have half-widths close to the instrumental width. This fact indicates that the bcc lattice is virtually close to an ideal one. No dependence on the type of the action or direction of its application was observed. The weak superstructural diffuse peaks testify to the presence of *B*2-type orderings. The absence of peaks with semi-integer indices points to the absence of the DO_3 phase. The analysis of the profile of superstructural reflections showed that its half-width was narrower in the magnetic-anisotropy direction and broader in the transverse direction. Hence, the average ordering-region size [12] is larger in the anisotropy direction and smaller across it; i.e., the size distribution of clusters with the *B*2-type order has an anisotropic shape (Table 1). Most likely, in a sample with magnetic anisotropy, the longitudinal extension of clusters is formed by pairs of *B*2 cells oriented predominantly along the [001] axis. In a sample with isotropic magnetic properties, we observed equiprobable distribution of pairs of cells after quenching, at least, along the [100] and [001] directions lying in the disk plane.

In samples with the Goss' orientation of axes, both the magnetic anisotropy and the extension of clusters along the [001] axis increase along the easy-magnetization axis after TMT or TmechT, accompanied by the application of a permanent magnetic field or loading (Table 2). The extension of clusters is likely associated with both reorientation of *B*2-cell pairs and chain formation.

Thus, we were pioneers in discovering a stable correlation of the magnetic-anisotropy direction and the anisotropy of the size distribution for regions with *B*2 short-range order.

The superstructural peaks are shifted from calculated positions toward smaller diffraction angles: $h = 2.84$ and $l = 2.87$ instead of 3 for the (300) and (003) coordinates, and $l = 0.94$–0.96 instead of 1 for the (001) coordinate. This implies that the interatomic distances are increased compared to the distances in the remaining lattice, which can be explained by the local extension of the lattice around cells containing silicon atoms (the *B*2-cell size is 3–4% smaller than that in the remaining bcc lattice).

Table 1. Sizes of clusters with *B*2 ordering in Fe–4.8%Si single crystals with cubic orientation

Thermal treatment	Direction	Size, nm	Error, nm
In a permanent magnetic field ∥ (003)	(100)	0.53	±0.05
	(001)	0.69	±0.06
Rapid quenching at 400 °C s^{-1}	(100)	0.72	±0.09
	(001)	0.70	±0.07

Table 2. Sizes of clusters along the [001] direction with *B*2 ordering in Fe–5.9%Si single crystals with Goss' orientation

Thermal treatment	Size, nm	Error, nm
In a permanent field ∥ (001)	1.02	±0.04
In an alternating field ⊥ (001)	0.72	±0.02
Under loading ∥ (001)	0.91	±0.10
Under loading ⊥ (001)	0.58	±0.06

In [13], we qualitatively substantiated for the first time shifts of superstructural peaks on the basis of estimates of various contributions to the structural factor. Later, using model calculations, we showed that the clusters represented a chain of predominantly two *B*2 cells oriented along one of the easy-magnetization axes and the lattice-extension region around them. As a result of thermal treatment, they are distributed predominantly along the direction of the applied field or load, thereby forming and stabilizing anisotropic magnetic properties. In other cases (without load and field, or after quenching), the clusters are equiprobably distributed along the directions of the ⟨100⟩ type.

Axial anisotropy of a short-range order in samples with magnetic anisotropy induced along one of the easy-magnetization axes, which was observed using the X-ray diffraction method, is experimental confirmation of the validity of the directed-ordering theory.

ACKNOWLEDGMENTS

This work was supported by the Russian Foundation for Basic Research (project nos. 03-02-16185 and 02-02-16981) and by the Division of Physical Sciences (program no. 5: "New Materials and Structures").

REFERENCES

1. R. M. Bozorth, *Ferromagnetism* (D. Van Nostrand, Toronto, 1951; Inostr. Lit., Moscow, 1956).
2. L. J. Nèel, J. Phys. Radiat. **15** (4), 225 (1954).
3. S. Taniguchi and M. Yamamoto, Sci. Rep. RITU **6**, 330 (1954).

4. S. Taniguchi, Sci. Rep. RITU **A7**, 269 (1955).
5. D. Mainhardt and O. Krisement, Arch. Eisenhüttenw. **36** (4), 293 (1965).
6. E. N. Vlasova and B. V. Molotilov, in *Precision Alloys* (Metallurgiya, Moscow, 1979), Vol. 5, p. 71.
7. K. Nilfrich, W. Kolker, W. Petry, *et al.*, Acta Metall. Mater. **42** (3), 743 (1994).
8. I. A. Zaĭkova, I. E. Startseva, and B. N. Filippov, *Domain Structure and Magnetic Properties of Electrical-Sheet Steels* (Nauka, Moscow, 1992).
9. I. B. Kekalo and B. A. Samarin, *Physical Metallurgy of Precision Alloys. Alloys with Special Magnetic Properties* (Metallurgiya, Moscow, 1989).
10. V. V. Gubernatorov and T. S. Sycheva, Dokl. Akad. Nauk **382**, 332 (2002) [Dokl. Phys. **47**, 64 (2002)].
11. I. E. Startseva, V. V. Shulika, and Ya. S. Shur, BRAS. Phys. **36**, 1597 (1972).
12. B. E. Warren, *X-Ray Diffraction* (Mass, New York, 1969).
13. Yu. P. Chernenkov, V. I. Fedorov, V. A. Lukshina, *et al.*, J. Magn. Magn. Mater. **254**/**255**, 346 (2003).

Translated by V. Bukhanov

Doklady Physics, Vol. 49, No. 11, 2004, pp. 625–629. Translated from Doklady Akademii Nauk, Vol. 399, No. 3, 2004, pp. 325–329.

PHYSICS

Orientation of a Hydrogen Atom Excited by an Electron Impact near Threshold

A. V. Demura*, G. V. Demchenko, and G. V. Sholin

Presented by Academician V.D. Rusanov May 28, 2004

Received June 2, 2004

1. INTRODUCTION

Further development of methods of plasma polarization spectroscopy [1, 2] is one of the urgent trends in current investigations in plasma physics. Indeed, the polarization properties of bright-line and continuous radiation carry information on both the anisotropy of the velocity distribution function of charged particles and electric and magnetic fields in a plasma [1–3]. When there is a separate direction in the plasma, the degree and sign of polarization depend primarily on the type of observed atomic transition and, e.g., on the type of the anisotropy of the velocity distribution function of charged particles and energy.

In particular, polarization of radiation arises when spectral lines are excited by an electron impact [1–4]. In this case, the observed polarization depends nonmonotonically on the velocity of beam electrons, reaching a maximum for an energy of only several electron volts above the excitation threshold [4]. Since the simplest first Born approximation is inapplicable in this energy range and does not provide satisfactory results [2, 4–6], fairly accurate calculation methods are necessary to describe this mechanism of causing the polarization of spectral lines, which is important for the plasma.

Various schemes of strong coupling methods in the theory of electron–atom collisions have been proposed and developed to describe this energy range. However, their realization often requires laborious computations [2, 3, 5–12]. At the same time, to provide a theoretical basis for plasma polarization spectroscopy, it is necessary to develop algorithms that do not require long computation time and provide rapid analysis of vast amounts of experimental data [1, 2].

In this paper, we propose a strong coupling scheme that is based on the variable-phase method [13] and provides a fast and effective algorithm for calculating near-threshold cross sections for the electron-impact excitation of atoms [2, 3, 5–12]. To illustrate this approach, we consider the problem of the electron-impact excitation of a hydrogen atom to the first excited level. As is known, the first formulations of the strong-coupling method [5] were tested by solving in particular this problem. Although neutral hydrogen is the simplest atomic target, this problem has important physical features associated with the presence of the constant dipole moment of the exited states of the hydrogen atom. This property of the excited states of the hydrogen atom is responsible for the linear Stark effect in electric fields [14]. As has been mentioned previously [7, 8], this gives rise to a peculiar momentum dependence of near-threshold excitation cross sections. In this work, it was shown that the existence of the dipole moment of an excited state of the hydrogen atom leads to the orientation of the atom in the electric field of the scattered electron near the excitation threshold.

2. STRONG COUPLING EQUATIONS

The Schrödinger equation for the electron scattering on the hydrogen atom in the c.m.s. in atomic units has the form [1–15]

$$\left[\Delta_{\mathbf{r}} + \Delta_{\mathbf{R}} + k_0^2 - \lambda_0^2 + \frac{2}{r} + \frac{2}{R} - \frac{2}{|\mathbf{r}-\mathbf{R}|}\right]\Psi(\mathbf{r},\mathbf{R}) = 0. \quad (1)$$

Here, $\mathbf{r}$ and $\mathbf{R}$ are the radius vectors of the atomic and incident electrons, respectively; $\Delta_{\mathbf{r}}$ and $\Delta_{\mathbf{R}}$ are the Laplacians with respect to the coordinates of the atomic and incident electrons, respectively; $\frac{\lambda_0^2}{2}$ is the energy of the bound state of the atomic electron; $\frac{k_0^2}{2}$ is the kinetic energy of the incident electron; and $\Psi(\mathbf{r},\mathbf{R})$ is the total wave function of the two-electron system. Equation (1) does not include relativistic corrections [14].

Institute of Hydrogen Energy and Plasma Technology, Russian Research Centre Kurchatov Institute, pl. Akademika Kurchatova 1, Moscow, 123182 Russia

** e-mail: alexander.demura@hepti.kiae.ru*

1028-3358/04/4911-0625$26.00 © 2004 MAIK "Nauka/Interperiodica"

Disregarding exchange, one can represent the total wave function of the system as the atomic-state expansion [5]

$$\Psi(\mathbf{r}, \mathbf{R}) = \sum_p \varphi_p(\mathbf{r})\psi_p(\mathbf{R}), \tag{2}$$

where $\psi_p(\mathbf{R})$ is the wave function of the incident electron, and the wave function $\varphi_p(\mathbf{r})$ of the atomic electron with energy $-\frac{\lambda_p^2}{2}$ satisfies the equation

$$\left[\Delta_\mathbf{r} - \lambda_p^2 + \frac{2}{r}\right]\varphi_p(\mathbf{r}) = 0. \tag{3}$$

Expanding $\psi_p(\mathbf{R})$ in the spherical functions

$$\psi_p(\mathbf{R}) = \sum_{l_i, m_i} \frac{1}{R}\chi_{pl_im_i}(R)Y_{l_im_i}\left(\frac{\mathbf{R}}{R}\right), \tag{4}$$

where l_i and m_i are the orbital angular momentum of the incident electron and its projection, respectively, one obtains the following set of strong-coupling equations for the radial wave functions $\chi_{pl_im_i}(R)$ (see, e.g., [5]):

$$\left[\frac{d^2}{dR^2} - \frac{l_i(l_i+1)}{R^2} + k_p^2\right]\chi_{pl_im_i}(R) = \sum_{q, l_f, m_f} U_{pl_im_i}^{ql_fm_f}(R)\chi_{ql_fm_f}(R). \tag{5}$$

In the representation of the conserving total angular momentum L of the system of the atomic and incident electrons, this set takes the form [5]

$$\left[\frac{d^2}{dR^2} - \frac{l_i(l_i+1)}{R^2} + k_p^2\right]{}^L\chi_{n_pl_pl_i}(R) = \sum_{n_q, l_q, l_f} {}^L U_{n_ql_ql_f}^{n_pl_pl_i}(R)\,{}^L\chi_{n_ql_ql_f}(R), \tag{6}$$

where n_p, l_p, and m_p are the principal quantum number, orbital angular momentum, and projection of the orbital angular momentum of the atomic electron, respectively.

Thus, to solve the problem under consideration, one should solve the set of strong-coupling equations with given boundary conditions at infinity and determine the S matrix and, then, the cross sections [5].

3. VARIABLE-PHASE METHOD

It is convenient to solve the strong-coupling equations by the variable-phase method, which enables one to transform equations for radial wave functions to equations for the S matrix [13]. Indeed, the asymptotic behavior of the solution of system (6) at infinity is related to the real elements of the reactance matrix K as

$$\chi_a(R) \to \sum_b y_b(R)\delta_{ab} - \sum_b z_b(R)K_{ab}. \tag{7}$$

Here, $y_b(R)$ and $z_b(R)$ are the linearly independent solutions of set (6) in the absence of the interaction potential $U_a^b(R)$ and indices a and b denote the set of quantum numbers determining a certain scattering channel in Eqs. (6). The reactance matrix K can be expressed in terms of the S matrix by the known transformation [13].

Then, the reactance matrix and S matrix are determined in the variable-phase method from the equations [13]

$$\frac{d\mathbf{K}(R)}{dR} = -[\mathbf{y}(R) - \mathbf{K}(R)\mathbf{z}(R)]\mathbf{U}(R)[\mathbf{y}(R) - \mathbf{z}(R)\mathbf{K}(R)], \quad \mathbf{K}(0) = 0; \tag{8}$$

$$\frac{d\mathbf{S}(R)}{dR} = -\frac{i}{2}\{[\mathbf{y}(R) - i\mathbf{z}(R)] + \mathbf{S}(R)[\mathbf{y}(R) + i\mathbf{z}(R)]\}\mathbf{U}(R) \times \{[\mathbf{y}(R) - i\mathbf{z}(R)] + [\mathbf{y}(R) + i\mathbf{z}(R)]\mathbf{S}(R)\}, \quad \mathbf{S}(0) = 1. \tag{9}$$

Here, $\mathbf{y}(R)$ and $\mathbf{z}(R)$ are the diagonal matrices of the linearly independent solutions of Eqs. (6) in the absence of the interaction potential $U_a^b(R)$ and the matrices $\mathbf{K}(R)$ and $\mathbf{S}(R)$ are the reactance matrix and S matrix, respectively, for the truncated potential $\mathbf{U}(R')\theta(R - R')$. Thus, the basic advantage of the variable-phase method is the transition from the calculation of wave functions to the calculation of the reactance matrix and S matrix, which are directly related to physical observables.

4. NUMERICAL CALCULATIONS

By the variable-phase method, the S matrix was calculated in the basis of the atomic states $1s$–$2s$–$2p$. The differential cross sections for electron scattering are expressed as [5]

$$\frac{d\sigma_{n_pl_pm_p}^{n_ql_qm_q}}{do} = \frac{4\pi^2}{k_p^2} \times \left|\sum_{l_i, m_i, l_f, m_f} Y_{l_im_i}^*\left(\frac{\mathbf{k}_p}{k_p}\right)Y_{l_fm_f}\left(\frac{\mathbf{k}_q}{k_q}\right)i^{l_i - l_f}T_{n_pl_pm_pl_im_i}^{n_ql_qm_ql_fm_f}\right|^2 \tag{10}$$

in terms of the transition probability matrix T, which is related to the S matrix by the known expression

$$T_{n_pl_pm_pl_im_i}^{n_ql_qm_ql_fm_f} = S_{n_pl_pm_pl_im_i}^{n_ql_qm_ql_fm_f} - 1. \tag{11}$$

Table

k_p	L	${}^L\sigma_{10L}^{20L}$, 1*s*–2*s*		${}^L\sigma_{10L}^{21L+1}$, 1*s*–2*p*		${}^L\sigma_{10L}^{21L-1}$, 1*s*–2*p*	
0.9	0	0.222	0.220917	0.157	0.157356	–	
	1	0.080	0.0789325	0.029	0.0285163	0.366	0.367683
	2	0.321	0.322354	0.055	0.0558210	0.573	0.571146
	3	0.007	0.00720635	0.0006	0.000609303	0.024	0.0238816
	4	0.0003	0.000259319	0.00001	1.32063(–5)	0.001	0.00133054
1.0	0	0.168	0.168277	0.100	0.100026	–	
	1	0.145	0.142817	0.145	0.144492	0.142	0.145180
	2	0.157	0.157611	0.051	0.0519812	0.755	0.753796
	3	0.048	0.048530	0.005	0.00524181	0.212	0.211887
	4	0.008	0.008266	0.0005	0.000479245	0.048	0.047540
1.5	0	0.025	0.025004	0.037	0.0373480	–	
	1	0.086	0.085876	0.018	0.0186089	0.014	0.014688
	2	0.020	0.020010	0.003	0.00300071	0.163	0.163139
	3	0.007	0.006701	0.007	0.0074267	0.247	0.247739
	4	0.011	0.011207	0.007	0.00707383	0.221	0.221109
	5	0.011	0.010597	0.004	0.00424686	0.163	0.163174
	6	0.007	0.007474	0.002	0.0021752	0.113	0.112280
2.0	0	0.010	0.010168	0.010	0.010537	–	
	1	0.038	0.037741	0.004	0.003646	0.003	0.003194
	2	0.025	0.025426	0.0003	0.000322	0.038	0.038412
	3	0.011	0.010711	0.0025	0.002473	0.080	0.080418
	4	0.005	0.004591	0.005	0.005019	0.104	0.104203
	5	0.003	0.003357	0.006	0.005697	0.108	0.108234
	6	0.003	0.003308	0.005	0.004987	0.100	0.100079

Here, indices p and q specify the initial and final states of the atomic electron, respectively, and indices i and f specify the initial and final states of the scattered electron, respectively.

The integrated partial cross section is determined by integrating over the scattering angles do, summing over the projections of the angular momentum of final states, and averaging over the initial states:

$$ {}^L\sigma_{n_p l_p l_i}^{n_q l_q l_f} = \frac{\pi}{k_p^2}\frac{2L+1}{2l_p+1}\left|{}^L T_{n_p l_p l_i}^{n_q l_q l_f}\right|^2, \quad (12) $$

$$ {}^L\sigma_{n_p l_p}^{n_q l_q} = \sum_{l_i, l_f} {}^L\sigma_{n_p l_p l_i}^{n_q l_q l_f}. \quad (13) $$

The table shows partial cross sections calculated for various orbital angular momenta L of the system and various electron velocities k_p in comparison with (left columns) data taken from [15]. As is seen, the results differ by less than 10%. Orbital angular momenta equal to and less than two make the dominant contribution to the inelastic scattering cross section near the threshold. Indeed, the contributions from higher orbital angular momenta are immaterial, because the strong dipole attraction of the hydrogen atom is compensated by the centrifugal potential:

$$ \max_{n_1, n_2}\frac{3}{2}n(n_1 - n_2) = \frac{3}{2}n(n-1) \le \frac{1}{2}L_{\max}(L_{\max}+1). \quad (14) $$

Therefore, $L_{\max} = 2$ for $n = 2$. Figure 1 shows the integrated partial cross sections for 1*s*–2*s* and 1*s*–2*p* excitations for $L = 0$–6.

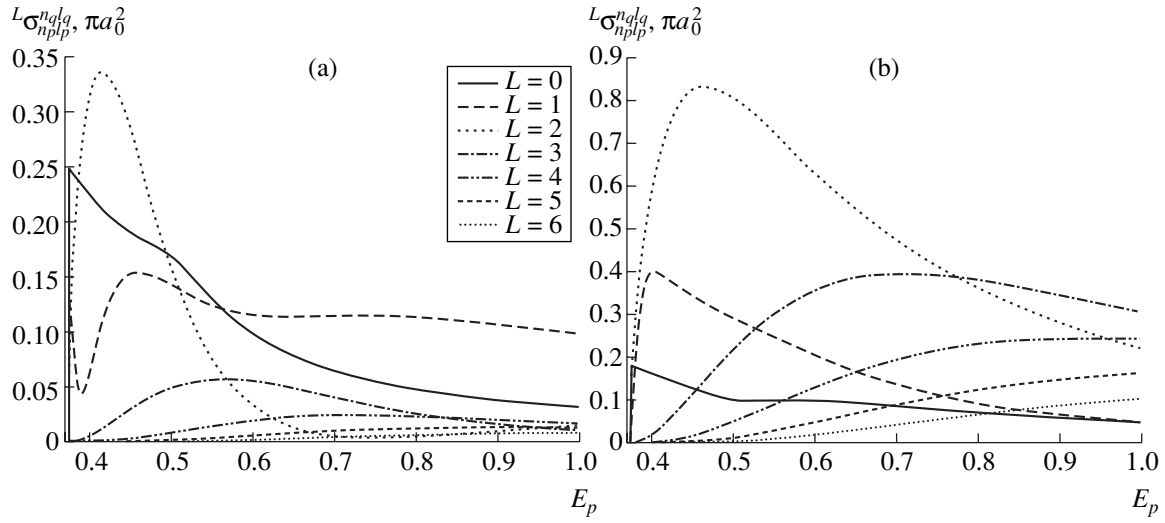

Fig. 1. Partial cross sections for the (a) 1*s*–2*s* and (b) 1*s*–2*p* electron-impact excitations of the hydrogen atom.

Let us consider the parabolic quantization of the atom along the momentum of the outgoing electron. In this case, the total cross section takes the form

$$ {}_F\sigma^{n_{1q}n_{2q}m_q}_{n_{1p}n_{2p}m_p} = \frac{\pi}{k^2_{p l_i, m_i}} \sum \left| \sum_{l_f} i^{-l_f} \sqrt{2l_f + 1}\, T^{n_{1p}n_{2p}m_q l_f 0}_{n_{1p}n_{2p}m_p l_i m_i} \right|^2, \quad (15) $$

where the subscript F means quantization along the momentum of the outgoing electron. Figure 2 shows the calculated total cross section for excitation to states $n_q = 2$ for the indicated quantization of the atom.

As is seen, the cross section for the excitation of the parabolic atomic state with $n_{1q} = 1$ and $n_{2q} = m_q = 0$ dominates in the near-threshold region due to the presence of the attractive potential in this state. The cross section for the atomic state with a repulsive potential is minimal.

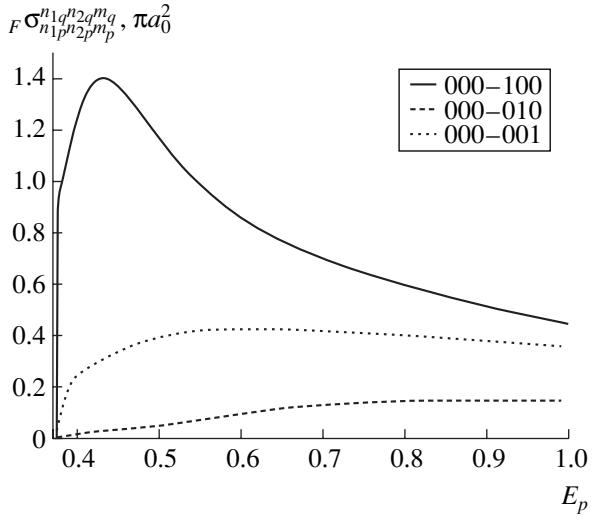

Fig. 2. Partial cross sections for the electron-impact excitation of the hydrogen atom from the ground state with $n_p = 1$ to the parabolic state with $n_q = 2$ and quantization along the final electron momentum.

5. CONCLUSIONS

A new algorithm for solving strong coupling equations, which is based on the variable-phase method [13], has been proposed and realized for calculating cross sections for electron-impact excitation of a hydrogen atom. The advantage of this algorithm is that it deals directly with the *S* matrix and significantly simplifies the numerical procedure and its analysis. It has been shown that orbital angular momenta equal to and less than two make the dominant contribution to the inelastic scattering cross section near the excitation threshold for $n = 2$. Cross sections tend toward a constant when approaching threshold $k_q \longrightarrow 0$. This anomalous behavior of the cross section is associated with the linear Stark effect [7]. The dipole moment of the atom is oriented along the momentum of the outgoing electron, because the states with attractive and repulsive interactions of the outgoing electron with the atom make the maximum and minimum contributions, respectively, to the total excitation cross section near the threshold.

ACKNOWLEDGMENTS

We are grateful to H.E. Saraph for support and to S.Ya. Umanskiĭ for useful advice and discussions.

REFERENCES

1. T. Fujimoto and S. A. Kazantsev, Plasma Phys. Controlled Fusion **39**, 1267 (1997).
2. N. Andersen and K. Bartschat, *Polarization, Alignment and Orientation in Atomic Collisions* (Springer, New York, 2001).

3. E. Haug, Sol. Phys. **71**, 77 (1981).
4. J. K. James, J. A. Slevin, D. Dziczek, *et al.*, Phys. Rev. A **57**, 1787 (1998).
5. I. C. Percival and M. J. Seaton, Proc. Cambridge Philos. Soc. **53**, 654 (1957).
6. M. J. Seaton, Proc. Roy. Soc. **77**, 174 (1961).
7. M. Gaĭlitis and R. Damburg, Zh. Éksp. Teor. Fiz. **44**, 1644 (1963) [Sov. Phys. JETP **17**, 869 (1963)].
8. M. Gailitis and R. Damburg, Proc. Phys. Soc. **82**, 192 (1963).
9. P. G. Burke and M. J. Seaton, in *Methods in Computational Physics*, Ed. by B. Adler, S. Fernbach, and M. Rotenburg (Academic, New York, 1971), Vol. 10, Chap. 1, pp. 9–81.
10. M. J. Seaton, Comput. Phys. Commun. **6**, 247 (1973).
11. M. K. Gaĭlitis, Usp. Fiz. Nauk **116**, 665 (1975) [Sov. Phys. Usp. **18**, 665 (1975)].
12. M. A. Crees, M. J. Seaton, and P. M. H. Wilson, Comput. Phys. Commun. **15**, 23 (1978).
13. V. V. Babikov, *Variable-Phase Method in Quantum Mechanics* (Nauka, Moscow, 1988).
14. H. A. Bethe and E. E. Salpeter, *Quantum Mechanics of One- and Two-Electron Atoms* (Academic, New York, 1957; Fizmatgiz, Moscow, 1960).
15. R. V. Damburg, *Atomic Collisions* (Akad. Nauk Latv. SSR, Riga, 1963).

Translated by R. Tyapaev

Doklady Physics, Vol. 49, No. 11, 2004, pp. 630–633. Translated from Doklady Akademii Nauk, Vol. 399, No. 3, 2004, pp. 330–333.

PHYSICS

Nonlinear Electromagnetic Delay of Electromagnetic Signals in the Magnetic Field of a Neutron Star

V. I. Denisov*, I. P. Denisova, I. V. Krivchenkov, and P. A. Vshivtseva

Presented by Academician A.A. Logunov June 1, 2004

Received June 1, 2004

Interest in the nonlinear electrodynamics of vacuum has been recently renewed [1, 2], because the sensitivity of current measuring instruments has closely approached the level that is required for detecting its effects [3, 4]. Therefore, after the first nonlinear electrodynamic experiment [5] recently carried out in Stanford, other experiments should follow in the near future that will make it possible to study the basic properties of the nonlinear interaction of electromagnetic fields in vacuum.

In our opinion, the measurement of the delay time of electromagnetic signals that have mutually orthogonal polarizations and have passed through the strong magnetic field of a pulsar or a magnetar is one of the most promising experiments for such a study. Let us analyze this problem more comprehensively.

Let us consider a neutron star (pulsar or magnetar) that has a strong magnetic field, radius R_s, and gravitational radius r_g. We take a coordinate system such that its origin is at the center of the star and a source and a receiver of electromagnetic radiation lie in the *XOZ* plane. Let the source and receiver be at the points ($x = b$, $y = 0$, $z = -a$) and ($x = b$, $y = 0$, $z = a$) symmetric with respect to the *XOY* plane. Since the magnetosphere of most neutron stars is filled with matter, we assume that the source (e.g., a Seyfert galaxy) emits in the X and gamma bands. The magnetosphere of pulsars and magnetars is transparent in the latter band.

According to the parameterized post-Maxwellian electrodynamics of vacuum [6], electromagnetic radiation propagates along the geodesics of a certain effective spacetime, the metric tensor g_{ik} of which depends on the polarization of this radiation due to birefringence of vacuum in strong electromagnetic fields. Therefore, an arbitrarily polarized electromagnetic signal in an external electromagnetic field splits into two signals carried by normal waves with mutually orthogonal polarizations along different rays. The metric tensor of the effective spacetime for these normal waves in the parameterized post-Maxwellian approximation has the form

$$g_{ik}^{(1,2)} = g_{ik}^{(0)} - 4\eta_{1,2}\xi F_{ip}F^{p}_{\cdot k}, \quad (1)$$

where $g_{ik}^{(0)}$ is the metric tensor of the background spacetime, η_1 and η_2 are the post-Maxwellian parameters [6] of the nonlinear electrodynamics of vacuum, $\xi = \dfrac{1}{B_q^2} \sim 10^{-27}\ \mathrm{G}^{-2}$, and the subscripts of the electromagnetic field tensor F_{nk} are lifted by the metric tensor $g^{kn}_{(0)}$.

Since neutron stars have a sufficiently strong gravitational field, the Schwarzschild solution should be taken as the metric tensor $g_{ik}^{(0)}$ of the background spacetime for the problem under consideration. In the isotropic spherical coordinates, this solution with post-Newtonian accuracy has the form

$$g_{22}^{(0)} = r^2 g_{11}^{(0)}, \quad g_{33}^{(0)} = g_{22}^{(0)}\sin^2\theta,$$

$$g_{00}^{(0)} = 1 - \frac{r_g}{r} + \frac{r_g^2}{2r^2}, \quad g_{11}^{(0)} = -\left[1 + \frac{r_g}{r} + \frac{3r_g^2}{8r^2}\right].$$

Assuming that the magnetic dipole moment of the neutron star generally has the components $m_x = m\sin\alpha\cos\beta$, $m_y = m\sin\alpha\sin\beta$, and $m_z = m\cos\alpha$, we write the tensor F_{pk} in the spherical coordinate system in the form

$$F_{12} = F_{r\theta} = -\frac{|\mathbf{m}|}{r^2}\sin\alpha\sin(\varphi - \beta),$$

$$F_{32} = F_{\varphi\theta} = \frac{2|\mathbf{m}|\sin\theta}{r}$$

$$\times\{\cos\theta\cos\alpha + \sin\theta\sin\alpha\cos(\varphi - \beta)\},$$

$$F_{13} = F_{r\varphi} = \frac{|\mathbf{m}|\sin\theta}{r^2}$$

$$\times\{\sin\theta\cos\alpha - \cos\theta\sin\alpha\cos(\varphi - \beta)\}.$$

Moscow State University,
Vorob'evy gory, Moscow, 119992 Russia
** e-mail: denisov@srd.sinp.msu.ru*

1028-3358/04/4911-0630$26.00

The motion of photons in the pseudo-Riemannian spacetime with metric tensor (1) proceeds along the geodesics of this space and is described by the equations

$$\frac{dk^m}{d\sigma} + \Gamma^m_{pn} k^p k^n = 0, \quad (2)$$

where $k^m = \frac{dx^m}{d\sigma}$ and σ is the affine parameter.

For $m = 0$, Eq. (2) takes the form

$$\frac{dk^0}{d\sigma} + \frac{r_g}{r^2} k^0 k^1 = 0$$

and is simply integrated as

$$k^0 = 1 + \frac{r_g}{r} + \frac{r_g^2}{2r^2}. \quad (3)$$

The remaining equations of system (2) take the form

$$\ddot{r} - r[\dot{\theta}^2 + \dot{\varphi}^2 \sin^2\theta] + \frac{r_g}{2r^2} - \frac{r_g}{2r^2}\left(1 - \frac{r_g}{4r}\right)$$
$$\times [\dot{r}^2 - r^2(\dot{\theta}^2 + \dot{\varphi}^2 \sin^2\theta)] + \frac{12\eta\xi m^2}{r^7}$$
$$\times \{[\dot{r}^2 + r^2(\dot{\theta}^2 + \dot{\varphi}^2 \sin^2\theta)][\sin\theta \sin\alpha \cos(\varphi - \beta)$$
$$+ \cos\theta \cos\alpha]^2 - \dot{r}^2 + r^2(\dot{\theta}^2 + \dot{\varphi}^2 \sin^2\alpha)$$
$$+ 2r\dot{r}\dot{\theta}[(2\sin^2\theta - 1)\sin\alpha\cos\alpha\cos(\varphi - \beta)$$
$$+ \sin\theta\cos\theta(\cos^2\alpha - \sin^2\alpha\cos^2(\varphi - \beta))]$$
$$+ 2r\dot{r}\dot{\varphi}\sin\theta\sin\alpha\sin(\varphi - \beta)$$
$$\times [\sin\theta\sin\alpha\cos(\varphi - \beta) + \cos\theta\cos\alpha]\} = 0,$$

$$\ddot{\theta} + \frac{1}{r}[2\dot{r}\dot{\theta} - r\dot{\varphi}^2 \sin\theta\cos\theta] - \frac{r_g \dot{r}\dot{\theta}}{r^2}\left(1 - \frac{r_g}{4r}\right)$$
$$+ \frac{12\eta\xi m^2}{r^8}\left\{\frac{3\dot{r}^2 - 2r^2\dot{\theta}^2}{2}[(2\sin^2\theta - 1)\sin 2\alpha \cos(\varphi - \beta)\right.$$
$$+ \sin 2\theta(\cos^2\alpha - \sin^2\alpha\cos^2(\varphi - \beta))]$$
$$- 2r\dot{r}\dot{\theta}[\sin^2\alpha\sin^2(\varphi - \beta) + 4(\sin\theta\sin\alpha\cos(\varphi - \beta) \quad (4)$$
$$+ \cos\theta\cos\alpha)^2] - 2r^2\dot{\theta}\dot{\varphi}\sin\theta\sin\alpha\sin(\varphi - \beta)$$
$$\times (\cos\theta\cos\alpha + \sin\theta\sin\alpha\cos(\varphi - \beta))$$
$$+ 2r\dot{r}\dot{\varphi}\sin\theta\sin\alpha\sin(\varphi - \beta)(\sin\theta\cos\alpha$$
$$\left. - \cos\theta\sin\alpha\cos(\varphi - \beta))\right\} = 0,$$

$$\ddot{\varphi} + \frac{2\dot{\varphi}}{r\sin\theta}[\dot{r}\sin\theta + r\dot{\theta}\cos\theta] - \frac{r_g \dot{r}\dot{\varphi}}{r^2}\left(1 - \frac{r_g}{4r}\right)$$
$$+ \frac{12\eta\xi m^2}{r^8\sin\theta}\{[3\dot{r}^2 - 2r^2\dot{\varphi}^2\sin^2\theta]$$
$$\times (\cos\theta\cos\alpha + \sin\theta\sin\alpha\cos(\varphi - \beta))\sin\alpha\sin(\varphi - \beta)$$
$$+ 2r\dot{r}\dot{\theta}\sin\alpha\sin(\varphi - \beta)(\sin\theta\cos\alpha$$
$$- \cos\theta\sin\alpha\cos(\varphi - \beta)) - 2r\dot{r}\dot{\varphi}\sin\theta[3(\sin\theta\sin\alpha$$
$$\times\cos(\varphi - \beta) + \cos\theta\cos\alpha)^2 + \sin^2\alpha\cos^2(\varphi - \beta) + \cos^2\alpha]$$
$$- 2r^2\dot{\theta}\dot{\varphi}\sin\theta[(2\sin^2\theta - 1)\sin\alpha\cos\alpha\cos(\varphi - \beta)$$
$$+ \sin\theta\cos\theta(\cos^2\alpha - \sin^2\alpha\cos^2(\varphi - \beta))]\} = 0,$$

where a dot over a symbol means it is derivative with respect to σ.

One more equation follows from the fact that the four-vector k^n must satisfy the condition $g^{1,2}_{nm} k^n k^m = 0$, which is the first integral of the system of Eqs. (2). We solve these equations by successive approximations with respect to small parameters of the problem, assuming that a signal is emitted for $\sigma = 0$ from the point $(x = b, y = 0, z = -a)$ and passes through the point $(x = b, y = 0, z = a)$. The substitution of the expressions

$$r^2 = f_{gr}(\sigma) + f_{el}(\sigma), \quad r\cos\theta = z_{gr}(\sigma) + z_{el}(\sigma),$$
$$\varphi = \varphi_{el}(\sigma)$$

into Eqs. (4) yields

$$f_{gr}(\sigma) = (\sigma - a)^2 + b^2$$
$$+ 2r_g[\sqrt{a^2 + b^2} - \sqrt{(\sigma - a)^2 + b^2}] - r_g^2\left[\frac{a\sigma}{b^2} - 2\right.$$
$$- \frac{3(3\sigma + 2a)}{8b}\arctan\frac{a}{b} + \frac{2\sqrt{a^2 + b^2}}{\sqrt{(\sigma - a)^2 + b^2}}$$
$$\left. + \frac{3(\sigma - a)}{4b}\arctan\frac{\sigma - a}{b}\right],$$

$$z_{gr}(\sigma) = \sigma - a + \frac{r_g^2}{16b}$$
$$\times\left\{9\left[\arctan\frac{\sigma - a}{b} + \arctan\frac{a}{b}\right] - \frac{8\sigma}{b}\right\}.$$

For the nonlinear electrodynamic part, we obtain

$$f_{el}(\sigma) = \eta_{1,2}\xi m^2\left\{C_0 + C_1\sigma + \left[\frac{b^2}{2[(\sigma-a)^2+b^2]^3} + \frac{15}{8[(\sigma-a)^2+b^2]^2} + \frac{75}{16b^2[(\sigma-a)^2+b^2]} - \frac{225(\sigma-a)}{16b^5}\arctan\frac{\sigma-a}{b}\right]\sin^2\alpha\cos^2\beta - \left[\frac{9(\sigma-a)}{16b^5}\arctan\frac{\sigma-a}{b} - \frac{b^2}{2[(\sigma-a)^2+b^2]^3} - \frac{7}{8[(\sigma-a)^2+b^2]^2} - \frac{3}{16b^2[(\sigma-a)^2+b^2]}\right]\sin^2\alpha + \left[\frac{39(\sigma-a)}{16b^3[(\sigma-a)^2+b^2]} + \frac{13(\sigma-a)}{8b[(\sigma-a)^2+b^2]^2} + \frac{(\sigma-a)b}{2[(\sigma-a)^2+b^2]^3} + \frac{39}{16b^4}\arctan\frac{\sigma-a}{b}\right]\sin 2\alpha\cos\beta - \frac{b^2}{2[(\sigma-a)^2+b^2]^3} - \frac{135(\sigma-a)}{16b^5}\arctan\frac{\sigma-a}{b} + \frac{9}{8[(\sigma-a)^2+b^2]^2} + \frac{45}{16b^2[(\sigma-a)^2+b^2]}\right\},$$

$$z_{el}(\sigma) = -\eta_{1,2}\xi m^2\left\{C_2 + \left[\frac{75(\sigma-a)}{64b^4[(\sigma-a)^2+b^2]} + \frac{25(\sigma-a)}{32b^2[(\sigma-a)^2+b^2]^2} + \frac{5(\sigma-a)}{8[(\sigma-a)^2+b^2]^3} + \frac{9(\sigma-a)b^2}{4[(\sigma-a)^2+b^2]^4} + \frac{75}{64b^5}\arctan\frac{\sigma-a}{b}\right]\sin^2\alpha\cos^2\beta + \left[\frac{3}{64b^5}\arctan\frac{\sigma-a}{b} + \frac{9b^2(\sigma-a)}{4[(\sigma-a)^2+b^2]^4} - \frac{3(\sigma-a)}{8[(\sigma-a)^2+b^2]^3} + \frac{\sigma-a}{32b^2[(\sigma-a)^2+b^2]^2} + \frac{3(\sigma-a)}{64b^4[(\sigma-a)^2+b^2]}\right]\sin^2\alpha - \left[\frac{9b^3}{4[(\sigma-a)^2+b^2]^4} - \frac{b}{[(\sigma-a)^2+b^2]^3}\right]\sin 2\alpha\cos\beta + \frac{45}{64b^5}\arctan\frac{\sigma-a}{b} - \frac{9b^2(\sigma-a)}{4[(\sigma-a)^2+b^2]^4} + \frac{3(\sigma-a)}{8[(\sigma-a)^2+b^2]^3} + \frac{15(\sigma-a)}{32b^2[(\sigma-a)^2+b^2]^2} + \frac{45(\sigma-a)}{64b^4[(\sigma-a)^2+b^2]}\right\},$$

$$\varphi_{el}(\sigma) = \eta_{1,2}\xi\left\{C_3 + C_4\sigma + \left[\frac{3}{32b^6}\arctan\frac{\sigma-a}{b} + \frac{5(\sigma-a)}{4b[(\sigma-a)^2+b^2]^3} + \frac{(\sigma-a)}{16b^3[(\sigma-a)^2+b^2]^2} + \frac{3(\sigma-a)}{32b^5[(\sigma-a)^2+b^2]}\right]\cos\alpha - \left[\frac{75(\sigma-a)}{32b^7}\operatorname{arccot}\frac{\sigma-a}{b} - \frac{5}{4[(\sigma-a)^2+b^2]^3} + \frac{5}{16b^2[(\sigma-a)^2+b^2]^2} + \frac{25}{32b^4[(\sigma-a)^2+b^2]}\right]\times\sin\alpha\cos\beta\right\}\sin\alpha\sin\beta,$$

where the integration constants have the form

$$C_0 = \frac{a(39a^4+104a^2b^2+73b^4)}{16b^3(a^2+b^2)^3}\sin 2\alpha\cos\beta - \left[\frac{45a^2+108a^2b^2+55b^4}{16b^2(a^2+b^2)^3} + \frac{3a^4+20a^2b^2+25b^4}{16b^2(a^2+b^2)^3}\times\sin^2\alpha + \frac{75a^4+180a^2b^2+113b^4}{16b^2(a^2+b^2)^3}\sin^2\alpha\cos^2\beta\right] + \frac{9a}{16b^5}[\sin^2\alpha + 25\sin^2\alpha\cos^2\beta + 15]\arctan\frac{a}{b} + \frac{39}{16b^4}\sin 2\alpha\cos\beta,$$

$$C_1 = -\left[\frac{39}{16ab^4}\arctan\frac{a}{b} + \frac{39a^4+104a^2b^2+73b^4}{16b^3(a^2+b^2)^3}\right]\sin 2\alpha\cos\beta,$$

$$C_2 = \frac{3a(15a^6 + 55a^4b^2 + 73a^2b^4 - 15b^6)}{64b^4(a^2 + b^2)^4}$$

$$+ \frac{3}{64b^5}\left[25\sin^2\alpha\cos^2\beta + 15 + \sin^2\alpha\right]\arctan\frac{a}{b}$$

$$+ a\left[\frac{75a^6 + 275a^4b^2 + 365a^2b^4 + 309b^6}{64b^4(a^2 + b^2)^4}\cos^2\beta\right.$$

$$\left. + \frac{3a^6 + 11a^4b^2 - 11b^4a^2 + 125b^6}{64b^4(a^2 + b^2)^4}\right]\sin^2\alpha$$

$$- \frac{(4a^2 - 5b^2)b}{4(a^2 + b^2)^4}\sin 2\alpha\cos\beta,$$

$$C_3 = \left[\frac{a(3a^4 + 8a^2b^2 + 45b^4)}{32b^5(a^2 + b^2)^3}\cos\alpha\right.$$

$$\left. + \frac{5b(5a^4 + 12a^2b^2 - b^4)}{32b^5(a^2 + b^2)^3}\sin\alpha\cos\beta\right]$$

$$+ \frac{3}{32b^6}\arctan\frac{a}{b}\cos\alpha + \frac{75a}{32b^7}\operatorname{arccot}\frac{a}{b}\sin\alpha\cos\beta,$$

$$C_4 = -\left[\frac{3}{32ab^6}\arctan\frac{a}{b} + \frac{3a^4 + 8a^2b^2 + 45b^4}{32b^5(a^2 + b^2)^3}\right]\cos\alpha.$$

Electromagnetic signals arrive at the receiver for the σ value,

$$\sigma_{1,2} = 2a + r_g^2\left[\frac{a}{b^2} - \frac{9}{8b}\arctan\frac{a}{b}\right]$$

$$+ \frac{\eta_{1,2}\xi m^2}{32b^5}\left\{3\left[25\sin^2\alpha\cos^2\beta + \sin^2\alpha + 15\right]\arctan\frac{a}{b}\right.$$

$$+ ab\left[\frac{75a^6 + 275a^4b^2 + 365a^2b^4 + 309b^6}{(a^2 + b^2)^4}\sin^2\alpha\cos^2\beta\right.$$

$$+ \frac{3a^6 + 11(a^4b^2 - a^2b^4) + 125b^6}{(a^2 + b^2)^4}\sin^2\alpha$$

$$\left.\left. + \frac{3[15(a^6 - b^6) + 55a^4b^2 + 73a^2b^4]}{(a^2 + b^2)^4}\right]\right\}.$$

Integrating Eq. (3), we obtain

$$ct(\sigma) = \sigma - a + r_g\ln\left\{\frac{[\sqrt{(\sigma - a)^2 + b^2} + \sigma - a]}{[\sqrt{b^2 + a^2} - a]}\right\}$$

$$- \frac{r_g^2}{2b}\left\{\frac{2a}{b} + \frac{2(\sigma - a)\sqrt{a^2 + b^2}}{b\sqrt{(\sigma - a)^2 + b^2}}\right.$$

$$\left. - 3\left[\arctan\frac{\sigma - a}{b} + \arctan\frac{a}{b}\right]\right\}.$$

Assuming that $a \gg b > R_s$, we obtain the time of nonlinear electrodynamic delay in the form

$$\Delta t = t(\sigma_1) - t(\sigma_2)$$

$$= \frac{3\pi(\eta_1 - \eta_2)\xi m^2}{64cb^5}[25\sin^2\alpha\cos^2\beta + \sin^2\alpha + 15].$$

This quantity for typical pulsars and magnetars may reach a measurable value of 0.2 μs.

ACKNOWLEDGMENTS

This work was supported by the Council of the President of the Russian Federation for Support of Young Russian Scientists and Leading Scientific Schools, project no. NSh-1450.2003.2.

REFERENCES

1. V. G. Kadyshevsky and V. N. Rodionov, Teor. Mat. Fiz. **136** (3), 517 (2003) [Theor. Math. Phys. **136**, 1346 (2003)].
2. V. N. Rodionov, Zh. Éksp. Teor. Fiz. **125** (2004) [JETP **98**, 395 (2004)].
3. V. I. Denisov, Phys. Rev. D **61**, 036004 (2000).
4. V. I. Denisov, I. V. Krivchenkov, and N. V. Kravtsov, Phys. Rev. D **69**, 066008 (2004).
5. D. L. Burke, R. C. Field, G. Horton-Smith, *et al.*, Phys. Rev. Lett. **79**, 1626 (1997).
6. V. I. Denisov and I. P. Denisova, Dokl. Akad. Nauk **378** (4), 463 (2001) [Dokl. Phys. **46**, 377 (2001)].

Translated by R. Tyapaev

Doklady Physics, Vol. 49, No. 11, 2004, pp. 634–637. Translated from Doklady Akademii Nauk, Vol. 399, No. 1, 2004, pp. 34–37.

TECHNICAL PHYSICS

On the Theory of Crystal-Surface Growth near a Crystallization Point

S. O. Gladkov

Presented by Academician O.A. Bannykh December 30, 2003

Received December 30, 2003

In this study, a differential equation describing the dynamics of the crystal-surface development in a viscous vitreous substance is derived from the solution of the variational problem with a mobile boundary. It is shown that, in this case, the heterogeneity of viscosity is a very important factor.

The transversality equation is analyzed, and its physical solution describing the development of a crystal in both time and space is found.

Previously [1, 2], we have proposed a general approach for the mathematical description of the crystallization-dynamics development. This approach was based on the assumption of the stochastic variation of a solid-phase nucleus and its subsequent growth from the standpoint of linear-size crystal evolution [1]. Later, in [2], a technique for analysis of the dynamic evolution of the nucleus was proposed that used a synergetic approach based on the general expression for the dissipative function. In this connection, we would like to note that the equation of motion obtained in [2] generally describes only a trajectory of motion for a certain abstract point on the surface of a future crystal. However, the equation determining the surface $z(x, y, t)$ (x and y are the coordinates, and t is time) was not presented in an explicit form. This disadvantage is eliminated in this study devoted to the derivation of the evolution equations of a solid-phase nucleus, which allows us to describe arbitrary (including rather complicated) surfaces of growing crystals.

We write the general expression for the dissipative function, which is similar to that in [2], as

$$\dot{Q} = \frac{B_{ikln}}{2\eta_0}\int_V v_i \nabla_k \eta M_l M_n d^3x, \qquad (1)$$

where B_{ikln} is the dimensionless tensor of the fourth rank; the subscripts i, k, l, and n take the values x, y, and z, and the repeated subscripts imply summation, with the summation sign being omitted; and v_i are the velocity components of very small particles (we call them crystallons) adhering to a fluctuation formed nucleus of the future solid phase. The angular momentum of these particles is $\mathbf{M} = m[\mathbf{v} \times \mathbf{r}]$, where m is the particle's mass, η is the viscosity, and η_0 is the constant with the dimension of viscosity.

We introduce the total energy loss as an integral of expression (1) over time:

$$Q = \frac{B_{ikln}}{2\eta_0}\int v_i \nabla_k M_l M_n d\Omega, \qquad (2)$$

where the volume element is $d\Omega = dx\,dy\,dz\,dt$.

We now require that, in a stationary case as $t \longrightarrow \infty$, the dissipation will be minimal and represent the stationary equation of motion in the form

$$\left.\frac{\delta Q}{\delta \mathbf{r}}\right|_{z = x(x, y, t)} = 0. \qquad (3')$$

Thus, the problem consists in calculating the variational derivative for expression (2).

In order to demonstrate the calculation technique and the approach in itself, we choose the tensor B_{ikln} in a simplified form—namely, we assume that $B_{ikln} = B\delta_{ik}\delta_{ln}$.

As a result, we obtain, from expression (2),

$$Q = \frac{B}{2\eta_0}\int_V\int_{t_0}^{t_1} (\mathbf{v}\nabla\eta)\mathbf{M}^2 d\Omega. \qquad (3)$$

Next, we transform the integrand in (3) using integration by parts in the following manner. We represent it as

$$(\mathbf{v}\nabla\eta)\mathbf{M}^2 = \nabla(\eta\mathbf{v}\mathbf{M})^2 - \eta\nabla\cdot(\mathbf{v}\mathbf{M}^2).$$

By definition, the angular momentum is $\mathbf{M} = m[\mathbf{v} \times \mathbf{r}]$. Therefore, it is easy to show that the latter term $\nabla \cdot (\mathbf{v}\mathbf{M}^2)$ identically vanishes. As a result, using the Gauss–Ostrogradskiĭ formula, we can transform the

Moscow State Regional University,
ul. Radio 10a, Moscow, 105005 Russia
e-mail: Sglad@newmail.ru

1028-3358/04/4911-0634$26.00

volume integral to the integral over the surface of a growing (!) solid nucleus.

In so far as the volume changes with time and its boundary (the surface Σ) moves while varying functional (3), it is necessary to solve the problem involving a mobile boundary. This implies that the expression for the variation of the functional δQ should be represented as a sum of two integrals,

$$\delta Q = B\int_{V}^{V+\delta V}\int_{t_0}^{t_1}(\mathbf{v}\nabla\eta)\mathbf{M}^2 d\Omega + Bd\iint_{Vt_0}^{t_1}\nabla(\mathbf{v}\eta\mathbf{M}^2)d\Omega. \quad (4)$$

Taking into account the above comments, we obtain

$$\delta Q = B\int_{t_0}^{t_1}\left[(\mathbf{v}\nabla\eta)\mathbf{M}^2\big|_\Sigma\delta V + 2\int_\Sigma(\mathbf{vn})\eta(\mathbf{M}\delta\mathbf{M})d\sigma\right]dt. \quad (5)$$

The volume variation is $\delta V = |[\mathbf{n}\times\delta\mathbf{r}]|\sigma$, where σ is the surface area. From this, it follows that

$$\begin{aligned}\delta V &= |[\mathbf{n}\times\delta\mathbf{r}]|\sigma \\ &= \sigma\sqrt{\delta x^2\sin^2\alpha + \delta y^2\sin^2\beta + \delta z^2\sin^2\gamma} \\ &= \sqrt{2}\cos^2\gamma\sqrt{z_x^2 + z_y^2 + z_x^2 z_y^2}\,\sigma\,\delta l, \end{aligned} \quad (6)$$

where $\delta l^2 = \delta x^2 + \delta y^2 + \delta z^2$ and the direction cosines of the vector of the surface normal are conventionally given by the relations

$$\cos\alpha = -z_x\cos\gamma,$$
$$\cos\beta = -z_y\cos\gamma,$$
$$\cos\gamma = \frac{1}{\sqrt{1 + z_x^2 + z_y^2}}.$$

The angular-momentum variation is

$$\delta\mathbf{M} = m[\delta\mathbf{v}\times\mathbf{r}] + m[\mathbf{v} + \delta\mathbf{r}],$$

where $\delta\mathbf{v} = \dfrac{\partial\delta\mathbf{r}}{\partial t}$. The integration of relationship (5) by parts with respect to time results in a doubled value of $\delta\mathbf{M}$: $\delta\mathbf{M} \longrightarrow 2m[\mathbf{v}\times\mathbf{r}]$. For the scalar product $\mathbf{M}\delta\mathbf{M}$, we have

$$\begin{aligned}\mathbf{M}\delta\mathbf{M} = m^2\delta l[&v^2(x\cos\alpha + y\cos\beta + z\cos\gamma) \\ &-(\mathbf{vr})(v_x\cos\alpha + v_y\cos\beta + v_z\cos\gamma)].\end{aligned} \quad (7)$$

Assuming that

$$\int_\Sigma(\mathbf{vn})\eta(\mathbf{M}\delta\mathbf{M})d\sigma = \eta(\mathbf{vn})(\mathbf{M}\delta\mathbf{M})|_\Sigma\sigma,$$

and taking into account expressions (6) and (7) and the above statement following from the condition $\delta Q = 0$, we find the transversality equation for our problem:

$$\begin{aligned}&\sqrt{2}(\mathbf{v}\nabla\eta)[\mathbf{v}\times\mathbf{r}]^2\cos^2\gamma\sqrt{z_x^2 + z_y^2 + z_x^2 z_y^2}\Big|_\Sigma \\ &+ 4\eta(\mathbf{vn})[v^2(x\cos\alpha + y\cos\beta + z\cos\gamma) \\ &-(\mathbf{vr})(v_x\cos\alpha + v_y\cos\beta + v_z\cos\gamma)]|_\Sigma = 0.\end{aligned} \quad (8)$$

Thus, we have obtained the evolution equation for the surface Σ. This equation makes it possible to describe not only the shape of the surface, but also its further evolution with time. Below, we consider a simple case.

Let the viscosity gradient be directed along the z axis; i.e., $\nabla\eta = \left(0, 0, \dfrac{\partial\eta}{\partial z}\right)$, and the crystal growth-rate vector have one component and be also directed along the z axis $\left(\mathbf{v} = \left(0, 0, \dfrac{\partial z}{\partial t}\right)\right)$. As a result (after reducing by v_z^3), we obtain from (8) the following considerably simpler equation:

$$a^2(x^2 + y^2)^2\,\frac{z_x^2 + z_y^2 + z_x^2 z_y^2}{1 + z_x^2 + z_y^2} = 8(xz_x + yz_y)^2, \quad (9)$$

where $a = \dfrac{1}{\eta}\dfrac{\partial\eta}{\partial z}$. It should be noted that, here, we used explicit expressions for direction cosines of the normal to the surface.

In Eq. (9), it is convenient to pass to the polar coordinates $x = r\cos\varphi$ and $y = r\sin\varphi$. As a result, we obtain

$$\begin{aligned}\frac{8}{r^2}\left(\frac{\partial z}{\partial r}\right)^2\left[1 + \left(\frac{\partial z}{\partial r}\right)^2 + \frac{1}{r^2}\left(\frac{\partial z}{\partial\varphi}\right)^2\right] &= a^2\left[\left(\frac{\partial z}{\partial r}\right)^2 + \frac{1}{r^2}\left(\frac{\partial z}{\partial\varphi}\right)^2\right. \\ &\left. + \frac{1}{r^4}\left(r\cos\varphi\frac{\partial z}{\partial r} - \sin\varphi\frac{\partial z}{\partial\varphi}\right)^2\left(r\sin\varphi\frac{\partial z}{\partial r} + \cos\varphi\frac{\partial z}{\partial\varphi}\right)^2\right].\end{aligned} \quad (10)$$

Assuming that, near the crystallization temperature T_{cr}, the latter term in the right-hand side of Eq. (10) can be ignored and provided that the function z is independent of the angular variable φ, we arrive at the quite simple equation,

$$a^2 = \frac{8}{r^2}\left[1 + \left(\frac{\partial z}{\partial t}\right)^2\right].$$

Upon separating the variables and integrating, we find

the solution,

$$z = \pm\left[\frac{r}{2}\sqrt{\frac{a^2r^2}{8}-1} - \frac{\sqrt{2}}{a}\ln\left(\frac{ar}{2\sqrt{2}} + \sqrt{\frac{a^2r^2}{8}-1}\right)\right] + 2C(t), \quad (11)$$

where $C(t)$ is a certain function of time, and the factor 2 is introduced for the sake of convenience.

Since the crystal viscosity at surface temperature T follows the Fogel–Fulcher law [3], $\eta = \bar{\eta}e^{\Delta/(T-T_\sigma)}$ (where $\bar{\eta}$ is a constant with the dimension of viscosity, Δ is the activation energy or, in other words, the barrier through which atoms of liquid tunnel into the solid phase; we assume that the Boltzmann constant k_B is unity). Further, by virtue of a large value of η and also considering the parameter a to be large ($a \gg 1$), from Eq. (11), we find the following simpler approximate equation:

$$z = \pm\frac{r^2}{4\sqrt{2}}\frac{1}{\eta}\frac{\partial\eta}{\partial z} + 2C(t). \quad (12)$$

Integrating this equation over the variable z, we arrive at

$$z^2 = \pm\frac{r^2}{2\sqrt{2}}\ln\eta + 2zC(t) + A(t), \quad (13)$$

where $A(t)$ is one more function of time. Furthermore, resolving Eq. (13) with respect to z, we have

$$z = C(t) \pm \sqrt{C^2(t) \pm \frac{r^2}{2\sqrt{2}}\frac{\Delta}{T-T_{cr}} + A(t)}. \quad (14)$$

For finding $C(t)$ and $A(t)$, it is necessary to use an additional equation that, according to [2], can be represented in the phenomenological form $\mathbf{M} = \frac{\delta\dot{Q}}{\delta\mathbf{M}}$. Using Eq. (3), we obtain, as a result, the equation for extremals,

$$\dot{\mathbf{M}} = \frac{B}{\eta_0}(\mathbf{v}\nabla\eta)\mathbf{M}. \quad (15)$$

Its solution is

$$\mathbf{M} = \mathbf{M}_0\exp\left(\frac{B}{\eta_0}\int v_z\frac{\partial\eta}{\partial z}dt\right) = \mathbf{M}_0\exp\left(B\frac{\eta}{\eta_0}\right). \quad (16)$$

From here, we find, for the x component,

$$v_y z - y v_z = M_{0x}\exp\left(B\frac{\eta}{\eta_0}\right).$$

We now choose the simplest variation law for the coordinates: $x = \bar{v}t$ and $y = \bar{v}t$. Then, we can write the equation for the coordinate z,

$$t\dot{z} - z = -\frac{M_{0x}}{\bar{v}}\exp\left(B\frac{\eta}{\eta_0}\right). \quad (17)$$

Assuming the constant B to be small (which is, in fact, true), it is possible to take $\exp\left(B\frac{\eta}{\eta_0}\right) \approx 1$ and to write the solution of Eq. (17) as

$$z = \frac{M_{0x}}{\bar{v}} + Dt, \quad (18)$$

where D is the integration constant.

We choose the solution to Eq. (14) in the form

$$z = C(t) + \sqrt{C^2(t) - \frac{r^2}{2\sqrt{2}}\frac{\Delta}{T-T_{cr}} + A(t)} \quad (19)$$

and assume that $A(t) = 0$.

Solution (19) is valid for surface boundary points. Therefore, to satisfy both solution (19) and (18), we choose $D = v_0$, where v_0 is the growth rate of the coordinate z at $t = 0$, and $z(0) = z_0$. As a result of sewing both solutions, we arrive at the function $C(t)$,

$$C(t) = \frac{1}{2}(z_0 + v_0 t) + \alpha\frac{\bar{v}^2t^2}{v_0t + z_0}, \quad (20)$$

where the parameter α is $\alpha = \frac{\Delta}{2\sqrt{2}(T-T_{cr})}$.

By virtue of $\alpha \gg 1$, solution (19) can be approximately written as

$$z(t, r) \approx 2C(t) - \frac{\alpha r^2}{2C(t)}.$$

Using Eq. (20), we finally obtain

$$z(t, r) = z_0 + v_0 t + \alpha\frac{\bar{v}^2t^2}{z_0 + v_0t} - \frac{\alpha r^2}{z_0 + v_0t + 2\alpha\frac{\bar{v}^2t^2}{z_0 + v_0t}}. \quad (21)$$

As is seen from the simple analysis of the solution, the nucleus is a needle (this is provided by the large value of the parameter α), which begins to grow at the instant of time $t = 0$ at the point z_0 for $r = 0$. Then, it attains a certain size L along the z axis converging to the point $r = 0$. The time required for the growth is determined from Eq. (21), and it turns out to be

$$t_0 \approx \frac{(L - z_0)v_0}{v_0^2 + \alpha\bar{v}^2}. \quad (22)$$

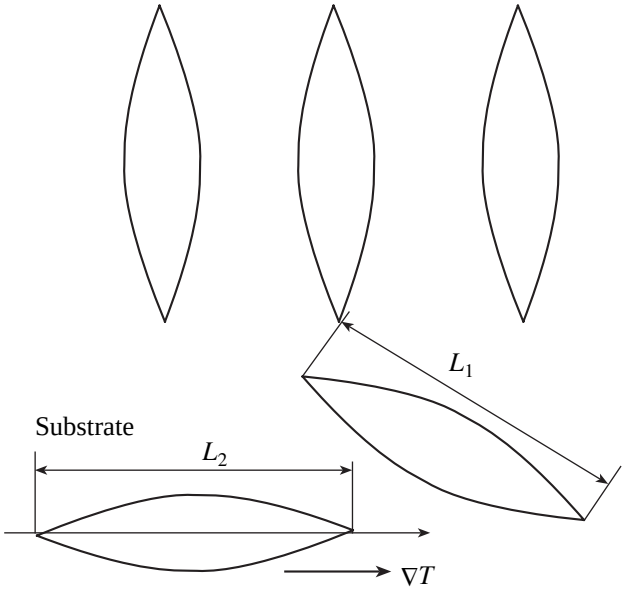

Schematic representation of a developing crystal with the shape of a double-edged needle. The number of needles is large due to the stochastic nature of nucleation of the crystallization areas chaotically scattered over the substrate surface. For a chosen needle, the directions of the z axis and temperature gradient are shown.

It is necessary to emphasize that, due to the chaotic appearance of future solid-phase nuclei, their localization over the substrate area is characterized by determinate chaos (see, for example, [4, 5], where the synergetic theory is developed for homogeneous and inhomogeneous fluctuations of the density and temperature in the bulk of liquid). In each of these i areas, a solid needle starts to be formed and dynamically developed (irrespective of the other needles). Thus, the similar process has a multivariate character, but, due to the statistical independence of each needle, can be described individually using the approach mentioned above. (By the way, the formation of such needles over a substrate was also observed in experiments.)

To conclude, once again, we pay attention to three important points.

The general transversality condition is found, which enables us to describe virtually arbitrary growth dynamics and the surface shape of crystals being formed inside a certain vitreous substance. The complete set of Eqs. (8) and (12) of the variational problem is solved. Dependence (21) of the surface shape on the coordinates and time (see figure) is analytically determined. An estimate (22) of needle formation time is presented.

ACKNOWLEDGMENTS

The author thanks E.F. Medvedev for the possibility to become acquainted with his experimental results before their publication.

REFERENCES

1. S. O. Gladkov, Dokl. Akad. Nauk **391**, 610 (2003) [Dokl. Phys. **48**, 405 (2003)].
2. S. O. Gladkov, Dokl. Akad. Nauk **394**, 469 (2004) [Dokl. Phys. **49**, 82 (2004)].
3. S. O. Gladkov, *Physics of Composites: Thermodynamic and Dissipative Properties* (Nauka, Moscow, 1999).
4. S. O. Gladkov and I. V. Gladyshev, Zh. Tekh. Fiz. **71** (3), 1 (2001).
5. S. O. Gladkov and I. V. Gladyshev, Zh. Tekh. Fiz. **71** (4), 1 (2001).

Translated by V. Bukhanov

Doklady Physics, Vol. 49, No. 11, 2004, pp. 638–643. Translated from Doklady Akademii Nauk, Vol. 399, No. 3, 2004, pp. 334–338.

THEORETICAL PHYSICS

Majorana Properties of Free Particles in the Pauli Symmetry Scheme

Yu. V. Gaponov

Presented by Academician E.P. Velikhov June 24, 2004

Received June 28, 2004

Analysis of the Majorana properties of neutrino [1] is one of the key problems of the physics of weak processes. Majorana neutrino models have been developed in two variants: (i) in a variant initiated by Pontecorvo [2] with left and right (sterile) neutrinos and (ii) in a variant involving neutrinos of different generations [3, 4]. In the former variant, the neutrino Lagrangian includes Dirac (m_D) and Majorana ($m_{L,R}$) mass terms of the form [5–9]

$$\begin{aligned} -2L_m(x) &= m_D(\overline{\psi_R}(x)\psi_L(x) + \overline{\psi_R^c}(x)\psi_L^c(x)) \\ &+ \overline{\psi_R}(x)m_R\psi_L^c(x) + \overline{\psi_R^c}(x)m_L\psi_L(x) + \text{h.c.} \\ &= \overline{n_L^c}(x)\hat{M}n_L(x) + \text{h.c.}, \end{aligned} \tag{1}$$

$$n_L(x) = \begin{pmatrix} \psi_L(x) \\ \psi_L^c(x) \end{pmatrix}, \quad \hat{M} = \begin{pmatrix} m_L & m_D \\ m_D & m_R \end{pmatrix},$$

which is determined by the general symmetry properties. This procedure for the introduction of the Majorana properties of particles is quite general. However, physical foundations for the joint description of Majorana and Dirac properties and choice of $n_L(x)$ in form (1) remain unclear. A modernization of this variant of Majorana models, which is based on special Pauli transformations providing such a foundation, is proposed in this paper (see also [10]).

As was shown by Pauli [11], for fermion fields with zero mass, there are the transformations

$$\begin{aligned} \psi'(x) &= e^{i\gamma_5\chi/2}(a\psi(x) + b\gamma_5\gamma_2\gamma_4\overline{\psi}^T(x)), \\ |a|^2 + |b|^2 &= 1, \end{aligned} \tag{2}$$

that conserve the commutators of a field and include chiral transformations (type II according to Pauli) and pure Pauli transformations (type I). The latter transformations for $a = e^{i\varphi/2}$ and $b = 0$ correspond to phase transformations. In terms of the generalized two-component function $\Psi(x)$ and operators $\hat{\kappa}_i$, $i = x, y, z$, introduced as

$$\Psi(x) = \begin{pmatrix} \psi(x) \\ \gamma_5\gamma_2\gamma_4\overline{\psi}^T(x) \end{pmatrix}, \quad \hat{\kappa}_x = \begin{pmatrix} 0 & +1 \\ +1 & 0 \end{pmatrix},$$
$$\hat{\kappa}_y = \begin{pmatrix} 0 & -i \\ +i & 0 \end{pmatrix}, \quad \hat{\kappa}_z = \begin{pmatrix} +1 & 0 \\ 0 & -1 \end{pmatrix}, \tag{3}$$

relations (2) for $a = e^{i\varphi/2}\cos\frac{\theta}{2}$ and $b = e^{i\varphi/2}e^{-i\phi}\sin\frac{\theta}{2}$ have the form

$$\begin{aligned} \Psi'(x) &= e^{i\gamma_5\chi/2}e^{i\hat{\kappa}_z\varphi/2}e^{i(-\sin\phi\hat{\kappa}_x + \cos\phi\hat{\kappa}_y)\theta/2}\Psi(x) \\ &= S(\chi)S(\varphi)S(\phi, \theta)\Psi(x), \\ S(\phi, \theta)\hat{\kappa}S^+(\varphi, \theta) &= \hat{\kappa}_z, \\ \hat{\kappa} &= \cos\theta\hat{\kappa}_z + \cos\phi\sin\theta\hat{\kappa}_x + \sin\phi\sin\theta\hat{\kappa}_y, \end{aligned} \tag{4}$$

where

$$\hat{\kappa} = \cos\theta\hat{\kappa}_z + \cos\phi\sin\theta\hat{\kappa}_x + \sin\phi\sin\theta\hat{\kappa}_y.$$

Chiral transformations $S(\chi)$ form the group $U(1)$, and Pauli transformations compose the group $SU(2)$. The latter group includes rotations $S(\varphi)$ about the $\boldsymbol{\kappa}_z$ axis and rotations $S(\phi, \theta)$ of vectors $\boldsymbol{\kappa}$ of the Pauli isospace, which are specified by Euler angles θ and φ, toward the $\boldsymbol{\kappa}_z$ direction. Two-component function $\Psi(x)$ can be also taken in another form. In this case, the form of Pauli transformations (4) must be modified.

The conservation of the form of Pauli transformations under the *CPT* transformation [12, 13] is a natural

Russian Research Centre Kurchatov Institute, pl. Akademika Kurchatova 1, Moscow, 123182 Russia
e-mail: gaponov2@imp.kiae.ru

1028-3358/04/4911-0638$26.00 © 2004 MAIK "Nauka/Interperiodica"

physical condition. This condition leads to the following relation between the phases η_P and η_T of the P and T transformations, respectively:

$$b\left(1+\frac{\eta_P^2}{\eta_T^2}\right)=0,\quad \frac{\eta_P^2}{\eta_T^2}=-1, \tag{5}$$

where $b \neq 0$ is arbitrary. This relation is consistent with the condition $\eta_P^2 = -1$ and $\eta_T^2 = 1$ for the phases of discrete transformations that is usually accepted for physical particles [12]. Fermions satisfying the condition $\eta_P = \pm i$ are called particles of inverse A–B classes [15]. However, another choice of inversion phases (which was first mentioned by Racah [14]) with $\eta_P = \pm 1$ is not excluded for Majorana particles. They are referred to as particles of inverse C–D classes [15], and $\eta_P^2 = 1$ and $\eta_T^2 = -1$ for them. Inverse classes are important for analysis of Majorana properties. Indeed, let us consider the most general Majorana-type conditions

$$\psi^c(x,\zeta) = \lambda e^{i\phi}\psi(x,\zeta), \tag{6a}$$

$$\psi^c(x,\zeta) = \lambda e^{i\phi}\gamma_5\psi(x,\zeta), \tag{6b}$$

where $(\psi^c(x,\zeta) = \gamma_2\gamma_4\overline{\psi}^T(x,\zeta)$ according to [12], λ is a real number, and ζ are quantum numbers. Condition (6a) is a generalization of the Majorana condition, and condition (6b) is its analogue studied below along with the Majorana condition. It is easy to show that condition (6a) is realized for particles of inverse A–B classes (see, e.g., [8]) and condition (6b) is realized for particles of C–D classes. Combinations $\overline{\psi}(x)\psi^c(x)$ and $\overline{\psi}^c(x)\psi(x)$ are scalar for A–B classes and pseudoscalar for C–D classes, whereas combinations $\overline{\psi}(x)\gamma_5\psi^c(x)$ and $\overline{\psi}^c(x)\gamma_5\psi(x)$ are scalar for C–D classes and pseudoscalar for A–B classes. The combinations of the former type or condition (6a) (for $\lambda = 1$) are used in Majorana models [7–9] so that they implicitly imply that particles belong to A–B classes. In what follows, this restriction is removed and Majorana schemes are developed for particles of inverse A–B and C–D classes. For latter classes, the Majorana condition is implied in form (6b).

Let us find the conserving charges associated with transformations (2) for a massless fermion field with the Lagrangian

$$L_0(x) = -\frac{1}{2}[\overline{\Psi}(x)\gamma_\mu\partial_\mu\Psi(x)],\quad \Psi(x)=\begin{pmatrix}\psi(x)\\ \gamma_5\psi^c(x)\end{pmatrix}, \tag{7}$$

where the wave functions are secondarily quantized. In contrast to the form usually used in Majorana models, the generalized function $\Psi(x)$ includes γ_5 in the lower component. The invariance of Lagrangian (7) under chiral and phase (subgroup of Pauli) transformations gives rise to the existence of the conserved chiral and lepton charges

$$\begin{aligned} Q^{CH} &= \frac{1}{2}\int d^3x\Psi^+(x)\gamma_5\Psi(x),\\ Q^L &= Q_z^{\mathrm{P}} = \frac{1}{2}\int d^3x\Psi^+(x)\hat{\kappa}_z\Psi(x),\end{aligned} \tag{8}$$

which specify the characteristics of the generalized function $\Psi(x)$. They include chirality ρ ($\gamma_5\Psi_\rho(y) = \rho\Psi_\rho(y)$) and eigenvalues of $\hat{\kappa}_z$ [$\hat{\kappa}_z\Psi_{\kappa_z}(y) = \kappa_z\Psi_{\kappa_z}(y)$]. We introduce the following set of eigenfunctions depending on ρ and κ_z [$\rho = \pm 1$ (L, R), $\kappa_z = \pm 1$] for the basic operators Q^{CH} and Q_z^{P}:

$$\begin{aligned} (\Psi_0)_{\rho,+1}(x) &= \begin{pmatrix}\psi_{0\rho}(x)\\ 0\end{pmatrix},\quad (\Psi_0)_{\rho,-1}(x)=\begin{pmatrix}0\\ \rho\psi_{0\rho}^c(x)\end{pmatrix},\\ (\Psi_0)_{\kappa_z}(x) &= \Sigma_\rho\Psi_{\rho,\kappa_z}(x),\\ Q_z^{\mathrm{P}} &= \frac{1}{2}\int d^3x(\Psi_0)^+_{\kappa_z}(x)\hat{\kappa}_z(\Psi_0)_{\kappa_z}(x).\end{aligned} \tag{9}$$

As is seen, the operator Q_z^{P} represented in terms of generalized functions is related to the z component of the vector $\boldsymbol{\kappa}$ of the Pauli isospace.

We now consider the group $SU(2)$ of arbitrary pure Pauli transformations ($\chi = 0$) (4), including $S(\varphi)$ and $S(\phi, \theta)$. Lagrangian (7) is invariant under them, and the following general form of a conserved charge is obtained by applying rotation $S^+(\phi, \theta)$ to Eq. (8):

$$\begin{aligned} Q^{\mathrm{P}} &= \frac{1}{2}\int d^3x\Psi^+(x)\hat{\kappa}\Psi(x) = \cos\theta Q_z^{\mathrm{P}}\\ &+ \sin\theta\cos\phi Q_x^{\mathrm{P}} + \sin\theta\sin\phi Q_y^{\mathrm{P}}\\ &= \frac{1}{2}\int d^3x\{\cos\theta[\psi^+(x)\psi(x) - \psi^{c+}(x)\psi^c(x)]\\ &+ \sin\theta[e^{-i\phi}\psi^+(x)\gamma_5\psi^c(x) + e^{+i\phi}\psi^{c+}(x)\gamma_5\psi(x)]\}.\end{aligned} \tag{10}$$

This charge, which includes vector $\boldsymbol{\kappa}$ (4), serves as the generalized lepton charge Q^{P} (below also called Pauli charge) in the Pauli scheme and includes not only Q_z^{P}, but also terms with Q_x^{P} and Q_y^{P}. Its eigenvalues are obtained from Eq. (9) by the transformation $S^+ = S^+(\phi, \theta)$

transforming κ_z to κ and $\Psi_0(x)$ to the eigenfunctions of the operator $\hat{\kappa}$: $\Psi(x) = S^+\Psi_0(x)$ [$\hat{\kappa}\Psi_\kappa(x) = \kappa\Psi_\kappa(x)$]. Quantum numbers ρ do not change, and κ_z are transformed to the quantum numbers κ of the eigenfunctions $\Psi_\kappa(x)$, conserving their values. For the eigenfunctions $\Psi_{\rho,\kappa}(x)$ for fixed $\kappa = \pm 1$, we obtain

$$\Psi_{\rho,+1}(x) = \begin{pmatrix} \cos\frac{\theta}{2}\psi_{0\rho}(x) \\ e^{i\phi}\sin\frac{\theta}{2}\psi_{0\rho}(x) \end{pmatrix},$$

$$\Psi_{\rho,-1}(x) = \begin{pmatrix} -\rho e^{i\phi}\sin\frac{\theta}{2}\psi^c_{0\rho}(x) \\ \rho\cos\frac{\theta}{2}\psi^c_{0\rho}(x) \end{pmatrix}, \qquad (11)$$

$$Q^{\mathrm{P}}(\kappa) = \frac{1}{2}\int d^3x\Psi^+_\kappa(x)\hat{\kappa}\Psi_\kappa(x) = Q^{\mathrm{P}}_z \quad (\kappa_z = \kappa).$$

According to the form of these eigenfunctions, the upper and lower components of the eigenfunctions of the charge Q^{P} for definite κ are related as

$$\Psi_{\rho\kappa}(x) = \begin{pmatrix} \psi_{\rho\kappa}(x) \\ \gamma_5\psi^c_{\rho\kappa}(x) \end{pmatrix},$$

$$\psi^c_{\rho\kappa}(x) = \tan\frac{\theta}{2}e^{i\phi}\gamma_5\psi_{\rho\kappa}(x)$$

$$(\kappa = +1),$$

$$\psi^c_{\rho\kappa}(x) = -\cot\frac{\theta}{2}e^{i\phi}\gamma_5\psi_{\rho\kappa}(x) \quad (\kappa = -1), \qquad (12)$$

$$\psi_\kappa(x) = \Sigma_\rho\psi_{\rho\kappa}(x),$$

$$\psi^c_\kappa(x) = \kappa\tan^\kappa\frac{\theta}{2}e^{i\phi}\gamma_5\psi_\kappa(x).$$

The last relation for $\kappa = 1$ coincides with the generalized Majorana condition given by Eq. (6b) for particles of inverse C–D classes for $\lambda = \tan\frac{\theta}{2}$, so that solutions $\kappa = 1$ are equivalent to Majorana solutions with corresponding $\lambda(\theta)$. The solutions associated with the possible alternative choice of Eq. (12) for $\kappa = -1$ correspond to Eq. (6b) with $\lambda' = -\cot\frac{\theta}{2} = -\frac{1}{\lambda}$ and complement solutions with $\lambda = \tan\frac{\theta}{2}$ to the complete set. Therefore, Majorana conditions (6b) for particles of C–D classes are projection conditions separating solutions in form (3) with the generalized charge $\kappa = \pm 1$ for fixed θ and corresponding $\lambda(\theta)$.

Let us consider particles of inverse A–B classes. In this case, one should take another form of the two-component generalized function $\Phi(x)$ constructed from charge-even/odd ($\eta = \pm 1$) combinations of the L and R components $\psi(x)$ and $\psi^c(x)$. In this case, the form of Pauli transformations (2), as well as the form of the charge Q^{P}_z, changes. For a case similar to Eq. (8), the new generalized function and charge have the form

$$\Phi(x) = \begin{pmatrix} \psi_{\mathrm{L}}(x) + \eta\psi^c_{\mathrm{R}}(x) \\ \psi_{\mathrm{R}}(x) + \eta\psi^c_{\mathrm{L}}(x) \end{pmatrix},$$
$$Q^L = Q^{\mathrm{P}}_z = \frac{1}{2}\int d^3x\Phi^+(x)\hat{\kappa}'_z\gamma_5\Phi(x), \qquad (13)$$

and Pauli transformations (4) take the form:

$$\Phi'(x) = e^{i\gamma_5\chi/2}e^{i\eta(\cos\phi\hat{\kappa}'_y - \sin\phi\hat{\kappa}'_x\gamma_5)\theta/2}e^{i\hat{\kappa}'_z\gamma_5\varphi/2}\Psi(x)$$
$$= S(\chi)S'(\phi, \theta)S'(\varphi)\Phi(x) \qquad (14)$$

($\hat{\kappa}'_i$ differs from $\hat{\kappa}_i$). Functions $\Phi(x)$ are characterized by charge parity η and lepton charge Q^{P}_z, which includes the product $\hat{\kappa}'_z\gamma_5$, so that, along with it there is the quantum number κ'_z alternative to the lepton charge. If $(\Phi_0)_{\kappa'_z}(x)$ are the eigenfunctions of the operator κ'_z, which are constructed in terms of $\psi_{0\rho}(x)$ and $\psi^c_{0\rho}(x)$ as combinations of form (13), then, using Pauli transformations $S'^+(\phi, \theta)$ transforming κ'_z to κ', one can obtain the general form of the generalized lepton charge of the A–B type and eigenfunctions $\Phi_{\kappa',\eta}(x)$ with quantum numbers $\kappa' = \pm 1$, $\eta = \pm 1$:

$$\Phi_{+1,\eta}(x) = \frac{1}{\sqrt{2}}\begin{pmatrix} \cos\frac{\theta}{2}(\psi_{0\mathrm{L}}(x) + \eta\psi^c_{0\mathrm{R}}(x)) \\ \eta e^{i\gamma_5\phi}\sin\frac{\theta}{2}(\psi_{0\mathrm{L}}(x) + \eta\psi^c_{0\mathrm{R}}(x)) \end{pmatrix},$$

$$\Phi_{-1,\eta}(x) = \frac{1}{\sqrt{2}}\begin{pmatrix} -\eta e^{-i\gamma_5\phi}\sin\frac{\theta}{2}(\psi_{0\mathrm{R}}(x) + \eta\psi^c_{0\mathrm{L}}(x)) \\ \cos\frac{\theta}{2}(\psi_{0\mathrm{R}}(x) + \eta\psi^c_{0\mathrm{L}}(x)) \end{pmatrix}, \qquad (15)$$

$$Q^P = \frac{1}{2}\int d^3x\Phi^+(x)\hat{\kappa}'\gamma_5\Phi(x),$$

$$\hat{\kappa}' = \cos\theta\hat{\kappa}'_z + \eta\sin\theta\hat{\kappa}'_x e^{i\gamma_5\hat{\kappa}'_z\phi}.$$

In this case, the generalized lepton charge vanishes for states with fixed κ'. Connections between the upper and lower components of eigenfunctions for fixed κ' provide the relations

$$\psi^c_{\rho\kappa'}(x) = \tan^{\rho}\frac{\theta}{2}e^{i\phi}\psi_{\rho\kappa'}(x) \quad (\kappa' = +1);$$
$$\psi^c_{\rho\kappa'}(x) = -\cot^{\rho}\frac{\theta}{2}e^{i\phi}\psi_{\rho\kappa'}(x) \quad (\kappa' = -1), \qquad (16)$$
$$\rho = \pm 1(L, R).$$

Solutions $\kappa' = 1$ satisfy Majorana conditions (6a) with $\lambda(\theta) = \tan\frac{\theta}{2}$ and $\cot\frac{\theta}{2}$ for L and R components, respectively, and solutions $\kappa' = -1$ satisfy Majorana conditions (6a) with $\lambda'(\theta) = -\frac{1}{\lambda(\theta)}$. For $\theta = \frac{\pi}{2}$ and $\varphi = 0$, at $\kappa' = \pm 1$ this is the Majorana condition $\psi^c(x) = \pm\psi(x)$ [1].

Let us describe Majorana massive neutral particles. For particles of inverse C–D classes with generalized function (3), the mass term of the Lagrangian and the equation for the Dirac case have the form

$$L_{m\mathrm{D}}(x) = -\frac{M}{2}[\overline{\Psi}_{\mathrm{D}}(x)\hat{\kappa}_z\Psi_{\mathrm{D}}(x)], \quad \Psi_{\mathrm{D}}(x) = \begin{pmatrix}\psi_{\mathrm{D}}(x)\\ \gamma_5\psi^c_{\mathrm{D}}(x)\end{pmatrix},$$
$$(\gamma_\mu\partial_\mu + M\hat{\kappa}_z)\Psi_{\mathrm{D}}(x) = 0, \qquad (17)$$
$$Q^{\mathrm{P}}_z = \frac{1}{2}\int d^3x\Psi^+_{\mathrm{D}}(x)\hat{\kappa}_z\Psi_{\mathrm{D}}(x).$$

The mass term includes κ_z and breaks invariance under chiral and total Pauli groups. However, it is invariant under phase subgroup (2) so that the charge Q^{P}_z is conserved. In this case, the Dirac mass is associated with the z axis of the Pauli space.

Let us assume that the Majorana mass terms are generally associated with directions that are separated in the chiral and Pauli subspaces and specified by the chiral angle χ and the Euler angles ϕ and θ. Applying general transformation (4) to Eq. (17), we obtain the mass part of the Lagrangian and generalized lepton charge in the form

$$L_m(x) = -\frac{M}{2}\overline{\Psi}(x)\hat{\kappa}e^{i\gamma_5\chi}\Psi(x),$$
$$Q^{\mathrm{P}} = \frac{1}{2}\int d^3x\Psi^+(x)\hat{\kappa}\Psi(x). \qquad (18)$$

For particles of C–D classes, the mass term and charge include the common operator $\hat{\kappa}$. To compare Eqs. (18) with current Majorana models, we introduce the L and R components of functions and generalized GC conjugation of charge (10), which conserves this Lagrangian but changes the sign of Q^{P}:

$$\psi^{gc}_{\mathrm{R}}(x) = e^{-i(\chi+\phi)}\psi^c_{\mathrm{R}}(x),$$
$$\psi^{gc}_{\mathrm{L}}(x) = e^{+i(\chi-\phi)}\psi^c_{\mathrm{L}}(x).$$

Then, in convenient notation, mass Lagrangian (18) and general equations for any inverse class of particles take the form

$$L_m(x) = -\frac{M}{2}\{\cos\theta(e^{+i\chi}\overline{\psi}_{\mathrm{R}}(x)\psi_{\mathrm{L}}(x)$$
$$+ e^{-i\chi}\overline{\psi}^{gc}_{\mathrm{R}}(x)\psi^{gc}_{\mathrm{L}}(x)) + \sin\theta(\overline{\psi}_{\mathrm{R}}(x)\psi^{gc}_{\mathrm{L}}(x)$$
$$-\overline{\psi}^{gc}_{\mathrm{R}}(x)\psi_{\mathrm{L}}(x)) + \mathrm{h.c.}\}; \qquad (19)$$

$$\gamma_\mu\partial_\mu\psi_\rho(x) + M\cos\theta e^{-i\rho\chi}\psi_{-\rho}(x) - M\rho\sin\theta\psi^{gc}_{-\rho}(x) = 0,$$
$$\gamma_\mu\partial_\mu\psi^{gc}_\rho(x) + M\cos\theta e^{+i\rho\chi}\psi^{gc}_{-\rho}(x) + M\rho\sin\theta\psi_{-\rho}(x) = 0,$$

where $\rho = \pm 1$. This Lagrangian in the general Majorana scheme [8, 9] is equivalent to the special case of particles with opposite Majorana masses $M_{\mathrm{R}} = -M_{\mathrm{L}} = M\sin\theta$ and Dirac mass $|M_{\mathrm{D}}| = M\cos\theta$. In this case, the charge C conjugation changes to the generalized charge GC conjugation.

For particles of inverse A–B classes with generalized function (13), the mass term of the Dirac Lagrangian, equation, and change have the form

$$L_{m\mathrm{D}}(x) = -\frac{M}{2}[\overline{\Phi_{\mathrm{D}}}(x)\hat{\kappa}'_x\Phi_{\mathrm{D}}(x)],$$

$$\Phi_D(x) = \begin{pmatrix} \psi_{DL}(x) + \eta\psi^c_{DR}(x) \\ \psi_{DR}(x) + \eta\psi^c_{DL}(x) \end{pmatrix}, \quad (\gamma_\mu\partial_\mu + M\hat{\kappa}'_x)\Phi_D(x) = 0, \qquad (20)$$

$$Q^P_z = \frac{1}{2}\int d^3x\Phi^+_D(x)\gamma_5\hat{\kappa}'_z\Phi_D(x).$$

The choice of the operator $\gamma_5\hat{\kappa}'_z$ as basic fixes the lepton charge, so that $\rho\kappa'_z = 1$ describes left and right particles and $\rho\kappa'_z = -1$ describes right and left antiparticles. In this case, κ'_z has the meaning of the product of this charge and chirality. However, the lepton charge and mass term are specified by different operators $\gamma_5\hat{\kappa}'_z$ and $\hat{\kappa}'_x$ and cannot be diagonalized jointly. Choosing charge as the basic characteristic, by analogy with Eq. (17), one arrives at the Dirac description (Dirac neutrino). The following general form of the mass term and generalized lepton charge are obtained for such choice in terms of *GC* conjugated functions from Eq. (20) by the general transformation of form (14):

$$L_m(x) = -\frac{M}{2}\bar{\Phi}(x)[\cos\theta\hat{\kappa}'_x e^{i\hat{\kappa}'_z\chi} - \eta\sin\theta\hat{\kappa}'_z]\Phi(x),$$

$$\Phi(x) = \begin{pmatrix} \psi_L(x) + \eta\psi^{gc}_R(x) \\ \psi_R(x) + \eta\psi^{gc}_L(x) \end{pmatrix} = \begin{pmatrix} \psi_L(x) + \eta e^{-i(\chi+\phi)}\psi^c_R(x) \\ \psi_R(x) + \eta e^{i+(\chi-\phi)}\psi^c_L(x) \end{pmatrix}, \qquad (21)$$

$$Q^P = \frac{1}{2}\int d^3x\Phi^+(x)[\cos\theta\hat{\kappa}'_z + \eta\sin\theta\hat{\kappa}'_x e^{i\hat{\kappa}'_z\chi}]\gamma_5\Phi(x).$$

However, for particles of A–B classes, it is possible to diagonalize the mass term rather than the charge. Indeed, transforming Eq. (20) by rotation $S'^+\left(\theta = -\frac{\eta\pi}{2}, \phi = 0\right)$, in the Dirac case, we obtain

$$L_{mD}(x) = -\frac{M}{2}\overline{\Phi'_D}(x)\hat{\kappa}'_z\Phi'_D(x),$$

$$\Phi'_D(x) = \frac{1}{\sqrt{2}}\begin{pmatrix} \psi_D(x) + \eta\psi^c_D(x) \\ -\gamma_5(\psi_D(x) - \eta\psi^c_D(x)) \end{pmatrix}, \quad (\gamma_\mu\partial_\mu + M\hat{\kappa}'_z)\Phi'_D(x) = 0, \qquad (22)$$

$$Q^P = -\frac{1}{2}\int d^3x\Phi'^+_D(x)\hat{\kappa}'_x\gamma_5\Phi'_D(x).$$

Values $\kappa'_z = \pm 1$ distinguish solutions that satisfy the Dirac equation with the condition $\psi^c_D(x) = \eta\psi_D$ and were first obtained by Majorana [1] and solutions with the condition $\psi^c_D(x) = -\eta\psi_D$ that supplement the above solutions. States with fixed values $\kappa'_z = \pm 1$ have zero generalized lepton charge. Deviation from zero arises due to their mixing. The most general case can be obtained from Eq. (21) by introducing an analogue of the parameter θ_{md} of Majorana models as $\theta_{md} = \frac{\pi}{2} + \eta\theta$ (in the operator and wave functions). In this case, the Lagrangian takes the general form that was described in [8, 9] and corresponds to the case $M_R = -M_L$. In the traditional scheme, the Lagrangian is diagonalized by certain unitary transformations. In the case under consideration, these are Pauli transformations (14) reducing the Lagrangian to form (22). Therefore, unitary transformations of Majorana models have the sense of Pauli transformations in the scheme under consideration. Thus, for A–B classes, there are two types of solutions—when either the generalized lepton charge operator or mass operator is diagonalized—so that states of a certain charge are superpositions of Majorana-type states with a fixed mass and vice versa.

In this paper, a Majorana-theory variant that includes left and right states has been analyzed. An alternative scheme for states of different flavors [3, 4] will be presented elsewhere.

ACKNOWLEDGMENTS

I am grateful to E.P. Velikhov for his unwavering interest in and support of the work and to B.V. Danilin, Yu.V. Linde, and S.V. Semenov for stimulating discussions during my long work for the paper.

REFERENCES

1. E. Majorana, Nuovo Cimento **14** (6), 171 (1937).
2. B. M. Pontecorvo, Zh. Éksp. Teor. Fiz. **33**, 549 (1958) [Sov. Phys. JETP **6**, 429 (1958)].
3. Z. Maki, M. Nakagawa, and S. Sakata, Prog. Theor. Phys. **28**, 870 (1962).
4. V. Gribov and B. Pontecorvo, Phys. Lett. A **28**, 493 (1969).
5. S. M. Bilenky and B. M. Pontecorvo, Phys. Lett. A **61**, 248 (1976).
6. H. Fritzsh and P. Menkovsky, Phys. Lett. A **62**, 72 (1976).

7. S. M. Bilenky and B. M. Pontecorvo, Usp. Fiz. Nauk **123**, 181 (1977) [Sov. Phys. Usp. **20**, 776 (1977)].

8. F. Boehm and P. Vogel, *Physics of Massive Neutrinos* (Cambridge University Press, New York, 1987; Mir, Moscow, 1990).

9. E. D. Commins and P. H. Bucksbaum, *Weak Interactions of Leptons and Quarks* (Cambridge University Press, Cambridge, 1983; Énergoatomizdat, Moscow, 1987).

10. Yu. V. Gaponov, Preprint No. 6307/1 (Russian Research Center Kurchatov Institute, Moscow, 2004).

11. W. Pauli, Nuovo Cimento **VI** (1), 204 (1957).

12. A. I. Akhiezer and V. B. Berestetskiĭ, *Quantum Electrodynamics*, 3rd ed. (Nauka, Moscow, 1969; Wiley, New York, 1965).

13. *Niels Bohr and the Development of Physics*, Ed. by W. Pauli (Pergamon Press, London, 1955; Inostrannaya Literatura, Moscow, 1958).

14. G. Racah, Nuovo Cimento **14** (7), 322 (1937).

15. P. T. Matthews, *The Relativistic Quantum Theory of Elementary Particle Interactions* (Rochester, New York, 1957).

Translated by R. Tyapaev

Doklady Physics, Vol. 49, No. 11, 2004, pp. 644–647. Translated from Doklady Akademii Nauk, Vol. 399, No. 1, 2004, pp. 38–41.

MECHANICS

On Stability in the Lyapunov Sense and Rigidity in the Joukowski Sense for Trajectories of Conservative Mechanical Systems

O. V. Druzhinina

Presented by Academician V.V. Rumyantsev April 12, 2004

Received April 28, 2004

INTRODUCTION

In the present paper, we formulate theorems on the stability in the Lyapunov sense and the rigidity in the Joukowski sense for trajectories of conservative mechanical systems with many degrees of freedom. The systems are modeled by the ordinary autonomous multidimensional differential equation of class C^2

$$\frac{dx}{dt} = X(x), \quad x = (x_1, x_2, \ldots, x_n) \in R_x^n, \quad n \geq 2, \quad (1)$$

having the first integral

$$S(x) = 0, \quad (2)$$

where $\operatorname{grad} S(x) \neq 0 \ \forall x \in \{S(x) = 0\}$. Mechanical systems modeled by Eq. (1) with property (2) are referred to as conservative systems.

Relationship $S(x) = 0$ defines an $(n-1)$-dimensional invariant set (integral manifold) for Eq. (1) in space R_x^n.

It is shown that, at certain constraints, autonomous n-dimensional differential equation (1) of class C^2 is equivalent to the autonomous $(n-1)$-dimensional differential equation of class C^1

$$\frac{dz}{dt} = Z(z), \quad Z = (z_1, z_2, \ldots, z_{n-1}) \in R_z^{n-1}, \quad (3)$$

in a sense such that the solutions of one of these equations are in one-to-one correspondence to the solutions of the other equation. A positively stable in the Lyapunov sense ω-periodic solution $\pi(t)$ to Eq. (3) corresponds to a positively stable [with respect to condition (2)] ω-periodic solution $\psi(t)$ to Eq. (1) and *vice versa*.

The aforementioned results were applied to study rigidity in the Joukowski sense for closed geodetic lines in the Riemann space. These lines are defined by the set of the second-order differential equations,

$$\frac{d^2y^i}{dt^2} + \Gamma_{jk}\frac{dy^j}{dt}\frac{dy^k}{dt} = 0, \quad i = 1, 2, \ldots, n. \quad (4)$$

By the change of variables $y^k = x_k$, $\dot{y}^k = x_{n+k}$, $k = 1, 2, \ldots, n$, the above set of equations is reduced to the following set:

$$\frac{dx_k}{dt} = x_{n+k}, \quad \frac{dx_{n+k}}{dt} = -\sum_{j,m}^{n} \Gamma_{jm}^k x_{n+j} x_{n+m}, \quad (5)$$
$$k = 1, 2, \ldots, n,$$

with the first integral in the form

$$F(x) = 0, \quad (2)_1$$
$$F(x) ::= \sum_{i,k}^{n} g_{ik}(x_1, x_2, \ldots, x_n) x_{n+i} x_{n+k} - 1.$$

Here, g_{ik} and Γ_{jm}^i are the components of the metric tensor and of the Cristoffel symbol, respectively, for coordinates $y = (y^1, y^2, \ldots, y^n)$ in the n-dimensional differentiable manifold M with a positive definite Riemann metric.

The properties of stability and rigidity for the trajectories of multidimensional autonomous equations having the first integral were studied in [1–6], etc. The rigidity in the Joukowski sense for trajectories of general dynamical systems was considered, e.g., in [7–13].

THE CONSERVATION OF THE STABILITY IN THE LYAPUNOV SENSE UNDER COORDINATE TRANSFORMATIONS

Let G be a domain (open and connected set) in the R_x^n space and $X(x)$ be a vector function belonging to the C^2 class in domain G.

We denote as $\psi(t)$ a reference (unperturbed) solution to Eq. (1) specified for the entire positive semiaxis

Russian State Open Technical University for Railway Transportation, Chasovaya ul. 22/2, Moscow, 125993 Russia

1028-3358/04/4911-0644$26.00 © 2004 MAIK “Nauka/Interperiodica”

$R^+ = [0, +\infty)$ such that $\psi(0) = \psi^0$, $\psi(t) \in G\ \forall t \in R^+$ and also denote as $x(t, x^0)$ an arbitrary solution to Eq. (1) meeting the initial condition $x(0, x^0) = x^0$.

Then, we represent equation $S(x) = 0$ in the parametric form

$$x_i = x_i(z_1, z_2, \ldots, z_{n-1}), \quad (z_1, z_2, \ldots, z_{n-1}) = z \in D, \quad (6)$$

where D is a domain of z-space R_z^{n-1}. We also assume that vector function $x(z)$ in domain G belongs to the C^2 class and, in addition,

$$\operatorname{Rang}\left\|\frac{\partial x}{\partial z}\right\| = n-1, \quad S(x(z)) \equiv 0,$$

where $\operatorname{Rang}\|\cdot\|$ denotes the rank of matrix $\|\cdot\|$.

Theorem 1. *Under the above assumptions, we consider the mapping*

$$\sigma : z \to x(z), \quad \sigma(D) ::= \hat{G} \subset G.$$

Let $x(t, x^0)$ denote the solution to Eq. (1) *such that*

$$x^0 \in \hat{G}, \quad \sigma^{-1}(x^0) = z^0 \in D, \quad S(x^0) = 0.$$

Then, there exists a unique solution $z(t)$, $t \in (-t_1, t_1)$, $t_1 > 0$ to autonomous $(n-1)$-dimensional equation (3) *derived from the set of ordinary equations with respect to* $\frac{dz_k}{dt}$, $k = 1, 2, \ldots, n-1$,

$$\sum_{k=1}^{n-1} \frac{\partial x}{\partial z_k}\frac{dz_k}{dt} = X(x(z)), \quad z \in D, \quad (7)$$

where $x(t, x^0) = x(z(t))$, $\forall t \in (-t_1, t_1)$, $z(0) = z^0$. And, inversely, if $z(t)$ is a solution to $(n-1)$-dimensional equation (3)*, then $x(z)$ at $z = z(t)$ is a solution to n-dimensional equation* (1).

Concept for the proof. For definiteness, we assume that $\frac{\partial(x_1, x_2, \ldots, x_{n-1})}{\partial(z_1, z_2, \ldots, z_{n-1})} \neq 0$, $x \in D$. We consider the set of equations $x_i(t, x^0) = x_i(z_1, z_2, \ldots, z_{n-1})$, $i = 1, 2, \ldots, n$ with respect to $z = (z_1, z_2, \ldots, z_{n-1})$. From the first $n-1$ equations, we can unambiguously determine $z_1, z_2, \ldots, z_{n-1}$ as continuously differentiable functions of $x_i(t, x^0)$, $i = 1, 2, \ldots, n-1$ in the vicinity of point $(x_1^0, x_2^0, \ldots, x_{n-1}^0)$ and as functions of t at $t \in (-t_1, t_1)$ belonging to class C^1, where $t_1 > 0$. It is easy to understand that the last nth equation of the set identically holds true. Function $z(t) = (z_1(t), z_2(t), \ldots, z_{n-1}(t))$ meets the set of equations (7) and Eq. (3). Following this line of reasoning in inverse order, we prove the second statement of the theorem.

Next, we define the modulus $|x|$ of vector x by the relationship $|x| = \max|x_i|$, $i = 1, 2, \ldots, n$.

Definition 1. Solution $\psi(t)$ of Eq. (1) with the initial condition $\psi^0 = \psi(0)$ is referred to as *positively stable in the Lyapunov sense with respect to integral set* (2) if (*1*) there exists $h > 0$ such that each solution $x(t, x^0)$ to Eq. (1) for which $|x^0 - \psi^0| < h$ and $S(x^0) = 0$ is defined on the entire semiaxis R^+; and (*2*) for a given number $\varepsilon > 0$, there exists a number $\delta \in (0, h)$ such that

$$|x^0 - \psi^0| < \delta \wedge S(x^0) = 0$$
$$\Rightarrow |x(t, x^0) - \psi(t)| < \varepsilon \quad \forall t \in R^+.$$

Theorem 2. *Let the hypothesis of Theorem 1 be met. Let $z = \pi(t)$, $t \in R^+$ be an ω-periodic solution to $(n-1)$-dimensional equation* (3) *positively stable in the Lyapunov sense and embedded into domain $D \subset R_z^{n-1}$. Then, the ω-periodic solution $\psi(t) = x(\pi(t))$ to n-dimensional equation* (1) *is positively stable in the Lyapunov sense with respect to integral set* (2).

Proof. We denote the solution to Eq. (3) as $z(t, z^0)$, $z(0, z^0) = z^0$. Let number $\varepsilon > 0$ be specified and x^0 be such that

$$\exists h > 0 \quad |x^0 - \psi^0| < h, \quad S(x^0) = 0. \quad (8)$$

We now prove that there exists a number $\delta \in (0, h)$ such that, from inequality $|x^0 - \pi^0| < \delta$, it follows that

$$|x(t, x^0) - \psi(t)| = |x(z(t, z^0)) - x(\pi(t))| < \varepsilon \quad (9)$$

under the condition

$$|z(t, z^0) - \pi(t)| < \eta \quad \forall t \in R^+. \quad (10)$$

Since $\pi(t)$ is positively stable in the Lyapunov sense, there exists a number $\mu > 0$ such that, at $|z^0 - \pi^0| < \mu$, the solution $z(t, z^0)$ to Eq. (3) is specified on the entire R^+ semiaxis. We choose a bounded domain Π such that $\pi(t) \in \Pi\ \forall t \in R^+$, $\bar{\Pi} \subset D$, where the bar above a symbol denotes the closure. We choose number $\mu > 0$ in a manner such that the following implication is met:

$$|z^0 - \pi| < \mu \Rightarrow z(t, z^0) \in \Pi \quad \forall t \in R^+.$$

Let $x(t, x^0)$ be a solution to Eq. (1) belonging to integral set (2). Then, according to Theorem 1, there exists a solution $z(t, z^0)$ to Eq. (3) such that

$$x(t, x^0) = x(z)|_{z = z(t, z^0)} = x(z(t, z^0)), \quad (11)$$

at $t \in (-t_1, t_1)$, $t_1 > 0$. Hence, we have

$$x^0 = x(0, x^0) = x(z(0, z^0)) = x(z^0). \quad (12)$$

It is easy to understand that, by virtue of Eq. (12), z^0 is a continuous function of x^0 in the vicinity of ψ^0 and there exists $h > 0$ such that $|z^0 - \psi^0| < \mu$ when

$|x^0 - \psi^0| < h$, $S(x^0) = 0$. Therefore, solution $z(t, z^0)$ entering into Eq. (11) can be extended to the entire semiaxis R^+, and since in $z(t, z^0) \in \Pi \subset D$, function $x(z(t, z^0))$ is also defined on R^+ and is a solution to Eq. (1) on R^+. Hence, if conditions (8) are met, solution $x(t, x^0)$ is defined on R^+. Let x^0 meet conditions (8) and $\varepsilon > 0$ be an arbitrary number. Then, there exists a number $\eta > 0$ such that Eq. (9) is valid if condition (10) is met. Owing to the positive stability of solution $\pi(t)$, condition (10) is valid for arbitrary $\eta > 0$ if inequality $|z^0 - \pi^0| < \lambda < \mu$ is met for sufficiently small $\lambda > 0$. The described situation takes place if

$$|x^0 - \psi^0| < \delta < h, \tag{13}$$

where number $\delta > 0$ is sufficiently small. Therefore, it is possible to find a number $\delta \in (0, h)$ such that Eq. (9) follows from Eq. (13). This implies that solution $\psi(t)$ to Eq. (1) is stable with respect to set (2). Thus, Theorem 2 is proved.

CRITERION OF THE CONDITIONAL STABILITY IN THE LYAPUNOV SENSE FOR A PERIODIC SOLUTION TO Eq. (1)

Let $\psi(t)$ and $\pi(t)$ be ω-periodic solutions to Eqs. (1) and (3), respectively. Let $\Phi(t)$ be the fundamental matrix for the solution of the equation in variations with respect to solution $\pi(t)$ to Eq. (3). The eigenvalues ρ_i, $i = 1, 2, \ldots, n-1$, of matrix $C = \Phi(\omega)$ are referred to as multiplicators of the ω-periodic solution $\pi(t)$ to Eq. (3).

It is well known [14] that vector $Z(z)$ in the right-hand side of Eq. (3) is an eigenvector of the monodromy matrix for the periodic solution $\pi(t)$ corresponding to the eigenvalue equal to +1.

Theorem 3. *Let 1, $\rho_2, \rho_3, \ldots, \rho_{n-1}$ be multiplicators of the ω-periodic solution $\pi(t)$ to $(n-1)$-dimensional equation* (3). *In absolute value, the multiplicators $\rho_2, \rho_3, \ldots, \rho_{n-1}$ are smaller than unity. Then, an ω-periodic solution $\psi(t)$ to n-dimensional equation* (1) *corresponding to the ω-periodic solution $\pi(t)$ is positively stable in the Lyapunov sense with respect to invariant set* (2).

Theorem 3 is a corollary of Theorem 2.

Theorem 4. *Let $n = 3$. We consider the two-dimensional equation* (3) *of the form* $\frac{dz}{dt} = Z(z)$, $Z(z) = (Z_1(z), Z_2(z))$. *Then, an ω-periodic solution $\psi(t)$ to three-dimensional equation* (1) *is positively stable in the Lyapunov sense with respect to integral set* (2) *if the functions $Z_1(z)$ and $Z_2(z)$ meet the condition*

$$\int_0^\omega [Z'_{1z_1}(\pi(t)) + Z'_{2z_2}(\pi(t))]dt < 0, \tag{14}$$

where Z'_{iz_j}, $i = j = 1, 2$, are partial derivatives of functions $Z_i(z_1, z_2)$ with respect to z_j and $\pi(t)$ is an ω-periodic motion of the two-dimensional system $\frac{dz_i}{dt} = Z_i(z_1, z_2)$, $i = 1, 2$.

Indeed, if condition (14) is met, then the ω-periodic solution $\pi(t)$ to Eq. (3) (in view of the Poincaré criterion [14]) is positively stable in the Lyapunov sense and, by virtue of Theorem 3, an ω-periodic solution $\psi(t)$ to Eq. (1) is positively stable in the Lyapunov sense with respect to invariant set (2).

CRITERION OF RIGIDITY IN THE JOUKOWSKI SENSE FOR A CLOSED GEODETIC LINE OF SET OF EQUATIONS (4)

Let M be an n-dimensional differentiable manifold with positively defined Riemann metrics and N be a natural coordinate neighborhood of manifold M with metric tensor g_{ik} and the Cristoffel symbols Γ^i_{ik} in the coordinate system $y = (y_1, y_2, \ldots, y_n)$.

We consider the equation $y = \gamma^0(s)$, $s \in R^+$ for the closed geodetic line corresponding to the natural parameterization, where s is the arc length. The natural parameterization is characterized by the condition that the norm of the tangent vector $\dot\gamma^0(s)$ is identically equal to unity, i.e.,

$$g_{ik}(\gamma^0(s))\dot\gamma^{0i}(s)\dot\gamma^{0k}(s) \equiv 1. \tag{15}$$

Suppose that the geodetic line

$$\Gamma ::= \{y = \gamma^0(s): 0 \le s < \infty\}, \quad \gamma^0(s + \omega) = \gamma^0(s), \tag{16}$$

is contained within the coordinate neighborhood N, i.e. $\Gamma \subset N$. Let $y = \gamma(s, y^0, \dot y^0)$ be the equation of an arbitrary geodetic line also corresponding to the natural parameterization, where $\gamma(0, y^0, \dot y^0) = y^0$, $\dot\gamma(0, y^0, \dot y^0) = \dot y^0$, and s is the arc length.

Definition 2. *A closed geodetic line Γ is referred to as rigid in the Joukowski sense if the following conditions are met*: (*1*) *it is possible to find a number $\rho > 0$ such that, from inequalities*

$$|y^0 - \gamma^0(0)| < \rho, \quad |\dot y^0 - \dot\gamma^0(0)| < \rho, \tag{17}$$

it follows that γ^0 is specified for all values of $s \in R^+$ and $\gamma^0(s, y^0, \dot y^0) \in N$ and (*2*) *for an arbitrary chosen num-*

ber $\varepsilon > 0$, *it is possible to find numbers* $\delta > 0, \delta < \rho$ *such that*

$$\begin{aligned} &|y^0 - \gamma^0(0)| < \delta \wedge |\dot{y}^0 - \dot{\gamma}^0(0)| < \delta \\ &\Rightarrow |\gamma(s, y^0, \dot{y}^0) - \gamma^0(s)| < \varepsilon, \\ &|\dot{\gamma}(s, y^0, \dot{y}^0) - \dot{\gamma}^0(s)| < \varepsilon \quad \forall s \in [0, \infty). \end{aligned} \tag{18}$$

From Definition 2, it follows that if the geodetic line Γ is rigid in the Joukowski sense in one admissible coordinate system, then it also is rigid in the other admissible coordinate system.

It is well known [7, 9] that closed geodetic lines meet a set of equations of form (4). Let $x = (x_1, x_2, x_{2n})$ be a vector defined by the relationships $x_k = y^k$, $x_{n+k} = \dot{y}^k$, $k = 1, 2, \ldots, n$. Then, the normal Cauchy form of set (4) takes the form corresponding to Eq. (5).

A solution to set (4) or to set (5) corresponds to the geodetic line Γ, but it is not necessarily specified in the form corresponding to the natural parameterization. Parameter t involved in Eq. (4) is the arc length if and only if, along with the solution γ to Eq. (4), the identity

$$g_{ik}(\gamma(t))\dot{\gamma}^i(t)\dot{\gamma}^k(t) \equiv 1 \tag{19}$$

is met, i.e., if and only if along with the corresponding solution to set (5), we have

$$\sum_{i,k=1}^{n} g_{ik}(x_1, x_2, \ldots, x_n)x_{n+i}x_{n+k} \equiv 1. \tag{20}$$

If the geodetic line Γ meets the set of equations (5), the tangent vector has the constant length, but it should not necessarily be the unit vector: $g_{ik}\dot{y}^i\dot{y}^k = \text{const}$. This implies that Eq. $(2)_1$ is the first integral of the set of equations (5), and equality $F(x) = 0$ determines an invariant manifold.

If the geodetic line Γ is specified by means of natural parameterization, its trajectory lies in the invariant manifold $F(x) = 0$, and the rigidity of this geodetic line is equivalent to stability in the Lyapunov sense with respect to the solutions with the trajectories lying within this manifold.

Therefore, the following theorem holds.

Theorem 5. *A closed geodetic line* Γ *of the set of second-order equations* (4) *is rigid in the Joukowski sense if and only if the corresponding* ω*-periodic solution to normal set of equations* (5) *is positively stable in the Lyapunov sense with respect to the integral set* $F(x) = 0$.

ACKNOWLEDGMENTS

The author is grateful to Prof. A.A. Shestakov and Academician V.V. Rumyantsev for their attention to this study.

REFERENCES

1. A. M. Lyapunov, *General Problem on the Stability of Motion* (Gostekhizdat, Moscow, 1950).
2. N. E. Joukowski, *Complete Collection of Papers* (ONTI NKTP, Moscow, 1937), Vol. 1, p. 110.
3. N. G. Chetaev, Prikl. Mat. Mekh. **20**, 309 (1956).
4. V. I. Vorotnikov and V. V. Rumyantsev, *Stability and Control with Respect to a Part of the Coordinates for the Phase Vector in Dynamical Systems* (Nauchnyĭ Mir, Moscow, 2001).
5. V. I. Zubov, *Analytical Dynamics of Gyroscopic Systems* (Sudostroenie, Leningrad, 1970).
6. V. D. Irtegov, *Invariant Manifolds of Stationary Motions and Their Stability* (Nauka, Novosibirsk, 1985).
7. J. L. Synge, *Tensor Methods in Dynamics* (Inostr. Lit., Moscow, 1947).
8. M. Sh. Aminov, Trudy Kazan. Aviats. Inst. **24**, 3 (1947).
9. T. Levi-Civita, Math. Ann. **97**, 291 (1926).
10. G. A. Leonov and D. V. Ponomarenko, Izv. Vuzov. Ser. Mat. **4** (371), 88 (1993).
11. O. V. Druzhinina and A. A. Shestakov, *The Rigidity of Motion for Mechanical Systems* (RUDN–PAIMS, Moscow, 1996).
12. O. V. Druzhinina, Dokl. Akad. Nauk **388**, 189 (2003) [Dokl. Phys. **48**, 38 (2003)].
13. O. V. Druzhinina and A. A. Shestakov, Dokl. Akad. Nauk **393**, 478 (2003) [Dokl. Phys. **48**, 674 (2003)].
14. B. P. Demidovich, *Lectures on the Mathematical Theory of Stability* (Nauka, Moscow, 1967).

Translated by K. Kugel

Doklady Physics, Vol. 49, No. 11, 2004, pp. 648–652. Translated from Doklady Akademii Nauk, Vol. 399, No. 1, 2004, pp. 42–46.

MECHANICS

The Lagrangian Approach to Solving the Time-Dependent Navier–Stokes Equations

G. Ya. Dynnikova

Presented by Academician G.G. Chernyĭ April 15, 2004

Received April 22, 2004

In this paper, the Navier–Stokes equations are reduced to an integro-differential form, which allows the method of discrete vortices to be generalized for viscous two-dimensional incompressible flows. It is shown that, in the case when infinite vortex refinement occurs, the equations describing the evolution of the vorticity field as a result of vortex motion tend to the Navier–Stokes equations. The expressions that relate aerodynamic forces (including friction) to characteristics of moving vortices are derived. Testing the method with the consideration of flows around both a longitudinal thin plate and a transverse circular cylinder at different Reynolds numbers is consistent with the known results.

In its original form, the Lagrangian method of describing a continuum is intended to trace displacements of particles marked with a certain set of parameters, i.e., with Lagrangian variables [1–3]. These variables can be presented, for example, by the initial coordinates of the particles. The Lagrangian representation of hydrodynamic equations is commonly used for investigating a perfect fluid, where vortex tubes can be considered to be frozen into the fluid flow [4–10].

In a viscous fluid, the velocity circulation along an arbitrary contour moving with a fluid, as a rule, is not conserved. However, in the case of two-dimensional viscous incompressible flows, the hydrodynamic equations can be reduced to a form that admits the usage of Lagrangian coordinates. For these flows, the term $\nu\Delta\mathbf{V}$ entering into the Navier–Stokes equation can be presented as [11]

$$\nu\Delta\mathbf{V} = \mathbf{V}_d \times \boldsymbol{\Omega}, \quad \mathbf{V}_d = \frac{\nu \operatorname{curl}\boldsymbol{\Omega} \times \boldsymbol{\Omega}}{\Omega^2},$$

where ν is the kinematic viscosity, $\mathbf{V}$ is the fluid velocity, and $\boldsymbol{\Omega} = \operatorname{curl}\mathbf{V}$.

Institute of Mechanics, Moscow State University, Michurinskiĭ pr. 1, Moscow, 117234 Russia

For a plane-parallel flow, the vector $\mathbf{V}_d$ can be presented as [12]

$$\mathbf{V}_d = -\left(\frac{\nu}{\Omega}\right)\nabla\Omega. \tag{1}$$

The action of the curl operator on the Navier–Stokes equation transforms it into the form

$$\frac{\partial\boldsymbol{\Omega}}{\partial t} = \operatorname{curl}((\mathbf{V} + \mathbf{V}_d) \times \boldsymbol{\Omega}) = -\operatorname{div}((\mathbf{V} + \mathbf{V}_d)\Omega)\mathbf{e}_\Omega,$$

which describes the evolution of vorticity field Ω.

The circulation along a contour with each of its points moving at a velocity $\mathbf{V} + \mathbf{V}_d$ remains constant. This fact allows the application of the Lagrangian approach while considering the motion of elementary contours with the conserved velocity circulation.

In contrast to a perfect fluid, these contours are not frozen into the flow and move with respect to the fluid under consideration at a velocity $\mathbf{V}_d$, which is called the diffusion velocity in [12]. The Eulerian coordinates of the observed elementary contours can be considered as functions of the Lagrangian coordinates and time and as satisfying the equations

$$\frac{\partial\mathbf{r}(L_i, t)}{\partial t} = \mathbf{V} + \mathbf{V}_d.$$

The Lagrangian variables L_i can be presented by either vortex coordinates $\mathbf{R}_0$ at the zero time or coordinates and times of the vortex origination on the surface. In the first case, the circulation element is $d\boldsymbol{\Gamma} = \boldsymbol{\Omega}\,dx_0dy_0$, while in the second case, $d\boldsymbol{\Gamma} = \mathbf{J}\,dl\,dt$, where $\mathbf{J}$ is the vorticity flow per unit area of the surface at the contour point l.

Vorticity-flow density $\mathbf{J}(l, t)$ is determined by boundary conditions imposed on the fluid velocity at the surface. If the coordinate system is immobile with respect to a certain infinite point, fluid velocity $\mathbf{V}(\mathbf{R}, t)$ can be expressed by the Biot–Savart formula in terms of

1028-3358/04/4911-0648$26.00

both the spatial vorticity distribution and velocity difference $\mathbf{V}_+ - \mathbf{V}_-$ occurring on the discontinuity surfaces

$$\mathbf{V}(\mathbf{R}, t) = \int_\Gamma \mathbf{K} \times d\mathbf{\Gamma} + \int_l \mathbf{K} \times d\boldsymbol{\gamma}, \quad \mathbf{K} = \frac{1}{2\pi} \frac{\mathbf{r} - \mathbf{R}}{|\mathbf{r} - \mathbf{R}|^2}, \qquad d\boldsymbol{\gamma} = (\mathbf{V}_+ - \mathbf{V}_-) \times \mathbf{n} dl. \tag{2}$$

Here, $\mathbf{n}$ is a normal to the surface, l is the coordinate measured along the surface, and $\mathbf{r}$ is the radius vector of either the vortex element $d\mathbf{\Gamma}$ or $d\boldsymbol{\gamma}$.

The boundary condition relating flow density $\mathbf{J}$ to both the spatial vorticity distribution and surface velocity $\mathbf{V}_s(l, t)$ is determined by impermeability and adherence (or slip) conditions. The adherence condition requires that $\boldsymbol{\gamma} = 0$. Then, under the assumption that the surface is impermeable at the zero time, the impermeability condition takes the form

$$\left.\frac{\partial}{\partial t}\right|_l \mathbf{V}_s(l, t) \cdot \mathbf{n}_l = \int_\Gamma \left.\frac{\partial}{\partial t}\right|_l \mathbf{n}_l \cdot \mathbf{K} \times d\mathbf{\Gamma} + \mathbf{n}_l \cdot \oint_l \mathbf{K} \times \mathbf{J} dl.$$

In the framework of the Lagrangian approach, the calculation of the diffusion velocity expressed in terms of derivatives with respect to the Eulerian coordinates is rather difficult. To calculate the functions $\Omega(\mathbf{R}, t)$ and $\nabla\Omega$, we use here the following integral approximations:

$$\Omega(\mathbf{R}) = \frac{I_1}{I_0} + O(\varepsilon),$$

$$\nabla\Omega(\mathbf{R}) = \frac{\mathbf{I}_2}{I_0} - \frac{\mathbf{I}_3 I_1}{I_0^2} + O(\varepsilon);$$

$$I_1(\mathbf{R}) = \int_S \Omega(\mathbf{r}) \exp\left(-\frac{|\mathbf{R} - \mathbf{r}|}{\varepsilon}\right) ds,$$

$$I_0(\mathbf{R}) = \int_S \exp\left(-\frac{|\mathbf{R} - \mathbf{r}|}{\varepsilon}\right) ds, \tag{3}$$

$$\mathbf{I}_2(\mathbf{R}) = -\int_S \frac{\mathbf{R} - \mathbf{r}}{|\mathbf{R} - \mathbf{r}|\varepsilon} \Omega(\mathbf{r}) \exp\left(-\frac{|\mathbf{R} - \mathbf{r}|}{\varepsilon}\right) ds,$$

$$\mathbf{I}_3(\mathbf{R}) = -\int_S \frac{\mathbf{R} - \mathbf{r}}{|\mathbf{R} - \mathbf{r}|\varepsilon} \exp\left(-\frac{|\mathbf{R} - \mathbf{r}|}{\varepsilon}\right) ds$$

(the formally small parameter ε is discussed below). Expanding the function $\Omega(\mathbf{r})$ into a series at point $\mathbf{R}$, we can show that Eqs. (3) are satisfied for an arbitrary smooth function $\Omega(\mathbf{r})$. Using these equations, we can express diffusion velocity $\mathbf{V}_d$ by the formula

$$\mathbf{V}_d = -\nu \frac{\mathbf{I}_2}{I_1} + \nu \frac{\mathbf{I}_3}{I_0}. \tag{4}$$

As $\Omega(\mathbf{R}, t) ds = d\Gamma$, integration in the expressions for I_1 and $\mathbf{I}_2$ can be performed in terms of the Lagrangian coordinates. In the course of numerical solution, we substitute integration by summation over vortex elements $\Delta\Gamma_i$. The error caused by this substitution has the order of magnitude $\frac{\Delta r_i}{\varepsilon}$, where Δr_i is the characteristic linear size of regions Δs_i in space S. Therefore, while choosing the parameter ε, we should simultaneously satisfy the following two conditions: $\varepsilon \gg \Delta r_i$ and ε being much smaller than the characteristic scale of the region where both the function Ω and its gradient vary by the order of their magnitude, respectively. The infinite refinement of vortex regions allows both conditions to be satisfied with a required accuracy.

The integrals I_0 and $\mathbf{I}_3$ are dependent only on the flow-region configuration and coordinates $\mathbf{R}$. If the distance between point $\mathbf{R}$ and the surface significantly exceeds ε, then the term $\frac{\mathbf{I}_3}{I_0}$ tends to zero. The integral $\mathbf{I}_3$ can be transformed into the contour integral

$$\nu \frac{\mathbf{I}_3}{I_0} = \oint \mathbf{I}_w dl, \quad \mathbf{I}_w(\mathbf{R}, \mathbf{r}(l)) = -\nu \frac{\mathbf{n}}{I_0(\mathbf{R})} \exp\left(-\frac{|\mathbf{R} - \mathbf{r}|}{\varepsilon}\right),$$

where $\mathbf{n}$ is the normal to the contour surface, which is directed from the fluid to the body. The vector $\mathbf{I}_w dl$ can be interpreted as a contribution of contour element dl to the diffusion velocity. This contribution is directed along the normal to the contour and describes repulsion from it. The first term in (4) can be considered as a result of interaction of vortex elements. Here, a contribution of the element $d\mathbf{\Gamma}_1$ situated at point $\mathbf{r}_1$ to the diffusion velocity of the element $d\mathbf{\Gamma}_2$ situated at point $\mathbf{r}_2$ is described by the expression $\mathbf{I}_{int}(\mathbf{r}_1, \mathbf{r}_2)\, d\mathbf{\Gamma}_1$, where

$$\mathbf{I}_{int} = \nu \frac{\mathbf{r}_2 - \mathbf{r}_1}{|\mathbf{r}_2 - \mathbf{r}_1| I_0 \varepsilon} \exp\left(-\frac{|\mathbf{r}_2 - \mathbf{r}_1|}{\varepsilon}\right) d\mathbf{\Gamma}_1. \tag{5}$$

According to (5), the vector $\mathbf{I}_{int}$ is directed along the line connecting vortex elements and describes repulsion and attraction for vortices having identical and opposite directions, respectively.

The integral representation of the diffusion velocity that is proposed in this study is not unique—e.g., in [12], another expression for $\mathbf{V}_d$ was suggested. However, as is shown in [13] by considering the Rankine vortex diffusion, the representation of [12] results in vortex "adhesion" due to a nonmonotone character of mutual vortex repulsion (the repulsion rate tends to zero

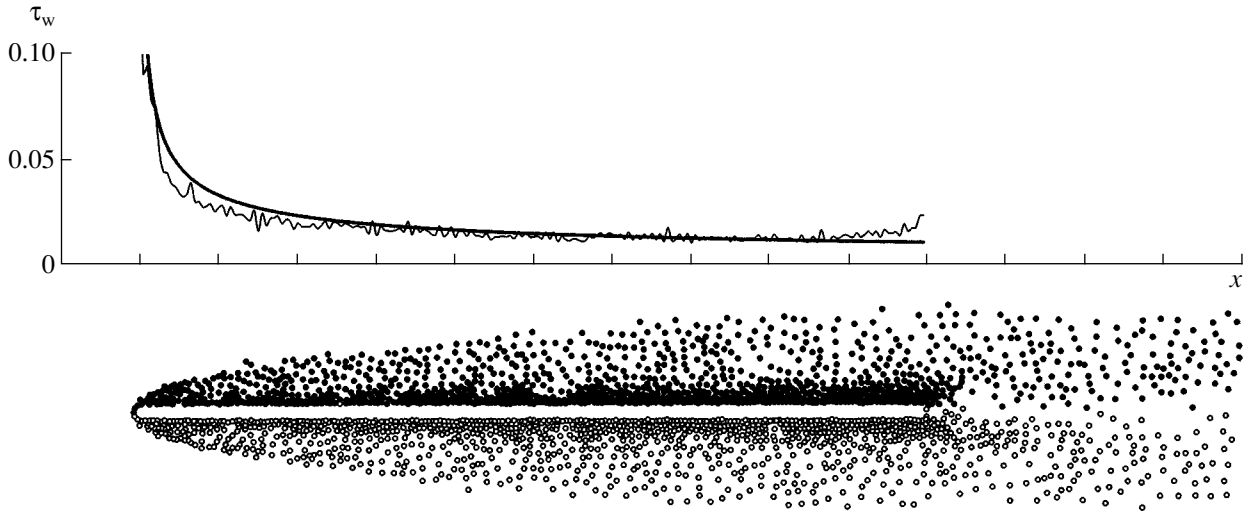

Fig. 1. Positions of vortex elements and friction-stress distribution for a flow around a thin plate.

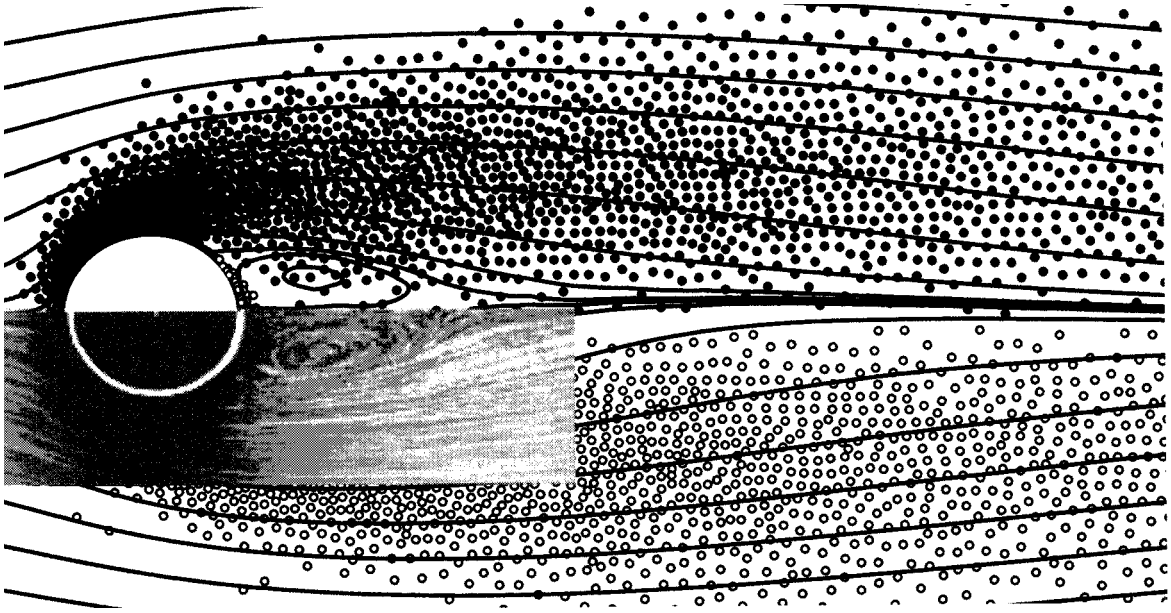

Fig. 2. Flow around a circular cylinder at Re = 26 with a fragment of the photograph taken in [14], which shows the experimental pattern of flow around a cylinder at the same value of the Reynolds number Re.

as the vortices approach each other). Moreover, in [12], the correct allowance for the effect of a surface with a flow around it on the diffusion velocity is absent.

As is shown in [10], in the absence of other forces acting on a body in the case of flow around it, force **F** applied to the body is related to hydrodynamic impulse **I** by the formula

$$\mathbf{F} = -\frac{d\mathbf{I}}{dt} - \rho\frac{d}{dt}\oint \mathbf{r}\times(\mathbf{V}\times\mathbf{n})\,dl,$$

where the hydrodynamic impulse is represented by the expression

$$\mathbf{I} = \rho\int_S \mathbf{r}\times\boldsymbol{\Omega}\,ds. \tag{6}$$

For translational uniform motion of the body and the adherence condition being satisfied, differentiating expression (6) and using formulas (2)–(4), we arrive at

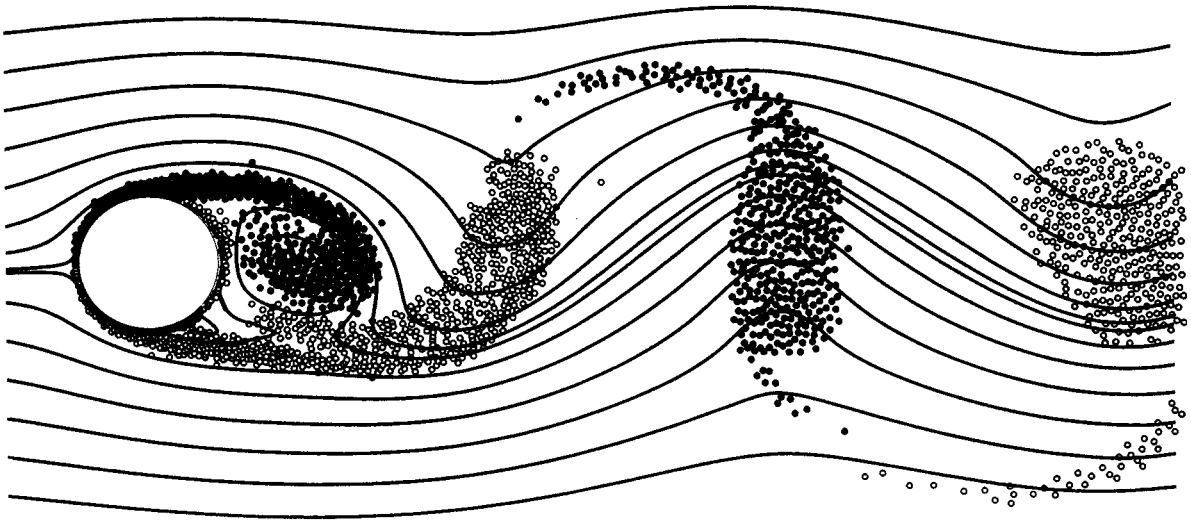

Fig. 3. Flow around a circular cylinder for the Reynolds number Re = 1000.

the following relation:

$$\mathbf{F} = -\rho\oint_{l}\mathbf{r}\times\mathbf{J}\,dl - \rho\int_{\Gamma}\mathbf{V}_{\mathrm{d}}\times d\boldsymbol{\Gamma},$$

where the first and the second terms are the resultants of pressure forces and of friction forces, respectively. Friction stress $\boldsymbol{\tau}_w$ is expressed by the formula

$$\boldsymbol{\tau}_{\mathrm{w}}(l) = -\rho\int_{\Gamma}\mathbf{I}_{\mathrm{w}}\mathbf{r}((l),\mathbf{r}(\Gamma))\times d\boldsymbol{\Gamma}.$$

Figures 1–4 present some results of calculations performed with the use of the proposed method. Figure 1 shows positions of observed Lagrangian particles (of vortex elements) and the distribution of the friction stress along a thin plate directed along the flow. The light and dark circles correspond to vortices with positive and negative signs of circulation, respectively. The Reynolds number calculated by using the plate length is equal to 1000. The thickness of the plate is equal to 2% of its length. The leading edge has the shape of a semicircle. The friction stress calculated by the Prandtl theory (Fig. 1, thick solid line) agrees well with the results obtained in our study. The small discrepancies occurring near the leading and trailing edges are associated, it appears, with a finite plate thickness.

Figures 2 and 3 present streamlines and positions of vortex elements in flows around a circular cylinder at Re = 26 and 1000. In addition, Fig. 2 contains a fragment of a photograph (taken from [14]) that shows the experimental flow pattern around a cylinder at Re = 26.

Figure 4 presents a drag coefficient for a cylinder at different values of Re according to both this calculation and data of other authors, which were taken from [15].

Thus, the Navier–Stokes equations are reduced to a form that allows application of the Lagrangian approach to the calculation of plane time-dependent viscous incompressible-fluid flows. The diffusion velocity of vortices with respect to fluid particles is represented as an integral taken over all vortices, where the contribution of a single vortex element to the diffusion velocity of another element has the character of repul-

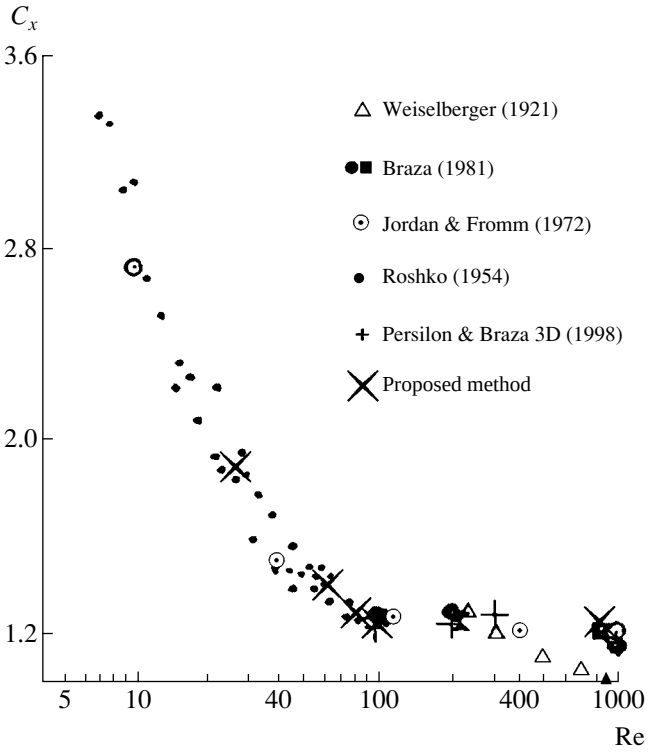

Fig. 4. Drag coefficient for a circular cylinder as a function of the Reynolds number.

sion (or attraction) for vortices of identical (or opposite) directions. In the vicinity of the body's surface, the contribution of the surface to the diffusion velocity has the form of repulsion from the surface. The expressions for hydrodynamic forces, including friction, are derived for a body with a flow around it. The method developed does not require constructing calculation grids, and, thereby, it considerably simplifies the calculation procedure. Therefore, this method can be successfully used for solving problems involving time-dependent flow geometry.

ACKNOWLEDGMENTS

The author is grateful to S.V. Guvernyuk and P.R. Andronov for fruitful discussions and their help in performing this study.

This work was supported by the Russian Foundation for Basic Research (project nos. 02-01-00670 and 04-01-00554) and by the Russian–Belarussian SKIF Program.

REFERENCES

1. G. Kirchhoff, *Mechanics* (Izd. Akad. Nauk SSSR, Moscow, 1962).
2. G. Lamb, *Hydrodynamics* (Gostekhizdat, Moscow, 1947).
3. N. E. Kochin, I. A. Kibel', and N. V. Roze, *Theoretical Hydromechanics* (Fizmatgiz, Moscow, 1963), Part 1.
4. J. T. Stuart and M. Tabor, Phil. Trans. Roy. Soc. A (London) **333** (1631), 263 (1990).
5. A. A. Abrashkin and E. I. Yakubovich, Dokl. Akad. Nauk SSSR **276**, 76 (1984) [Sov. Phys. Dokl. **29**, 370 (1984)].
6. V. K. Andreev, O. V. Kaptsov, V. V. Pukhnachev, *et al.*, *Application of Group-Theoretical Methods in Hydrodynamics* (Nauka, Novosibirsk, 1994).
7. A. A. Abrashkin, D. A. Zen'kovich, and E. I. Yakubovich, Dokl. Akad. Nauk **357**, 619 (1997) [Phys. Dokl. **42**, 111 (1997)].
8. S. M. Belotserkovskiĭ and A. S. Ginevskiĭ, *Modeling of Turbulent Jets and Wakes on the Basis of the Method of Discrete Vortices* (Fizmatlit, Moscow, 1995).
9. T. Sarpkaĭya, Sovr. Mashinostr., Ser. A, No. 10, 1 (1989).
10. P. G. Saffman, *Vortex Dynamics* (Univ. of Cambridge Press, Cambridge, 1992).
11. G. Ya. Dynnikova, Izv. Ross. Akad. Nauk, Mekh. Zhidk. Gaza, No. 5, 11 (2003).
12. Y. Ogami and T. Akamatsu, Comput. Fluids **19** (3/4), 433 (1991).
13. G. Ya. Dynnikova, *Proc. 11th Int. Symposium on Methods of Discrete Singularities in Problems of Mathematical Physics. Abstracts of Papers* (Kharkov–Kherson, 2003), p. 103.
14. M. Van-Dyke, *An Album of Fluid Motion* (Parabolic, Stanford, 1982).
15. H. Persillon and M. Braza, J. Fluid Mech. **365**, 23 (1998).

Translated by Yu. Verevochkin

Doklady Physics, Vol. 49, No. 11, 2004, pp. 653–657. Translated from Doklady Akademii Nauk, Vol. 399, No. 1, 2004, pp. 47–51.

MECHANICS

Formulation and Solution of the Problem of Bow Dynamics

A. V. Zvyagin and A. A. Malashin

Presented by Academician E.A. Shemyakin April 5, 2004

Received May 5, 2004

INTRODUCTION

In formulation of the problem of shooting from a sports bow, the basic and most complicated stage is the analysis of the arrow acceleration process in which the arrow is set in motion by the force of bowstring tension and is accelerated until departing from the bow (take off from the string). The arrow departure velocity depends on the string tension force, on the material and shape (geometry) of the staff, on the angle of the string deviation when the bow is stretched for shooting, and on the method of string fixing.

In this study, equations for both the bow-staff dynamics and bowstring dynamics are obtained. In the case of large initial staff displacements and large string-deviation angles, we are dealing with a complicated nonlinear problem. In this connection, methods of simplifying the problem are analyzed. Solutions are obtained that can be a test characteristic for numerical calculations in both the nonlinear case and the case of complicated bow geometry.

We study features of tension as a function of geometry and physical problem parameters in the nonlinear formulation and for the case of large displacements and bends. It is found that, for small angles of the string deviation from the equilibrium state, the string tension weakly depends on the deviation angle, and the tension for the speed-up time can be considered as constant. For a usual bow, the arrow departure velocity lies within the range 50–60 m s^{-1}.The propagation velocity of transverse waves in the string (~300–400 m s^{-1}) turns out to be much higher than the arrow velocity of motion (especially in the accelerated onset). As is shown in this paper, 20–40 transverse-wave reflections occur in the segment ranging from the arrow–string contact point to the string fixing point. In the case of strong tension, the string deviations are small in this segment. Thus, in the first approximation, we can consider it as a flexible nonstretchable line. This allows us to analyze string motion as a quasi-static process.

Moscow State Timber University,
ul. Lenina 4/17, Khot'kovo, Moscow oblast, Russia
e-mail: malashin@mgul.ac.ru

For certain bow shapes and features of string tension, it is possible to perform analysis and find the solution to the problem in its linear formulation.

EQUATIONS OF MOTION FOR A BOW STAFF AND STRING

We represent the staff as a flexible homogeneous rod that is rectilinear in its nondeformed state. This make it possible to simulate the position of the staff using its middle fiber [1].

We introduce the following basic characteristics of the rod: S is the Lagrangian coordinate; D is the cross-section area; E and G are the Young's modulus and shear modulus, respectively; ρ_b is the density; $\rho = \rho_b D$ is the rod linear density; $\mathbf{Q}$ and $\mathbf{M}$ are, respectively, the vectors of forces and moments acting onto the cross-section area; $\mathbf{V}$ and $\mathbf{W}$ are the vectors of the velocity and acceleration; $\boldsymbol{\psi}$ is the vector of the angular acceleration for the rotation of the given cross section; J_b is the rotation moment for an element with respect to an instantaneous rotation axis; $\boldsymbol{\omega}$ is the angular velocity of a cross section; $\mathbf{q}$ and $\boldsymbol{\mu}$ are the linear densities of external forces and moments; $\mathbf{R}_0$ and $\mathbf{R}$ are the initial and current radii vectores of the middle fiber; and, finally, $\boldsymbol{\tau}$, $\mathbf{n}$, and $\boldsymbol{\beta}$ are unit vectors of the tangent, normal, and binormal to the middle fiber.

Analyzing the equilibrium of forces and moments acting on a separated rod element of length dS, we obtain the equations of motion for the rod in the form

$$\rho\mathbf{W} = \frac{\partial\mathbf{Q}}{\partial S} + \mathbf{q}, \quad J_b\boldsymbol{\psi} = \frac{\partial\overline{M}}{\partial S} + \boldsymbol{\tau}\times\mathbf{Q} + \boldsymbol{\mu}. \qquad (1)$$

Equations (1) are complemented by the kinematic equation

$$\frac{\partial^2\mathbf{R}}{\partial S\partial t} = \frac{\partial^2\mathbf{R}}{\partial t\partial S} \qquad (2)$$

and by equations of the elastic bond of the moments with the variation of the curvature and rotation of the middle fiber,

$$M_\beta = EJ_\beta(\chi_\beta - \chi_{\beta 0}), \quad M_n = EJ_n(\chi_n - \chi_{n0}), \quad M_\tau = GJ_\tau(\chi_\tau - \chi_{\tau 0}). \qquad (3)$$

1028-3358/04/4911-0653$26.00

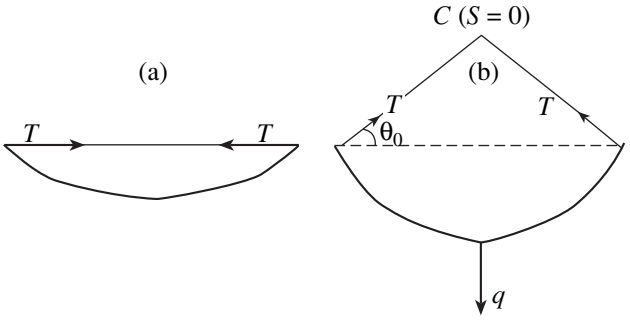

Fig. 1. (a) Stretched bow and (b) bow at the instant of shooting. T and q are the string tension and the force acting on the bow staff during a shot.

Here, χ_n and χ_β are the fiber-curvature projections onto the plane orthogonal to the main normal and binormal. χ_τ is the fiber torsion (χ_{n0} and $\chi_{\beta 0}$ correspond to the not deformed state). In the case of a nonstretchable rod, we have

$$Q_\tau = E\varepsilon. \tag{4}$$

We consider the staff to be nonstretchable ($\varepsilon = 0$) and motion to occur in the *xy* plane. We now introduce the angle θ of the middle-fiber inclination with respect to the *ox* axis. Furthermore, we project the equations onto the mobile axes $\boldsymbol{\tau} = (\cos\theta, \sin\theta)$, $\mathbf{n} = (-\sin\theta, \cos\theta)$. We also write out the decompositions of the velocity vectors and internal-force vectors in the form

$$\mathbf{V} = u\boldsymbol{\tau} + v\mathbf{n}, \quad \mathbf{Q} = T\boldsymbol{\tau} + N\mathbf{n}.$$

The equation can be written as

$$\rho(\dot{u} - v\dot{\theta}) = T' - N\theta' + q_\tau, \quad M = EJ\theta';$$

$$\rho(\dot{v} + u\dot{\theta}) = N' + T\theta' + q_n, \quad u' - v\theta' = 0; \tag{5}$$

$$\rho\frac{J}{F}\ddot{\theta} = M' + N + \mu, \quad v' + u\theta' = \dot{\theta}.$$

Here, dots and primes correspond to the derivatives with respect to time and to the S coordinate, respectively.

Further, we represent the bow string as a perfect nonstretchable line. The equations for this line are similar to Eqs. (5) [2], in which only the projection of the force onto the tangent to the line is nonzero, whereas all other internal forces and moments vanish. Let ρ_0 be the string linear density. T is tension, and φ is the tangent inclination angle to the *ox* axis. Under these assumptions, we arrive at the following equations:

$$\rho_0(\dot{U} - V\dot{\varphi}) = T', \quad U' - V\varphi' = 0;$$
$$\rho_0(\dot{V} + U\dot{\varphi}) = T\varphi', \quad V' + U\varphi' = \dot{\varphi}, \tag{6}$$

where $\bar{V} = U\bar{\tau} + V\bar{n}$ is the line velocity.

FORMULATION OF THE PROBLEM

Let $2L$ and $2I$ are the lengths of the staff and string; θ_0 is the string deviation angle at the shot instant (Fig. 1b). Formulation of the initial conditions of the given problem requires preliminarily solving the problem on the rod equilibrium under string tension forces acting from the source side of a hand holding the bow. We model this force as a concentrated one applied in the middle of the staff. The point C is the interaction (contact) point of the string and the arrow of mass m. The equation of motion for the arrow plays the role of the boundary condition for the string at the point $s = 0$, i.e.,

$$m\dot{V}_y(0, t) = -2T(0, t)\sin\theta(0, t)$$

with the initial conditions

$$V_y(0, 0) = 0, \quad T(0, 0) = T_0, \quad \theta(0, 0) = \theta_0.$$

At the boundaries $s = \pm l$, the line velocity coincides with that of the rod ends.

For the rod ends $S = \pm L$, the force $\mathbf{T}$ is specified, whereas the moment M must be zero. The concentrated force $q(t) = 2T(l, t)\sin\theta(l, t)$ is also determined in the course of solving the problem from the condition that the velocity of the rod point $S = 0$ is zero. Let the *ox* axis be parallel to the bow string (Fig, 1a) and the *oy* axis be the symmetry axis of the problem. The origin of the coordinate axis, we make coincident with the immobile bow-staff point, i.e., the force-application point. We now determine the torsion force at the shot instant as a function of the angle θ_0. We solve the problem of staff equilibrium under the action of the forces $\mathbf{T}$ and $\mathbf{q}$.

Initially, we consider the problem of the determination of tension in the absence of force ($q = 0$) (Fig. 1a). In conditions of static equilibrium, Eqs. (5) take the form

$$T'(S) - N(S)\theta'(S) = 0, \quad M'(S) + N = 0,$$
$$N'(S) + T(S)\theta'(S) = 0, \quad M(S) + EJ\theta'(S). \tag{7}$$

The boundary conditions are

$$S = 0, \quad x = 0, \quad \theta = 0, \quad N = 0;$$

$$S = L, \quad x = l, \quad \mathbf{T} = -T_0(\bar{\tau}\cos\theta + \bar{n}\sin\theta), \quad M = 0.$$

We now introduce the dimensionless variables

$$s^* = \frac{S}{L}, \quad T^* = \frac{T}{T_0}, \quad N^* = \frac{N}{T_0},$$
$$k^2 = \frac{EJ}{T_0L^2}, \quad M^* = \frac{M}{LT_0}, \quad l_0 = \frac{l}{L}. \tag{8}$$

To simplify the written form of the variables in (8), we below omit the asterisks. Thus, the last equation in (7) can be represented as

$$M(s) = k^2\theta'(s). \tag{9}$$

The first two equations are being integrated and, with regard to the boundary conditions for $s = 0$, we obtain the following expressions for the forces:

$$T = -\cos\varphi, \quad N = \sin\varphi, \quad \varphi = \theta. \tag{10}$$

After multiplying by θ', the equation for the determination of the staff shape $k^2\theta''(s) = -\sin\theta(s)$ is solved and yields

$$\frac{k^2}{2}(\theta')^2 = \cos\theta + \text{const} = \cos\theta - \cos\theta_1. \tag{11}$$

The integration constant in (11) is defined by the condition that, at the point $s = 0$, the moment is zero, the angle at this point being denoted as θ_1. Thus, the determination of the bow shape is reduced to finding the integral

$$\frac{\sqrt{2}s}{k} = \int_0^\theta \frac{d\theta}{\sqrt{\cos\theta - \cos\theta_1}}. \tag{12}$$

In expression (12), the quantity θ_1 is unknown and is determined by the string length. At

$$\frac{dx}{ds} = \cos\theta, \quad \frac{dx}{d\theta} = \frac{ds}{d\theta}\cos\theta = \frac{k}{\sqrt{2}}\frac{\cos\theta}{\sqrt{\cos\theta - \cos\theta_1}}$$

we find

$$\frac{\sqrt{2}x}{k} = \int_0^\theta \frac{\cos\theta d\theta}{\sqrt{\cos\theta - \cos\theta_1}}. \tag{13}$$

Thus, the determination of the staff shape for the stretched bow is reduced to integrals (12) and (13). As a result, we arrive at two equations with two unknowns θ_1 and k:

$$\begin{aligned}\frac{\sqrt{2}}{k} &= \int_0^{\theta_1} \frac{d\theta}{\sqrt{\cos\theta - \cos\theta_1}},\\ \frac{\sqrt{2}l_0}{k} &= \int_0^{\theta_1} \frac{\cos\theta d\theta}{\sqrt{\cos\theta - \cos\theta_1}}.\end{aligned} \tag{14}$$

In addition, we introduce the elliptic integrals of the first and second kinds, namely, $F(\varphi, \lambda)$ and $E(\varphi, \lambda)$ [5]. Then, Eqs. (12), (13) take the form

$$\frac{\sqrt{2}s}{k} = \sqrt{2}F\left(\varphi, \sin\frac{\theta_1}{2}\right),$$

$$\frac{\sqrt{2}x}{k} = \sqrt{2}\left[2E\left(\varphi, \sin\frac{\theta_1}{2}\right) - F\left(\varphi, \sin\frac{\theta_1}{2}\right)\right],$$

$$\varphi = \arcsin\frac{\sin\frac{\theta}{2}}{\sin\frac{\theta_1}{2}}.$$

Equations (14) are expressed in terms of complete elliptic integrals

$$\begin{aligned}\frac{\sqrt{2}}{k} &= \sqrt{2}F\left(\frac{\pi}{2}, \sin\frac{\theta_1}{2}\right),\\ \frac{\sqrt{2}l_0}{k} &= \sqrt{2}\left[2E\left(\frac{\pi}{2}, \sin\frac{\theta_1}{2}\right) - F\left(\frac{\pi}{2}, \sin\frac{\theta_1}{2}\right)\right].\end{aligned} \tag{15}$$

This makes it possible to reduce the determination of the angle θ_1 to solving the following algebraic equation with respect to $\lambda = \sin\frac{\theta_1}{2}$:

$$2E\left(\frac{\pi}{2}, \lambda\right) = (1 + l_0)F\left(\frac{\pi}{2}, \lambda\right), \tag{16}$$

after which the quantity

$$\frac{1}{k} = \sqrt{\frac{T_0L^2}{EJ}} = F\left(\frac{\pi}{2}, \lambda\right) \tag{17}$$

is determined. Retaining terms up to λ^4 in the asymptotic expressions for the complete elliptic integrals, we reduce problem (17) to solving the biquadratic equation

$$\lambda^4 + \frac{16(3 + l_0)}{15 + 9l_0}\lambda^2 - \frac{64(1 - l_0)}{15 + 9l_0} = 0.$$

The root of the equation exists for arbitrary l_0 within the interval $0 < l_0 < 1$:

$$\lambda = \sin\frac{\theta_1}{2} = 2\sqrt{2}\sqrt{\frac{\sqrt{24 - 8l_0^2} - 3 - l_0}{15 + 9l_0}}.$$

We can approximate the dependence λ^2 by the linear function

$$\lambda^2 = 1 - l_0 = \sin^2\frac{\theta_1}{2} = \frac{1}{2}(1 - \cos\theta_1),$$

whence it follows that

$$\theta_1 = \arccos(2l_0 - 1). \tag{18}$$

In this case, the dependence of tension on l_0 is determined by the analytical expression

$$\frac{T_0L^2}{EJ} = \frac{\pi}{2}(1 + 0.25(1 - l_0) + 0.140625(1 - l_0)^2). \tag{19}$$

The solution to the problem of determining the bow tension at the shot instant (Fig. 1b) is obtained by a similar manner. Here, the force q is present and must be balanced by the normal force N at the point $s = 0$. The expression for the forces is of the form

$$\begin{aligned}T = -\cos(\theta + \theta_0), \quad N = \sin(\theta + \theta_0),\\ x_1 = l_0\cos\theta_0.\end{aligned} \tag{20}$$

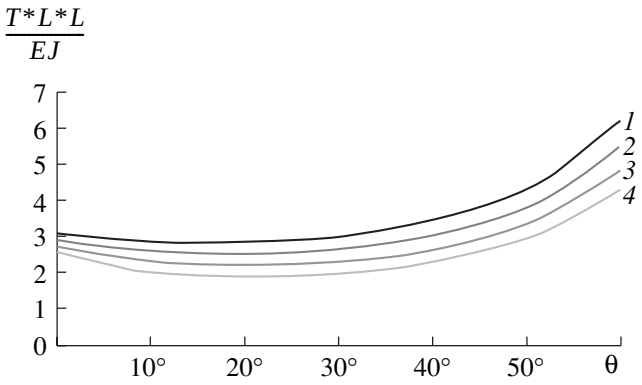

Fig. 2. String tension as a function of the string-deviation angle θ at the instant of shooting: (*1*) $\frac{I}{L}$ = 0.6, (*2*) 0.7, (*3*) 0.8, (*4*) 0.9.

As in the case considered before, the line shape is determined by integrals of the types (12) and (13):

$$\frac{\sqrt{2}}{k} = \int_0^{\varphi_1} \frac{d\varphi}{\sqrt{\cos\varphi - \cos\varphi_1}} - \int_0^{\theta_0} \frac{d\varphi}{\sqrt{\cos\varphi - \cos\varphi_1}},$$

$$\varphi_1 = \theta_0 + \theta_1;$$

$$\frac{\sqrt{2}l_0\cos\theta_0}{k}$$

$$= \int_0^{\varphi_1} \frac{\cos(\varphi - \theta_0)d\varphi}{\sqrt{\cos\varphi - \cos\varphi_1}} - \int_0^{\theta_0} \frac{\cos(\varphi - \theta_0)d\varphi}{\sqrt{\cos\varphi - \cos\varphi_1}}.$$

As a result, we arrive at the algebraic equations for the determination of T_0 and θ_1:

$$\frac{1}{k} = F\left(\frac{\pi}{2}, \sin\frac{\theta_0 + \theta_1}{2}\right) - F\left(\varphi_1, \sin\frac{\theta_0 + \theta_1}{2}\right),$$

$$\varphi_1 = \arcsin\sqrt{\frac{1 - \cos\theta_0}{1 - \cos(\theta_0 + \theta_1)}},$$

$$\frac{\sqrt{2}l_0\cos\theta_0}{k} = \sqrt{2}\cos\theta_0\left[2\left(E\left(\frac{\pi}{2}, \sin\frac{\theta_0 + \theta_1}{2}\right)\right.\right.$$
$$\left.\left. - 2E\left(\varphi_1, \sin\frac{\theta_0 + \theta_1}{2}\right)\right)\right] \quad (21)$$

$$- \sqrt{2}\cos\theta_0\left[F\left(\frac{\pi}{2}, \sin\frac{\theta_0 + \theta_1}{2}\right) - F\left(\varphi_1, \sin\frac{\theta_0 + \theta_1}{2}\right)\right]$$

$$+ 2\sin\theta_0\sqrt{\cos\theta_0 - \cos(\theta_0 + \theta_1)}.$$

The solution to Eqs. (21) allows us to find (for a given string-deviation angle θ_0) the values of tension and of the angle θ_1 realized at the staff end. This presents an opportunity to determine the staff shape at the initial instant of time, i.e., to complete the formulation of boundary and initial values in the problem of shooting from a bow. The calculation results for tension as a function of the string-deviation angle are shown in Fig. 2. Analysis of these results testifies to the fact that tension weakly decreases with increasing string-deviation angles to 20° and, then, begins to rapidly increase.

SOLVING THE PROBLEM OF BOW DYNAMICS IN THE LINEAR FORMULATION

For certain bow types (admitting a string deviation of not more than 20°, tension is constant and equals 40–50 kg), the dynamic problem can be solved in the linear approximation. In this case, the equation of staff motion can be written in the form of the equation for compressed-beam dynamics [3, 4]:

$$\frac{\partial^2}{\partial s^2}\left(EI\frac{\partial^2 y}{\partial s^2}\right) + T_l\frac{\partial^2 y}{\partial s^2} = \rho D\frac{\partial^2 y}{\partial t^2}.$$

The set of dynamics equations for the bow staff and string is written as

$$a^2\frac{\partial^4 y}{\partial s^4} + k^2\frac{\partial^2 y}{\partial s^2} = \frac{\partial^2 y}{\partial t^2},$$

$$y(s = \pm L) = Y(S = \pm l),$$

$$\frac{\partial^3 y}{\partial s^3}(s = \pm L, t) = F_\pm(t) = \frac{T}{EI}\frac{\partial Y}{\partial S}(S = \pm l, t), \quad (22)$$

$$y(s, 0) = y_0(s),$$

$$\frac{\partial y}{\partial t}(s, 0) = 0;$$

$$b^2\frac{\partial^2 Y}{\partial S^2} = \frac{\partial^2 Y}{\partial t^2},$$

$$Y(S = \pm l) = y(S = \pm L),$$

$$Y(S, 0) = Y_0(S), \quad (23)$$

$$\frac{\partial Y}{\partial t}(S, 0) = 0,$$

$$m\frac{\partial^2 Y(0, t)}{\partial t^2} = 2T\frac{\partial Y(0, t)}{\partial S}.$$

Here, $y(s, t)$ and $Y(S, t)$ are the transverse displacements of the staff and string, $a^2 = \frac{EI}{\rho D}$, and $k^2 = \frac{T}{\rho D}$.

The solution to the set of equations (23) is sought using the method of characteristics. Since, at the instant of time prior to the first reflected wave has arrived, the relations

$$b\frac{\partial Y}{\partial S}(0,t) = b\frac{\partial Y}{\partial S}(S,0) - \frac{\partial Y}{\partial t}(0,t), \quad \theta_0 = \frac{\partial Y(S,0)}{\partial S},$$

are valid, the last equation in the set of Eqs. (23) takes the form

$$m\frac{\partial V}{\partial t} = 2T\left(\frac{\partial Y(S,0)}{\partial s} - \frac{V}{b}\right),$$

where V is the string velocity at the point of contacting the arrow. The arrow velocity before the first transverse wave has arrived is

$$V_0(t) = b\theta_0(1 - \exp(-2Tt/mb)).$$

At the instant $\tau = \frac{2l}{b}$ of the arrival of the reflected wave, the angle of string deviation at the arrow contact point changes abruptly. The relation between the velocities and deformations before and after the arrival of the next transverse wave,

$$\frac{\partial Y(0,t)}{\partial S} = \frac{\partial Y(0,t-2\tau)}{\partial S} - \frac{V(t-2\tau)}{b} - \frac{V(t)}{b}$$

makes it possible to construct recurrence differential equations for the determination of the arrow velocity at each stage in terms of the velocity at the preceding stage. For example, immediately after the arrival of the first reflected wave, we have

$$m\frac{\partial V_1(t)}{\partial t} = 2T\left(\theta_0 - \frac{V_1(t)}{b} - \frac{V_0(t-2\tau)}{b}\right).$$

Here, V_1 is the velocity of the arrow and of the string prior to the arrival of the second reflected wave.

With the initial conditions taken into account, the solution to this equation is

$$V_1(t) = b\theta_0 e^{-\lambda t}[(1 + \lambda t - \lambda\tau)2e^{\lambda\tau} - 1] - b\theta_0,$$

$$\lambda = \frac{2T}{mb}.$$

The dependence

$$\frac{\partial Y(l,t)}{\partial S} = \frac{\partial Y(0,t-\tau)}{\partial S} - \frac{V(t-\tau)}{b}$$

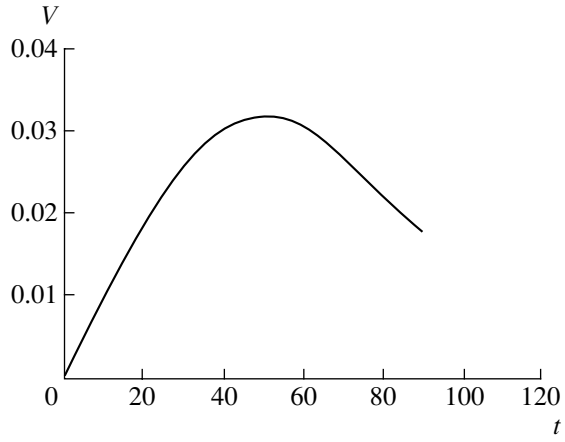

Fig. 3. Time dependence of the arrow velocity V (k = 0.0001).

makes it possible to find the string deviation angles at fixation points and to determine the force $F_{\pm}(t)$ acting on the staff from the string. Thereby, we additionally define the set of Eqs. (22) to which the solution is sought by, e.g., the method of separation of variables.

The calculation results obtained in the linear approximation for the time dependence of the arrow velocity at the speed-up period are presented in Fig. 3.

ACKNOWLEDGMENTS

The work was supported by the Russian Foundation for Basic Research, project no. 03-01-00131.

REFERENCES

1. V. A. Svetlitskiĭ, *Mechanics of Rods* (Vysshaya Shkola, Moscow, 1987), Vol. 1.
2. Kh. A. Rakhmatulin and Yu. A. Dem'yanov, *Strength under Intense Short-Time Loads* (Fizmatgiz, Moscow, 1961).
3. Yu. N. Rabotnov, *Mechanics of a Deformed Solid* (Nauka, Moscow, 1988).
4. A. I. Vesnitskiĭ, *Waves in Systems with Moving Boundaries and Loads* (Fizmatlit, Moscow, 2001).
5. I. S. Gradshteĭn and I. M. Ryzhik, *Tables of Integrals, Sums, Series, and Products* (Fizmatgiz, Moscow, 1962; Academic Press, New York, 1980).

Translated by G. Merzon

Doklady Physics, Vol. 49, No. 11, 2004, pp. 658–661. Translated from Doklady Akademii Nauk, Vol. 399, No. 1, 2004, pp. 52–55.

MECHANICS

Stability, Resonances, and Instability of Regular Vortex Polygons in a Circular Domain

L. G. Kurakin

Presented by Academician G.G. Chernyĭ April 21, 2004

Received April 29, 2004

INTRODUCTION

In recent years, the model of point vortices has demonstrated its fundamental importance in studies of vortices in liquid helium and electron columns in plasma physics. The results obtained are stimulating new applications and additional studies of the model in different fields of research (experiment, theory, and numerical simulations) [1–3]. This has already led to the solution of several old problems. Recently, the efforts of many researchers were completed in a mathematically rigorous solution of the Kelvin problem (formulated in 1878) on the stability of steady-state rotation in a system of n identical point vortices located in a plane at apexes of a regular n-gon [4, 5]: the rotation is stable only if $n \le 7$, whereas, at $n \ge 8$, this motion is unstable. In the case of $n \ne 7$, linear analysis turns out to be sufficient to arrive at a conclusion concerning nonlinear stability. At the same time, for $n = 7$, it is necessary to involve nonlinear terms in the analysis.

The Kelvin problem, generalized for the spherical case, was also solved in its exact nonlinear formulation (see [6–9] and also review article [3, pp. 17–178]). It was proved that the curvature is not able to stabilize a vortex polygon, and, in particular, it makes a heptagon unstable.

The present paper deals with the Kelvin problem for the case in which the vortex n-gon of radius R_0 is located within circular domain R with a common center of symmetry. Havelock [11] was the first to study this problem using mathematical methods in the linear formulation. As was shown in [11], the corresponding linearized system has exponentially growing solutions at $n \ge 7$ and also in cases ($2 \le n \le 6$) in which the parameter $p = \dfrac{R_0^2}{R^2}$ exceeds a certain critical value, $p_{*n} < p < 1$. In all other cases, the linear system exhibits only a power-law instability, which is usual—and inevitable—for systems of such a kind.

Rostov State University,
ul. Zorge 5, Rostov-on-Don, 344090 Russia

According to the well-known Lyapunov theorem, the equilibrium of a complete system is unstable when a linearized system is exponentially unstable. The power-law instability is insufficient to draw this conclusion; therefore, nonlinear terms should be involved in the analysis.

The substantiation of all the conditions for nonlinear stability on a plane and sphere in the Kelvin problem is based on the fact that, in the trajectory of steady-state motion for the vortex n-gon, the relative Hamiltonian (see, for example, [4, 5]) attains its maximum value. In this case, the stability of steady-state motion is treated as stability in the Routh sense.

In the present paper, such an approach allows us to prove the stability of steady-state rotation of the regular vortex n-gon within a circle. The proof is obtained in the exact nonlinear formulation of the problem in the cases (a) $0 < p \le p_{*n}$ for even n ($n = 2, 4, 6$), (b) $0 < p < p_{03}$ for three vortices, and (c) $0 < p \le p_{05}$ when $n = 5$. The values of p_{0k} and p_{*n} are specified in Table 1.

The numerical analysis performed in [10] revealed the alternating-sign behavior of the relative Hamiltonian under conditions (d) $n = 3$, $p_{03} < p < p_{*3}$ or (e) $n = 5$, $p_{05} < p < p_{*5}$, although, in these cases, the lin-

Table 1. Critical values p_{*n} and p_{0n}, which are the roots of the polynomials P_n and Q_n, respectively

$P_2 = 7p^3 - 3p^2 + 5p - 1$	$p_{*2} \approx 0.2137403629$
$P_3 = 10p^6 + 3p^5 + 6p^4 + 10p^3 + 6p^2 + 3p - 2$	$p_{*3} \approx 0.3212811546$
$Q_3 = 5p^6 + 9p^5 + 5p^3 + 9p^2 - 1$	$p_{03} \approx 0.3040641646$
$P_4 = 7p^6 + p^4 + 9p^2 - 1$	$p_{*4} \approx 0.3298399891$
$P_5 = 18p^{10} + 10p^8 + 15p^7 + 34p^5 + 15p^3 + 10p^2 - 2$	$p_{*5} \approx 0.3461008645$
$Q_5 = 27p^{12} + 81p^{11} + 132p^{10} + 135p^9 + 90p^8 + 96p^7 + 153p^6 + 196p^5 + 165p^4 + 60p^3 + 2p^2 - 9p - 3$	$p_{05} \approx 0.3410383818$
$P_6(x) = 23p^9 + 13p^6 + 37p^3 - 1$	$p_{*6} \approx 0.2991212951$

1028-3358/04/4911-0658$26.00

earized system is characterized only by the power-law instability. Such a situation is analyzed below using the methods of the Kolmogorov–Arnold–Mozer theory. In addition, we list and analyze all resonances up to the fourth-order ones available in the system. This analysis is based on the results of Markeev and Sokol'skiĭ (see [12]). It turned out that two of these resonances led to instability: (f) $n = 3$, $p = p_{03}$ and (g) $n = 5$, $p = p_{*05} \approx 0.3443792197$.

As a result, we present in this paper both the necessary and sufficient conditions for the stability and instability of a regular n-gon of point vortices ($n \neq 5$) located within a circle. For a vortex pentagon, the answer to the question concerning the instability has remained unclear for the null set when the parameter p meets conditions $p \in [a, b] \subset (p_{05}, p_{*5})$ and there exist resonances higher than four ($a \approx 0.3412172781$ and $b \approx 0.3429140261$).

EQUATIONS OF MOTION

The basic results on the motion of point vortices inside and outside the circular domain were systematized by Kilin *et al.* [3, pp. 414–440].

Motion of the system of n point vortices at the plane inside a circle of radius R is described by the equations

$$\dot{z}_k^* = \frac{1}{2\pi i}\sum_{j=1}^{n}{}' \frac{\kappa_j}{z_k - z_j} - \frac{1}{2\pi i}\sum_{j=1}^{n}\frac{\kappa_j}{z_k - \hat{z}_j}, \quad k = 1, 2, \ldots, n. \tag{1}$$

Here, $z_k = x_k + iy_k$, $k = 1, 2, \ldots, n$ are complex variables; x_k, y_k are the Cartesian coordinates of the kth vortex; κ_k is its intensity; and $\hat{z}_k = \dfrac{R^2}{z_k^*}$ is the reflection of the kth vortex from the circle boundary. The prime denotes the omission of the term with $j = k$, and the asterisk implies complex conjugation. The phase space Z for the set of Eqs. (1) is $(\mathbb{C}\backslash\{0\})^n$ with cuts along all the hyperplanes $z_j = z_k$, $j \neq k$.

The set of Eqs. (1) is the Hamiltonian set characterized by the Hamiltonian

$$H = -\frac{1}{4\pi}\sum_{1 \le j < k \le n}\kappa_j\kappa_k \ln[(z_j - z_k)(z_j^* - z_k^*)] + \frac{1}{8\pi}\sum_{j=1}^{n}\sum_{k=1}^{n}\kappa_j\kappa_k \ln[(R^2 - z_j z_k^*)(R^2 - z_j^* z_k)]. \tag{2}$$

It has two integrals: energy H and the total moment of inertia,

$$M = \sum_{k=1}^{n}\kappa_k |z_k|^2. \tag{3}$$

This set is invariant with respect to the group G, with the group generators being the mirror reflection j: $z \mapsto z^*$ and rotation g^{rot}: $z \mapsto e^{i\alpha} z$, $\alpha \in \mathbb{R}$. The action $g \mapsto L_g$ of the group G on the phase space Z is determined by the relationship $L_g z = (gz_1, gz_2, \ldots, gz_n)$ for an arbitrary point $z = (z_1, z_2, \ldots, z_n) \in Z$ and arbitrary motion $g \in G$.

It is worth recalling that the motion is referred to as steady-state motion if it is generated by transformations corresponding to a certain one-parameter subgroup of the symmetry group characterizing the equation under study.

We seek the steady-state motion corresponding to the subgroup of rotations g^{rot} in the form $z_k = e^{i\omega t}u_k$. Then, the equation determining the steady-state motions is written as the following set of equations:

$$-i\omega u_k^* = \frac{1}{2\pi i}\sum_{j=1}^{n}{}' \frac{\kappa_j}{u_k - u_j} - \frac{1}{2\pi i}\sum_{j=1}^{n}\frac{\kappa_j}{u_k - \hat{u}_j}, \quad k = 1, 2, \ldots, n, \tag{4}$$

with respect to the unknowns $u_1, u_2, \ldots, u_n \in \mathbb{C}$ and $\omega \in \mathbb{R}$.

In the case of equal intensities $\kappa_1 = \kappa_2 = \ldots = \kappa_n = \kappa$, the exact solution to the set under consideration is well known:

$$u_k = R_0 e^{2\pi i(k-1)/n}, \quad k = 1, 2, \ldots, n, \tag{5}$$

$$\omega = \frac{\kappa}{4\pi R_0^2}\left(\frac{n+1}{2} - \frac{n}{1 - p^n}\right), \tag{6}$$

where we have introduced the notation $p = \dfrac{R_0^2}{R^2}$ and R_0 meets the inequality $0 < R_0 < R$.

The corresponding steady-state mode is determined by the relationships

$$z_k(t) = R_0 e^{i\omega t}u_k, \quad k = 1, 2, \ldots, n. \tag{7}$$

Thus, the configuration of identical vortices located at the circumference of radius R_0 at the apexes of a regular n-gon rotates at a constant angular velocity $\omega = \omega(p)$.

THE STABILITY OF A REGULAR VORTEX n-GON

We now assume all vortices to have the same intensity κ and analyze the stability of stead-state solution (7). For convenience of calculation, we consider that $R_0 = 1$.

The change of variables

$$z_k(t) = e^{i\omega t}v_k(t)$$

in set (1) results in the following equation describing the relative motion:

$$\dot{v}_k^* = \frac{1}{2\pi i}\sum_{j=1}^{n}{}' \frac{\kappa}{v_k - v_j} - \frac{1}{2\pi i}\sum_{j=1}^{n}\frac{\kappa}{v_k - \hat{v}_j} + i\omega v_k^*, \quad k = 1, 2, \ldots, n, \tag{8}$$

with the relative Hamiltonian

$$E(v) = H(v) + \omega M(v), \quad M = \kappa\sum_{k=1}^{n}|v_k|^2, \tag{9}$$

where $v = (v_1, v_2, \ldots, v_n) \in C^n$.

In each plane of variables v_k, we introduce new coordinates and write v_k in the form

$$v_k = \sqrt{2\left(\frac{R_0^2}{2} + r_k\right)}e^{i\left(\frac{2\pi}{n}(k-1) + \theta_k\right)}. \tag{10}$$

In variables $r = (r_1, r_2, \ldots, r_n)$ and $\theta = (\theta_1, \theta_2, \ldots, \theta_n)$, Eq. (8) takes the form

$$\dot{r}_k = \frac{\partial E}{\partial \theta_k}(v(r, \theta)), \tag{11}$$

$$\dot{\theta}_k = -\frac{\partial E}{\partial r_k}(v(r, \theta)). \tag{12}$$

Steady-state motion (7) is put in correspondence with the continuous family of equilibrium states of the set of Eqs. (11), (12) located in the straight line $\Gamma = \{(r, \theta) \in R^{2n}: r = 0, \theta_1 = \theta_2 = \ldots = \theta_n\}$.

The expansion of function $E(v(\rho))$, $\rho \stackrel{\text{def}}{=} (r, \theta)$ into the Taylor series has the same form in the neighborhood of each equilibrium state belonging to family Γ:

$$E(v(\rho)) = \frac{\kappa^2}{4\pi}(E_0 + E_2(v(\rho)) + E_3(v(\rho)) + E_4(v(\rho)) + \ldots). \tag{13}$$

Here, dots denote terms of the power higher than four. The quadratic form E_2 can be represented as

$$E_2 = (S\rho, \rho), \quad S = \begin{pmatrix} F_1 & \frac{1}{2}G_0 \\ -\frac{1}{2}G_0 & F_2 \end{pmatrix}, \quad \rho = (r, \theta), \tag{14}$$

and the linearization matrix for the set of Eqs. (11), (12) has the following form for the zeroth equilibrium state:

$$L = \begin{pmatrix} G_0 & 2F_2 \\ -2F_1 & -G_0 \end{pmatrix}. \tag{15}$$

Here, F_1 and F_2 are symmetric matrices and G_0 is a skew-symmetric matrix. Their matrix elements and eigenvalues λ_{1k}, λ_{2k}, and $i\lambda_{0k}$, $k = 1, 2, \ldots, n$, were written out by Havelock in [11]:

$$\lambda_{1k} = -\frac{1}{2}k(n-k) - (n+1) - \frac{n^2 p^{n-k}(1+p^k)^2}{2(1-p^n)^2} - \frac{nk(p^k - p^{n-k})}{2(1-p^n)} + \frac{2n}{1-p^n}, \tag{16}$$

$$\lambda_{2k} = \frac{1}{2}k(n-k) - \frac{nk(p^k - p^{n-k})}{2(1-p^n)} - \frac{n^2 p^{n-k}(1-p^k)^2}{2(1-p^n)^2}, \tag{17}$$

$$\lambda_{0k} = \frac{nk(p^k + p^{n-k})}{1-p^n} - \frac{n^2 p^{n-k}(1-p^{2k})}{(1-p^n)^2}. \tag{18}$$

The eigenvalues of matrix S can be found using the roots of the polynomials,

$$\Lambda^2 - (\lambda_{1k} + \lambda_{2k})\Lambda + \lambda_{1k}\lambda_{2k} - \frac{1}{4}(\lambda_{0k})^2, \quad k = 1, 2, \ldots, n.$$

For the linearization matrix L, the eigenvalues are determined by the formulas [11]

$$\sigma_k^{\pm} = -i\lambda_{0k} \pm 2\sqrt{-\lambda_{1k}\lambda_{2k}}, \quad k = 1, 2, \ldots, n.$$

The following theorem validates the linearization method in the stability problem for a vortex n-gon. The stability in the Routh sense for steady-state solution (7) implies the stability of family Γ of equilibrium states for Eq. (8) corresponding to the relative motion. The instability is understood here in the strongest sense: the invariant set of steady-state rotations is (transversally) unstable. The values of p_{0k} and p_{*n} are specified in Table 1.

Theorem 1. *Steady-state rotation* (7) *of the regular vortex n-gon is stable in the Routh sense in the cases*

(*1*) $0 < p < p_{*n}$ *and for even values of n* ($n = 2, 4, 6$),

(*2*) $0 < p < p_{03}$ *for* $n = 3$, *and*

(*3*) $0 < p < p_{05}$ *when* $n = 5$,

as well as at $n = 1$. *It is unstable when* $n \geq 7$ *or* $p_{*n} < p < 1$ *at an arbitrary* $n = 2$–6.

Table 2. Critical values of parameter p corresponding to resonances: p_{00} is the double diagonalizable zero and $p_{k:m}$ is the $k:m$ resonance; $\hat{p}$ denotes a nondiagonalizable case

$n = 2$	$\hat{p}_{00} = p_{*2}$
$n = 3$	$p_{00} = p_{03}$, $p_{1:3} \approx 0.3168967611$
	$p_{1:2} \approx 0.3193266263$, $\hat{p}_{1:1} = p_{*3}$
$n = 4$	$\hat{p}_{00} = p_{*4}$
$n = 5$	$p_{00} = p_{05}$
	$p_{1:3} \approx 0.3434991204$, $p_{1:3} \approx 0.3448097395$
	$p_{1:2} \approx 0.3443792197$, $p_{1:2} \approx 0.3455248914$
	$p_{1:1} \approx 0.3459139152$, $\hat{p}_{1:1} = p_{*5}$
$n = 6$	$\hat{p}_{00} = p_{*6}$

The proof repeats the substantiation of the validity of linearization in the problem of stability for a regular vortex n-gon in a plane (see Theorem 1 in [4, 5]).

The following theorem requires for its proof taking into account the nonlinear terms present in the system. Formal stability in the Routh sense implies that there exists a power series—possibly diverging—that is formally an integral of the equation with respect to relative motion (8). This integral attains the minimum value on the family Γ of equilibrium states for this motion. In the case of formal stability in the Routh sense, instability in the Lyapunov sense for family Γ (if it exists) does not manifest itself in the system even if, in the expansion, we take into account terms of an arbitrarily high (but finite) order. Below, we use the values $p_{0*5} \approx 0.3443792197$, $a \approx 0.3412172781$, $b \approx 0.3429140261$, and an arbitrary nonzero vector (n_1, n_2, n_3, n_4) with integer nonnegative components.

Theorem 2. *Steady-state rotation* (7) *of a regular vortex n-gon is stable in the Routh sense in the cases*

(*4*) $p = p_{*n}$ *at an arbitrary* $n = 2, 3, 4, 6$ *and also at* $p = p_{05}$ *for* $n = 5$;

(*5*) $p_{03} < p < p_{*3}$ *for* $n = 3$; *and*

$0 < p < p_{05}$ *when* $n = 5$,

or formally stable in the Routh sense if

(*6*) $n = 5$, $p \in (p_{05}, a) \cup (b, p_{0*5}) \cup (p_{0*5}, p_{*5}]$ *or if* $p \in [a, b]$ *under the conditions* $n_1\sigma_1^+ + n_3\sigma_3^+ + n_4\sigma_4^+ \neq n_2\sigma_2^-$.

It is unstable in the following resonance cases:

(*7*) $n = 3$, $p = p_{03}$,

(*8*) $n = 5$, $n = 5$, $p = p_{0*5}$.

Proof. First of all, owing to the existence of the cyclic variable, we reduce by one the number of degrees of freedom for the Hamiltonian system under study. Then, in the resonance cases listed in Table 2, we apply the appropriate theorems of Markeev and Sokol'skiĭ [12]. If the resonances are absent and inequalities (*5*) are met, stability is substantiated by verifying the validity of the conditions imposed by the Alnold–Mozer theorem [13, 14], while, in case (*6*), we use the theorems of Birkhoff, Glimm, and Brunot.

ACKNOWLEDGMENTS

The author is grateful to V.I. Yudovich for his attention to this study.

This work was supported by the Russian Foundation for Basic Research, project no. 02-01-00337, the Center for Basic Research in Natural Sciences at St. Petersburg State University (grant no. E02-1.0-145), and the Foundation of the President of the Russian Federation for Support of Leading Scientific Schools (grant no. NSh-1768.2003.1).

REFERENCES

1. P. K. Newton, *The n-vortex Problem: Analytical Techniques*: in *Appl. Math. Sci.* (Springer, New York, 2001), Vol. 145.
2. H. Aref, P. K. Newton, M. A. Stremler, *et al.*, Adv. Appl. Mech. **39**, 1 (2003).
3. *Basic and Applied Problems of Theory of Vortices*, Ed. by A. V. Borisov, I. S. Mamaev, and M. A. Sokolovskiĭ (IKI, Moscow, 2003).
4. L. G. Kurakin and V. I. Yudovich, Dokl. Akad. Nauk **384**, 476 (2002) [Dokl. Phys. **47**, 465 (2002)].
5. L. G. Kurakin and V. I. Yudovich, Chaos **12**, 574 (2002).
6. V. A. Bogomolov, Fiz. Atm. Okeana **15**, 243 (1979).
7. S. Pekarsky and J. Marsden, J. Math. Phys. **39**, 5894 (1998).
8. A. V. Borisov and A. V. Kilin, Reg. Chaot. Dyn. **2** (2), 189 (2000).
9. L. G. Kurakin, Dokl. Akad. Nauk **388**, 482 (2003) [Dokl. Phys. **48**, 84 (2003)].
10. L. J. Campbell, Phys. Rev. A **24**, 514 (1981).
11. T. H. Havelock, Philos. Mag. **11**, 617 (1931).
12. A. P. Markeev, *Libration Points in Celestial Mechanics and Space Dynamics* (Nauka, Moscow, 1978).
13. V. I. Arnold, Usp. Mat. Nauk **18** (5), 13 (1963).
14. J. Mozer, *Lectures on Hamiltonian Systems* (Mir, Moscow, 1973).

Translated by K. Kugel

Doklady Physics, Vol. 49, No. 11, 2004, pp. 662–667. Translated from Doklady Akademii Nauk, Vol. 399, No. 1, 2004, pp. 56–61.

MECHANICS

Helical Dipole

V. L. Okulov and Y. Fukumoto

Presented by Academician G.G. Chernyĭ June 2, 2004

Received May 27, 2004

Investigation of helical vortices is of fundamental importance for fluid mechanics, as they determine one of the basic states of swirling flows. A wide variety of examples of helical vortices are described in the literature. These include tip vortices in the wakes behind propellers, screws, and wind turbines; concentric vortices in rotating reservoirs; tornados; swirls in a fluid escaping from a vessel; vortex structures arising after vortex breakdown behind a delta-shaped wing and in pipes; longitudinal vortex structures in a boundary layer; vortex filaments in a flow of superfluid helium; paraxial vortices in vortex facilities, etc. In just the same way as point vortices and infinitely thin vortex rings are fundamental objects in the vortex dynamics of ideal incompressible fluids, infinitely thin helical filaments are elementary models of the above structures. However, there are difficulties in describing them because, for a helical filament, the Biot–Savart integral cannot be evaluated in closed form. For the uniform distribution of the intensity of the pole-type vorticity along a helical filament, an alternative representation of the solution was found in [1] as a trigonometric series with coefficients in the form of products of modified Bessel functions. For calculating these coefficients, an efficient algorithm was proposed in [2, 3] with the singularity separation in the solution. In the present study, we investigate a flow induced by an infinitely thin helical filament with a uniform distribution of the dipole-type vorticity. This elementary vortex structure is a fundamental object of helical-vortex dynamics, which is second in the order of importance, just like a point dipole in the plane theory of vortices.

In an unbounded space, we consider a helical filament characterized by a helical pitch $h = 2\pi l$ and winded round a cylinder of radius a. In terms of cylindrical coordinates (r, ϕ, z), the helical filament is determined by the equations

$$x' = a\cos\phi, \quad y' = a\sin\phi, \quad z' = l\phi. \qquad (1)$$

Its arc element is $ds = d\phi\sqrt{a^2 + l^2}$, and the triplet of basis vectors is

$$\mathbf{t} = \frac{a}{\sqrt{a^2 + l^2}}\left[-\sin\phi, \cos\phi, \frac{l}{a}\right],$$

$$\mathbf{n} = [-\cos\phi, -\sin\phi, 0],$$

$$\mathbf{b} = \frac{l}{\sqrt{a^2 + l^2}}\left[\sin\phi, -\cos\phi, \frac{a}{l}\right].$$

The curvature and torsion of the filament are $\kappa = \frac{a}{a^2 + l^2}$ and $\tau = \frac{l}{a^2 + l^2}$, respectively.

The vector potential of the induced flow can be represented in the form

$$\mathbf{A} = \nabla \times \mathbf{D} = \oint \frac{\mathbf{d}(s) \times |\mathbf{x} - \mathbf{x}'(s)|}{|\mathbf{x} - \mathbf{x}'(s)|^3} ds, \qquad (2)$$

where $D = \oint \frac{\mathbf{d}(s)ds}{|\mathbf{x} - \mathbf{x}'(s)|}$, the dipole-moment intensity being $d = |\mathbf{d}(s)|$. Without loss of generality, we align the dipole-moment vector with the direction of the binormal $\mathbf{b}$ to the helical filament:

$$\mathbf{d}(s)ds = d \cdot \mathbf{b}ds = d[l\sin\theta, -l\cos\theta, a]d\theta.$$

In this case, vector $\mathbf{D}$ can be rewritten in the form

$$\mathbf{D} = d(-l\mathrm{Re}[ie^{-i\phi}I(1)], -l\mathrm{Im}[ie^{-i\phi}I(1)], aI(0)), \qquad (3)$$

where

$$I(\alpha) = \int_{-\infty}^{\infty} \frac{\exp(i\alpha\theta)d\theta}{(r^2 + a^2 - 2ar\cos(\phi - \theta) + (z - l\theta)^2)^{1/2}}.$$

Institute of Thermophysics, Siberian Division, Russian Academy of Sciences, pr. Lavrent'eva 1, Novosibirsk, 630090 Russia
e-mail: vokulov@mail.ru
Graduate School of Mathematics and Space Environment Research Center, Kyushu University, 33, Fukuoka 812-8581, Japan

1028-3358/04/4911-0662$26.00 © 2004 MAIK "Nauka/Interperiodica"

In accordance with [1], we have

$$I(0) = \frac{2}{l}\left\{\begin{array}{c} -\ln a \\ -\ln r \end{array}\right\} + \frac{4}{l}\mathrm{Re}\left\{\begin{array}{c} H_0^{0,0}\left(\frac{r}{l}, \frac{a}{l}, \chi\right) \\ H_0^{0,0}\left(\frac{a}{l}, \frac{r}{l}, \chi\right) \end{array}\right\} + \frac{2}{l}C_\infty,$$

$$I(1) = \frac{\exp(i\phi)}{l}\left[\left\{\begin{array}{c} \frac{r}{a} \\ \frac{a}{r} \end{array}\right\}\right.$$

$$-4\mathrm{Re}\left(\left\{\begin{array}{c} H_0^{1,1}\left(\frac{r}{l}, \frac{a}{l}, \chi\right) \\ H_0^{1,1}\left(\frac{a}{l}, \frac{r}{l}, \chi\right) \end{array}\right\} + \frac{l^2}{ra}\left\{\begin{array}{c} H_0^{0,0}\left(\frac{r}{l}, \frac{a}{l}, \chi\right) \\ H_0^{0,0}\left(\frac{a}{l}, \frac{r}{l}, \chi\right) \end{array}\right\}\right)$$

$$\left.+4i\mathrm{Im}\left(\frac{l}{r}\left\{\begin{array}{c} H_0^{0,1}\left(\frac{r}{l}, \frac{a}{l}, \chi\right) \\ H_0^{1,0}\left(\frac{a}{l}, \frac{r}{l}, \chi\right) \end{array}\right\} + \frac{l}{a}\left\{\begin{array}{c} H_0^{1,0}\left(\frac{r}{l}, \frac{a}{l}, \chi\right) \\ H_0^{0,1}\left(\frac{a}{l}, \frac{r}{l}, \chi\right) \end{array}\right\}\right)\right],$$

where

$$H_M^{I,J}(x, y, \chi) = \sum_{m=1}^{\infty} m^M I_m^{\langle I\rangle}(mx) K_m^{\langle J\rangle}(my) \cdot e^{im\chi} = \sum_{m=1}^{\infty} hi_m(x, y, I, J, M) \cdot e^{im\chi} \quad (4)$$

are series of the Kapteyn's type; $\chi = \phi - \frac{z}{l}$; $I_m(\cdot)$ and $K_m(\cdot)$ are modified Bessel functions on the order of m; the conditions $I, J = 0$ determine the functions, while the conditions $I, J = 1$ determine their derivatives; the indeterminate constant C_∞ does not depend on a and r; and the upper and lower rows in braces correspond to $r < a$ and $r \geq a$, respectively.

If we substitute $I(1)$ and $I(0)$ into (3) and apply to the result the curl operator in accordance with definition (2), the components of the vector potential for the flow induced by a dipole vortex helical filament are written in the form

$$A_r = -\frac{4d}{l}\mathrm{Im}\left[\left\{\begin{array}{c} H_1^{1,1}\left(\frac{r}{l}, \frac{a}{l}, \chi\right) \\ H_1^{1,1}\left(\frac{a}{l}, \frac{r}{l}, \chi\right) \end{array}\right\}\right.$$

$$\left.+\frac{a^2 + l^2}{ra}\left\{\begin{array}{c} H_1^{0,0}\left(\frac{r}{l}, \frac{a}{l}, \chi\right) \\ H_1^{0,0}\left(\frac{a}{l}, \frac{r}{l}, \chi\right) \end{array}\right\}\right],$$

$$A_\phi = \frac{2a}{l}\left\{\begin{array}{c} 0 \\ \frac{a}{r} \end{array}\right\} - 4d\mathrm{Re}\left(\frac{1}{r}\left\{\begin{array}{c} H_1^{0,1}\left(\frac{r}{l}, \frac{a}{l}, \chi\right) \\ H_1^{1,0}\left(\frac{a}{l}, \frac{r}{l}, \chi\right) \end{array}\right\}\right. \quad (5)$$

$$\left.+\frac{a^2 + l^2}{al^2}\left\{\begin{array}{c} H_1^{1,0}\left(\frac{r}{l}, \frac{a}{l}, \chi\right) \\ H_1^{0,1}\left(\frac{a}{l}, \frac{r}{l}, \chi\right) \end{array}\right\}\right),$$

$$A_z = 2d\left\{\begin{array}{c} -\frac{1}{a} \\ 0 \end{array}\right\} + \frac{4d}{l}\mathrm{Re}\left\{\begin{array}{c} H_1^{0,1}\left(\frac{r}{l}, \frac{a}{l}, \chi\right) \\ H_1^{1,0}\left(\frac{a}{l}, \frac{r}{l}, \chi\right) \end{array}\right\}.$$

Employing the dependence of vector potential (5) only on two helical variables r and χ and taking into account the obvious relation

$$\nabla \cdot (\mathrm{curl}\mathbf{A}) = \frac{\partial}{\partial r}[r(\mathrm{curl}\mathbf{A})_r] + \frac{\partial}{\partial \chi}\left((\mathrm{curl}\mathbf{A})_\phi - \frac{r}{l}(\mathrm{curl}\mathbf{A})_z\right) = 0,$$

where the $\mathrm{curl}\mathbf{A}(r, \chi) = (A_r, A_\phi, A_z)$ is given by the relations

$$(\mathrm{curl}\mathbf{A})_r = \frac{1}{r}\frac{\partial}{\partial \chi}\left(A_z + \frac{r}{l}A_\phi\right),$$

$$(\mathrm{curl}\mathbf{A})_\phi = -\frac{1}{l}\frac{\partial A_r}{\partial \chi} - \frac{\partial A_z}{\partial r}, \quad (6)$$

$$(\mathrm{curl}\mathbf{A})_z = -\frac{1}{r}\frac{\partial A_r}{\partial \chi} + \frac{1}{r}\frac{\partial (rA_\phi)}{\partial r},$$

we can introduce an analog of the stream function for the flow under consideration,

$$\psi = A_z + \frac{r}{l}A_\phi = \frac{2d}{l}\begin{Bmatrix} -\frac{l}{a} \\ \frac{a}{l} \end{Bmatrix} - \frac{4dr}{al}\frac{a^2+l^2}{l^2}\mathrm{Re}\begin{Bmatrix} H_1^{1,0}\left(\frac{r}{l}, \frac{a}{l}, \chi\right) \\ H_1^{0,1}\left(\frac{a}{l}, \frac{r}{l}, \chi\right) \end{Bmatrix}. \quad (7)$$

According to relation (6), the components of the velocity field $\mathbf{u} = (u_r, u_\phi, u_z)$ can be obtained by directly differentiating the vector potential in (5). As a result, we arrive at

$$u_r = (\mathrm{curl}\mathbf{A})_r = 4d\frac{a^2+l^2}{al^3}\mathrm{Im}\begin{Bmatrix} H_2^{1,0}\left(\frac{r}{l}, \frac{a}{l}, \chi\right) \\ H_2^{0,1}\left(\frac{a}{l}, \frac{r}{l}, \chi\right) \end{Bmatrix},$$

$$u_\phi = (\mathrm{curl}\mathbf{A})_\phi = 4d\frac{a^2+l^2}{ral^3}\mathrm{Re}\begin{Bmatrix} H_2^{0,0}\left(\frac{r}{l}, \frac{a}{l}, \chi\right) \\ H_2^{0,0}\left(\frac{a}{l}, \frac{r}{l}, \chi\right) \end{Bmatrix}, \quad (8)$$

$$u_z = (\mathrm{curl}\mathbf{A})_z = -4d\frac{a^2+l^2}{al^3}\mathrm{Re}\begin{Bmatrix} H_2^{0,0}\left(\frac{r}{l}, \frac{a}{l}, \chi\right) \\ H_2^{0,0}\left(\frac{a}{l}, \frac{r}{l}, \chi\right) \end{Bmatrix}.$$

A direct verification proves that the projection of the velocity onto the unit vector tangential to helical lines collinear to the filament given by (1) vanishes (that is, $u_\tau = u_z + \frac{ru_\phi}{l} = 0$) and that the velocity component orthogonal to u_r and u_τ has the form

$$u_\chi = u_\phi - \frac{ru_z}{l} = \frac{4d}{rl^2}\left(1 + \frac{r^2}{l^2}\right)\mathrm{Re}\begin{Bmatrix} H_2^{0,0}\left(\frac{r}{l}, \frac{a}{l}, \chi\right) \\ H_2^{0,0}\left(\frac{a}{l}, \frac{r}{l}, \chi\right) \end{Bmatrix}.$$

We note that both nonzero orthogonal velocity components, u_r and u_χ, can be obtained with the aid of stream function (7) as $u_r = \frac{\partial\psi}{r\partial\chi}$ and $u_\chi = -\frac{\partial\psi}{\partial r}$. This yields

$$u_\phi = -\frac{l}{r}u_z = \frac{l^2}{r^2+l^2}u_\chi = -\frac{l^2}{r^2+l^2}\frac{\partial\psi}{\partial r},$$

$$u_z = -\frac{r}{l}u_\phi = -\frac{l^2}{r^2+l^2}\frac{r}{l}u_\chi = \frac{l^2}{r^2+l^2}\frac{r}{l}\frac{\partial\psi}{\partial r}.$$

The above relations between the velocity components u_ϕ and u_z make it possible to analyze below only one of them, e.g., component u_z.

In order to complete the investigation of the problem, it only remains to indicate a simple and efficient procedure for calculating Kapteyn's type series (4). As is shown in Fig. 1a, the coefficients hi_m in the trigonometric series (4) increase with m. Naturally, this hampers numerical summation of these series in calculating the kinematic features of the flow, especially in the vicinity of the circle $r = a$. In order to calculate the velocity field induced by a dipole helical vortex filament in the entire space, we generalize the method used in [3, 4] to separate the leading part of the series in (4). This method was used to calculate the kinematic features of monopole helical filaments at the points lying on the circumference $r = a$. With this goal, we represent series (4) in the form

$$H_M^{I,J}(x, y, \chi) = \lambda^{I,J}\left[b_{M,0}^{I,J}\frac{e^{\xi+i\chi}}{(e^\xi - e^{i\chi})^2} + b_{M,1}^{I,J}\frac{e^{i\chi}}{e^\xi - e^{i\chi}} + b_{M,2}^{I,J}\ln(1 - e^{-\xi+i\chi}) + b_{M,3}^{I,J}\mathrm{Li}_2(e^{-\xi+i\chi}) + b_{M,4}^{I,J}\mathrm{Li}_3(e^{-\xi+i\chi})\right] + R_M^{I,J}(x, y, \chi), \quad (9)$$

where $\mathrm{Li}_k(z) = \sum_{m=1}^{\infty}\frac{z^m}{m^k}$ ($|z| < 1$) are polylogarithms,

$$e^\xi = \frac{x}{y}\frac{\exp(\sqrt{1+x^2})(1+\sqrt{1+y^2})}{\exp(\sqrt{1+y^2})(1+\sqrt{1+x^2})},$$

$$\lambda^{I,J} = \frac{1}{2}\frac{(\sqrt{1+x^2})^{I-1/2}(\sqrt{1+y^2})^{J-1/2}}{x^I(-y)^J},$$

$$\mathbf{b}^{I,J} = \begin{bmatrix} 0 & 0 & 1 & \alpha^{I,J} & \beta^{I,J} & \gamma^{I,J} \\ 0 & 1 & \alpha^{I,J} & \beta^{I,J} & \gamma^{I,J} & 0 \\ 1 & \alpha^{I,J} & \beta^{I,J} & \gamma^{I,J} & 0 & 0 \end{bmatrix}.$$

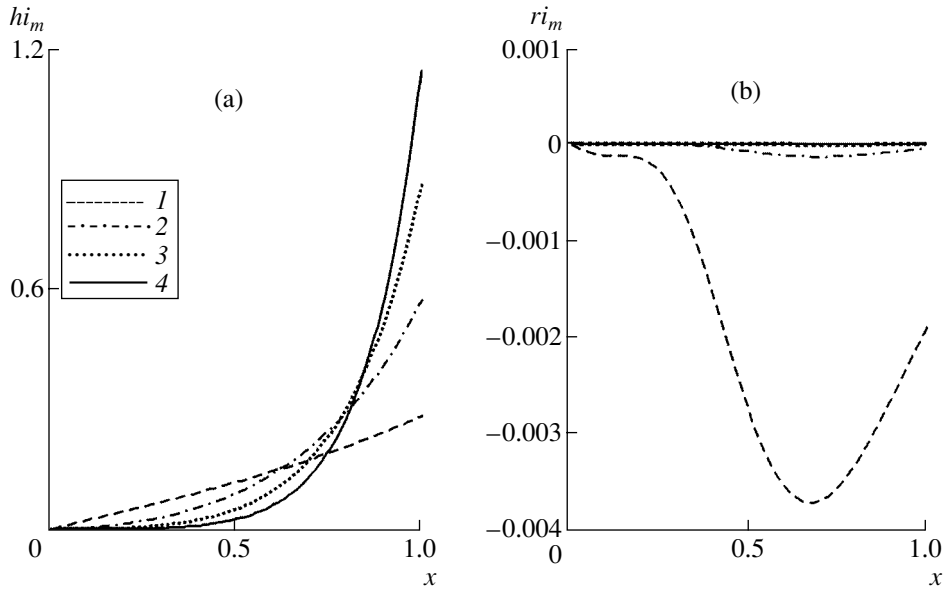

Fig. 1. Coefficients in the trigonometric (a) Kapteyn's series and (b) residual series after the separation of a singularity for the first four terms of the series; m = (*1*) 1, (*2*) 2, (*3*) 3, and (*4*) 4.

The coefficients $\mathbf{b}^{I,J}$, which are used to calculate the velocity over the entire space, are given by

$$\alpha^{I,J}(x,y) = (1-I)\vartheta_1(x) - (1-J)\vartheta_1(y) + I\upsilon_1(x) - J\upsilon_1(y),$$

$$\beta^{I,J}(x,y) = (1-I)\vartheta_2(x) + (1-J)\vartheta_2(y) + I\upsilon_2(x) + J\upsilon_2(y) - (1-I)(1-J)\vartheta_1(x)\vartheta_1(y) - J(1-I)\vartheta_1(x)\upsilon_1(y) - I(1-J)\vartheta_1(y)\upsilon_1(x) - IJ\upsilon_1(x)\upsilon_1(y),$$

$$\gamma^{I,J}(x,y) = (1-I)\vartheta_3(x) - (1-J)\vartheta_3(y) + I\upsilon_3(x) - J\upsilon_3(y) + (1-I)(1-J)[\vartheta_1(x)\vartheta_2(y) - \vartheta_2(x)\vartheta_1(y)] + J(1-I)[\vartheta_1(x)\upsilon_2(y) - \vartheta_2(x)\upsilon_1(y)] - I(1-J)[\vartheta_2(y)\upsilon_1(x) - \vartheta_1(y)\upsilon_2(x)] + IJ[\upsilon_1(x)\upsilon_2(y) - \upsilon_2(x)\upsilon_1(y)].$$

The functions appearing in the definitions of $\alpha^{I,J}$, $\beta^{I,J}$, and $\gamma^{I,J}$ are polynomials in terms of $t = (1+x^2)^{-1/2}$,

$$\vartheta_1 = \frac{1}{24}(3t - 5t^3), \quad \upsilon_1 = \frac{1}{24}(-9t + 7t^3),$$

$$\vartheta_2 = \frac{1}{1152}(81t^2 - 462t^4 + 385t^6),$$

$$\upsilon_2 = \frac{1}{1152}(-135t^2 + 594t^4 - 455t^6),$$

$$\vartheta_3 = \frac{1}{414720}(30375t^3 - 369603t^5 + 765765t^7 - 425425t^9),$$

$$\upsilon_3 = \frac{1}{414720}(-42525t^3 + 451737t^5 - 883575t^7 + 47547t^9),$$

while a small regular residue is determined by the relation

$$R_M^{I,J} = \sum_{m=1}^{\infty} ri_m(x,y,I,J,M)\cdot e^{im\chi} = \sum_{m=1}^{\infty}[m^M I_m^{\langle I\rangle}(mx)K_m^{\langle J\rangle}(my) - m^M\lambda^{I,J}(e^{\xi})^m\left(1 + \frac{\alpha^{I,J}}{m} + \frac{\beta^{I,J}}{m^2} + \frac{\gamma^{I,J}}{m^3}\right)]e^{im\chi}. \quad (10)$$

Figure 1b shows the behavior of the coefficients ri_m in residual trigonometric series (10). In contrast to what we have for the series in (4), these coefficients are small and rapidly decrease with increasing m. By virtue of this fact, the representation in (9) is more convenient in performing calculations.

In accordance with (9), the exact solution to the problem, where the singularities are separated, can be

rewritten for the stream function in the form

$$\psi = \frac{2d}{l}\begin{Bmatrix} -\frac{l}{a} \\ \frac{a}{l} \end{Bmatrix} - \frac{4dr}{al}\frac{a^2+l^2}{l^2}\lambda^{1,0}\left(\frac{r}{l},\frac{a}{l}\right)$$

$$\times \mathrm{Re}\left[\frac{\pm e^{i\chi}}{e^{\mp\xi}-e^{i\chi}} + \alpha^{1,0}\left(\frac{r}{l},\frac{a}{l}\right)\ln(1-e^{\pm\xi+i\chi})\right. \quad (11)$$

$$\left. \pm \beta^{1,0}\left(\frac{r}{l},\frac{a}{l}\right)\mathrm{Li}_2(e^{\pm\xi+i\chi}) + \gamma^{1,0}\left(\frac{r}{l},\frac{a}{l}\right)\mathrm{Li}_3(e^{\pm\xi+i\chi})\right]$$

$$-\frac{4dr}{al}\frac{a^2+l^2}{l^2}\mathrm{Re}\begin{Bmatrix} R_1^{1,0}\left(\frac{r}{l},\frac{a}{l},\chi\right) \\ R_1^{0,1}\left(\frac{a}{l},\frac{r}{l},\chi\right) \end{Bmatrix}.$$

The corresponding representation for the velocity components u_r and u_z takes the form

$$u_r = 4d\frac{a^2+l^2}{al^3}\lambda^{1,0}\left(\frac{r}{l},\frac{a}{l}\right)\mathrm{Im}\left[\frac{\pm e^{\mp\xi+i\chi}}{(e^{\mp\xi}-e^{i\chi})^2}\right.$$

$$+ \alpha^{1,0}\left(\frac{r}{l},\frac{a}{l}\right)\frac{e^{i\chi}}{e^{\mp\xi}-e^{i\chi}} \pm \beta^{1,0}\left(\frac{r}{l},\frac{a}{l}\right)\ln(1-e^{\pm\xi+i\chi})$$

$$\left. + \gamma^{1,0}\left(\frac{r}{l},\frac{a}{l}\right)\mathrm{Li}_2(e^{\pm\xi+i\chi})\right] + 4d\frac{a^2+l^2}{al^3}\mathrm{Im}\begin{Bmatrix} R_2^{1,0}\left(\frac{r}{l},\frac{a}{l},\chi\right) \\ R_2^{0,1}\left(\frac{a}{l},\frac{r}{l},\chi\right) \end{Bmatrix}, \quad (12)$$

$$u_z = -4d\frac{a^2+l^2}{al^3}\lambda^{0,0}\left(\frac{r}{l},\frac{a}{l}\right)\mathrm{Re}\left[\frac{e^{\mp\xi+i\chi}}{(e^{\mp\xi}-e^{i\chi})^2}\right.$$

$$+ \alpha^{0,0}\left(\frac{r}{l},\frac{a}{l}\right)\frac{e^{i\chi}}{e^{\mp\xi}-e^{i\chi}} + \beta^{0,0}\left(\frac{r}{l},\frac{a}{l}\right)\ln(1-e^{\pm\xi+i\chi})$$

$$\left. \pm \gamma^{0,0}\left(\frac{r}{l},\frac{a}{l}\right)\mathrm{Li}_2(e^{\pm\xi+i\chi})\right] - 4d\frac{a^2+l^2}{al^3}\mathrm{Re}\begin{Bmatrix} R_2^{0,0}\left(\frac{r}{l},\frac{a}{l},\chi\right) \\ R_2^{0,0}\left(\frac{a}{l},\frac{r}{l},\chi\right) \end{Bmatrix}.$$

The solution given by (11) and (12) is exact. However, for a number of practical problems in which an accuracy of up to 5% is sufficient [3, 4], one can retain only the first two terms in (9). Upon specifying the values of the coefficients λ and α, the approximate formula for the stream function can be rewritten as

$$\psi \simeq \frac{2d}{l}\begin{Bmatrix} -\frac{l}{a} \\ \frac{a}{l} \end{Bmatrix} - \frac{2d}{al^2}(l^2+a^2)^{3/4}\sqrt[4]{l^2+r^2}\,\mathrm{Re}\left[\frac{\pm e^{i\chi}}{e^{\mp\xi}-e^{i\chi}}\right]$$

$$-\frac{d}{12al}(l^2+a^2)^{3/4}\sqrt[4]{l^2+r^2} \quad (13)$$

$$\times\left(\frac{2l^2-3a^2}{(l^2+a^2)^{3/2}} - \frac{9r^2+2l^2}{(l^2+r^2)^{3/2}}\right)\mathrm{Re}[\ln(1-e^{\pm\xi+i\chi})].$$

The corresponding reduced representation of the velocity field takes the form

$$u_r \simeq \frac{2d}{arl^2}(l^2+a^2)^{3/4}\sqrt[4]{l^2+r^2}\,\mathrm{Im}\left[\frac{\pm e^{\mp\xi+i\chi}}{(e^{\mp\xi}-e^{i\chi})^2}\right.$$

$$\left. + \frac{l}{24}\left(\frac{2l^2-3a^2}{(l^2+a^2)^{3/2}} - \frac{9r^2+2l^2}{(l^2+r^2)^{3/2}}\right)\frac{e^{i\chi}}{e^{\mp\xi}-e^{i\chi}}\right], \quad (14)$$

$$u_z \simeq -\frac{2d}{al^2}\frac{(l^2+a^2)^{3/4}}{\sqrt[4]{(l^2+r^2)}}\mathrm{Re}\left[\frac{e^{\mp\xi+i\chi}}{(e^{\mp\xi}-e^{i\chi})^2}\right.$$

$$\left. \pm \frac{l}{24}\left(\frac{3r^2-2l^2}{(l^2+r^2)^{3/2}} - \frac{3a^2-2l^2}{(l^2+a^2)^{3/2}}\right)\frac{e^{i\chi}}{e^{\mp\xi}-e^{i\chi}}\right].$$

In Fig. 2, the variation in the structure of the flow induced by a helical vortex filament is shown for various values of the helical pitch (h = 1, 2, 8) and the same radius (a = 1.5). The filament is characterized by a uniform distribution of dipoles having the intensity d = 0.1. Isolines of the stream function are constructed with a uniform step equal to two. The flow patterns differ quite significantly. At a large pitch (h = 8), the stream function resembles that for a point dipole, but there is a modest asymmetric distortion of the stream lines with respect to the dipole axis. As the pitch decreases, the flow pattern exhibits noticeable changes associated with the concentration of the flow along the cylinder (a = 1.5). In order to describe the structure of the flow more exactly, we consider the velocity field. In Fig. 3, we compare the velocity profiles for the same three vortex filaments. At a large helical pitch of a filament, there are no significant distinctions from the velocity profiles of the flow induced by a point dipole. However, a decrease in the filament pitch results in a significant rearrangement of the flow: there arises intense motion of the fluid along the surface of the cylinder (a = 1.5).

Thus, the solution for a flow induced by a helical vortex filament having a uniform dipole distribution of

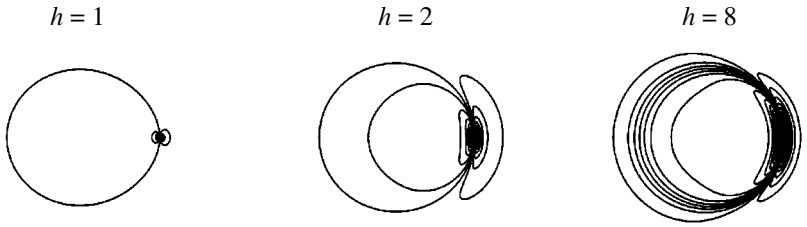

Fig. 2. Stream-function isolines for a vortex filament having dipole-type vorticity distribution and various values of the helical pitch: $h = 1$, 2, and 8.

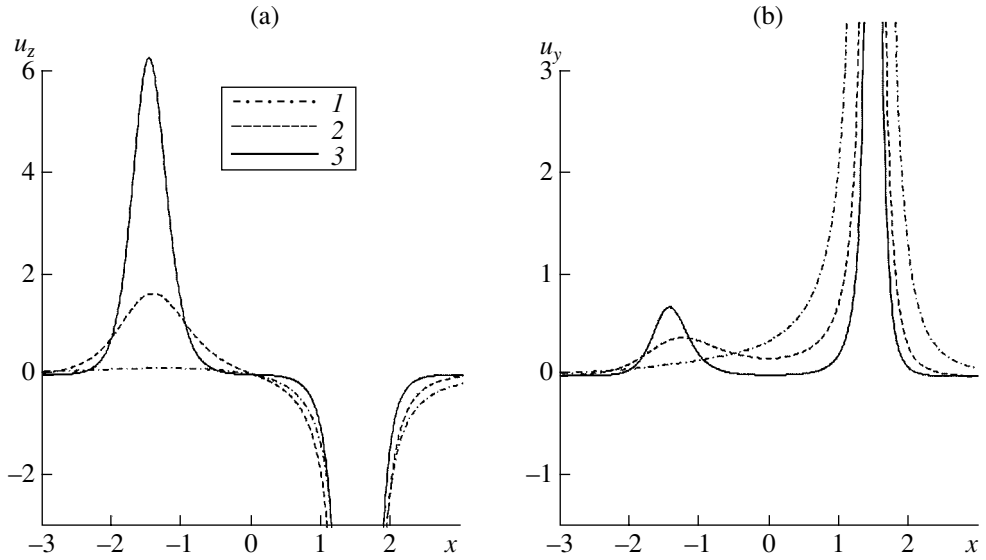

Fig. 3. Velocity-component profiles along the x axis, which are induced by a helical vortex filament having dipole-type vorticity distribution and various values of the helical pitch: $h = (3)$ 1, (2) 2, and (1) 8. The results are given for the velocity component along the symmetry axis (u_z) and for the azimuth velocity component (u_ϕ). In Fig. 3b $u_y = u_\phi$ for $x > 0$ and $u_y = -u_\phi$ for $x < 0$.

vorticity has been obtained. A simple analytical form of the solution makes it possible to efficiently analyze the flow structure and to use the solution in constructing more advanced hydrodynamic models.

ACKNOWLEDGMENTS

This work was supported in part by JSPS and the Russian Foundation for Basic Research, project no. 04-01-00124.

REFERENCES

1. J. C. Hardin, Phys. Fluids **25**, 1949 (1982).
2. V. L. Okulov, Russ. J. Eng. Thermophys. **5**, 63 (1995).
3. V. L. Okulov, Pis'ma Zh. Tekh. Fiz. **28** (24), 80 (2002) [Tech. Phys. Lett. **28**, 1060 (2002)].
4. V. L. Okulov, J. Fluid Mech. (2004, in press).

Translated by T. Syromyatnikova

Doklady Physics, Vol. 49, No. 11, 2004, pp. 668–672. Translated from Doklady Akademii Nauk, Vol. 399, No. 2, 2004, pp. 188–191.

MECHANICS

Certain Asymptotic Formulas in the Problem of the Beginning of Deformation of a Gas Bubble and Its Collapse

D. V. Georgievskiĭ and A. V. Zhdanova

Presented by Academician I.G. Goryacheva February 19, 2004

Received February 24, 2004

The spherically symmetric collapse of a bubble in a continuum under pressure at infinity is one of the classical problems of continuum mechanics and can be integrated in many cases [1–12]. The problem of the beginning of the deformation and complete filling (collapse) of a bubble filled with a barotropic gas in an inhomogeneous viscoplastic medium with radius-dependent yield stress is analytically analyzed. Certain asymptotic formulas for such a system are derived, and qualitative features of its behavior are revealed.

1. We consider the evolution of radius $R(t)$ of a spherical gas bubble in an incompressible viscoplastic medium under pressure p_∞ at infinity. Let the gas be barotropic and the process for $r < R(t)$ be close to adiabatic, so that pressure p_g is identical at all points $r < R(t)$ up to the boundary $r = R(t)$ and is related to gas density ρ_g by the adiabatic law,

$$p_g = p_g^0\left(\frac{\rho_g}{\rho_g^0}\right)^\gamma, \quad \gamma > 0. \tag{1}$$

Therefore, pressure is related to the bubble radius as

$$p_g = \frac{C}{R^{3\gamma}}, \tag{2}$$

where the constant C characterizes the total mass of the gas inside the bubble.

We assume that the center O of the bubble is at rest and the yield stress τ_s of the surrounding medium depends on the distance from the point O, which is taken as the center of the spherical coordinate system (r, θ, φ), where θ is the polar angle. Density ρ and dynamic viscosity μ does not vary for $r > R(t)$. A particular case, where τ is a step function of r such that $\tau \equiv 0$ beginning with a certain r, was studied in [6, 11]. The dependences of the coefficients under investigation simulate, in particular, the collapse of the bubble in the large volume of a viscoplastic or ideally plastic material (the characteristic size of this volume is much larger than the initial radius of the bubble) that is surrounded by either a viscous medium with the same viscosity or an ideal liquid.

To construct dimensionless parameters, we use initial radius $R(0)$, density ρ, and pressure p_∞. In addition to the adiabatic index γ, the problem involves three dimensionless governing parameters,

$$\mathrm{Re} = \frac{R(0)\sqrt{\rho p_\infty}}{\mu}, \quad c = \frac{C}{(R(0))^{3\gamma} p_\infty},$$

$$v_0 = \dot{R}(0)\sqrt{\frac{\rho}{p_\infty}}$$

and one function $\tau(r) = \dfrac{\tau_s(r)}{p_\infty}$. All further relations are written in a dimensionless form.

We assume that the motion of the bubble-surrounding medium is radial ($v_\theta = v_\varphi \equiv 0$). In this case, the incompressibility condition provides the following relations for the radial velocity component $v_r \equiv v(r, t)$ and components v_{rr}, $v_{\theta\theta}$, and $v_{\varphi\varphi}$ of the strain rate tensor $\underset{\sim}{v}(r, t)$:

$$v = -\frac{V(t)}{r^2}, \quad v_{rr} = \frac{2V(t)}{r^3}, \quad v_{\theta\theta} = v_{\varphi\varphi} = -\frac{V(t)}{r^3}, \tag{3}$$

where $V(t)$ is an unknown function. The only equation of motion,

$$\frac{\partial \sigma_{rr}}{\partial r} + \frac{1}{r}(2\sigma_{rr} - \sigma_{\theta\theta} - \sigma_{\varphi\varphi}) = \frac{\partial v}{\partial t} + v\frac{\partial v}{\partial r} \tag{4}$$

is complemented by the boundary conditions

$$\sigma_{rr}(\infty, t) = -1, \quad \sigma_{rr}(R(t), t) = -\frac{c}{R^{3\gamma}} \tag{5}$$

Moscow State University,
Vorob'evy gory, Moscow, 119992 Russia
e-mail: georgiev@mech.math.msu.su

1028-3358/04/4911-0668$26.00

and initial conditions

$$R(0) = 1, \quad \dot{R}(0) = v_0. \tag{6}$$

Taking into account Eq. (3) and relation $V(t) = -R^2(t)\dot{R}(t)$ following from Eq. (3) for $r = R(t)$, we integrate Eq. (4) with respect to r from R to infinity and use boundary conditions (5). Since $\sigma_{\theta\theta} = \sigma_{\varphi\varphi}$ for the spherically symmetric case, we obtain

$$\frac{c}{R^{3\gamma}} - 1 + 2\int_r^\infty \frac{\sigma_{rr} - \sigma_{\theta\theta}}{r} dr = R\ddot{R} + \frac{3}{2}\dot{R}^2. \tag{7}$$

For the viscoplastic medium (Shvedov–Bingham model),

$$\underset{\sim}{\sigma} = -p\underset{\sim}{I} + 2\left(\frac{\tau}{\sqrt{2\underset{\sim}{\nu} : \underset{\sim}{\nu}}} + \frac{1}{\mathrm{Re}}\right)\underset{\sim}{\nu}, \tag{8}$$

where $\underset{\sim}{I}$ is the identity tensor under kinematic constraints (3), and the tensor constitutive relationships have the form

$$\begin{aligned} \sigma_{rr} &= -p + 2\left(\frac{\tau}{\sqrt{3}}\mathrm{sgn}V + \frac{2V}{r^3\mathrm{Re}}\right), \\ \sigma_{\theta\theta} &= -p - \left(\frac{\tau}{\sqrt{3}}\mathrm{sgn}V + \frac{2V}{r^3\mathrm{Re}}\right). \end{aligned} \tag{9}$$

The substitution of Eq. (9) into Eq. (7) and certain manipulations yield ($\mathrm{sgn}V = -\mathrm{sgn}\dot{R}$)

$$R\ddot{R} + \frac{3}{2}\dot{R}^2 = -\frac{4\dot{R}}{R\mathrm{Re}} - T(R)\mathrm{sgn}\dot{R} + \frac{c}{R^{3\gamma}} - 1, \tag{10}$$

$$T(R) = 2\sqrt{3}\int_R^\infty \frac{\tau(r)}{r} dr. \tag{11}$$

Since Eq. (10) is free of the independent variable t, the order of this equation can be reduced. The Cauchy problem given by Eqs. (10) and (6) is equivalent to the first-order differential equation

$$RQQ' + \frac{3}{2}Q^2 = -\frac{4Q}{R\mathrm{Re}} - T(R)\mathrm{sgn}Q + \frac{c}{R^{3\gamma}} - 1 \tag{12}$$

for the function $Q(R) = \dot{R}$ with the initial condition

$$Q(1) = v_0. \tag{13}$$

We note that the first terms on the right-hand sides of Eqs. (10) and (12) are proportional to the medium viscosity (these terms are absent for an ideal liquid or an ideally plastic body). The second terms are related to the yield stress $\tau(r)$ and the third terms are due to the fact that the bubble is filled with a gas. Therefore, the effect of these parameters on the evolution of the radius $R(t)$ can be studied independently or additively in various combinations.

The medium cannot be homogeneous in terms of the yield stress, because integral (11) diverges at infinity for $\tau = \mathrm{const}$. This means that infinite external or internal pressure must be applied for the beginning of compression or expansion. The convergence of integral (11) at infinity is a necessary and sufficient condition for choosing the function $\tau(r)$.

2. Equations (10) and (12) can be integrated in quadratures for $\mathrm{Re} = \infty$, i.e., for an inviscid medium surrounding the bubble. In this case, multiplying Eq. (12) by the factor $2R^2$ and integrating, we obtain

$$\begin{aligned} Q^2(R) &= \mp\frac{2}{R^3}\int R^2 T(R) dR \\ &\times \begin{cases} -\dfrac{2c}{3(\gamma-1)R^{3\gamma}}, & \gamma \neq 1, \\ +\dfrac{2c\ln R}{R^3}, & \gamma = 1, \end{cases} \quad -\frac{2}{3} + \frac{k}{R^3}, \end{aligned} \tag{14}$$

where the constant k is determined from condition (13). The upper and lower signs in Eq. (14) correspond to $Q > 0$ (expansion) and $Q < 0$ (compression). It is *a priori* unknown which of these two processes proceeds at any given time. This is a feature of—and traditional difficulty in—problems of the flow of media with the yield point [6, 7].

Owing to the existence of viscosity, analysis is complicated, and the evolution of radius $R(t)$ depends on one more parameter, Reynolds number Re. Even for the classical Zababakhin problem [3] on the filling of a vacuum bubble in a Newtonian viscous fluid with zero initial velocity, two substantially different regimes are known. In regime A for $\mathrm{Re} \gtrsim 8.4$, as well as in the Rayleigh problem, the bubble is filled in a finite time and $Q \sim -R^{-3/2}$ for $R \longrightarrow 0$ [$R \sim (t^* - t)^{2/5}$ for $t \longrightarrow t^*$]. Infinite velocity at the collapse time and large increments of local pressures are among causes of cavitation [13]. Similarity between the behavior of solutions in the viscous case for large Reynolds numbers and the behavior for an ideal liquid is corroborated by the regularity of the perturbation of Eqs. (10) and (12) by the parameter $1/\mathrm{Re}$ for $\mathrm{Re} \gg 1$. In regime B for $\mathrm{Re} \lesssim 8.4$, filling occurs exponentially in infinite time, the cumulation of energy is completely eliminated due to viscosity, and $Q \sim -R$ for $R \to 0$ ($R \sim \exp(-t)$ for $t \longrightarrow \infty$]. These two regimes

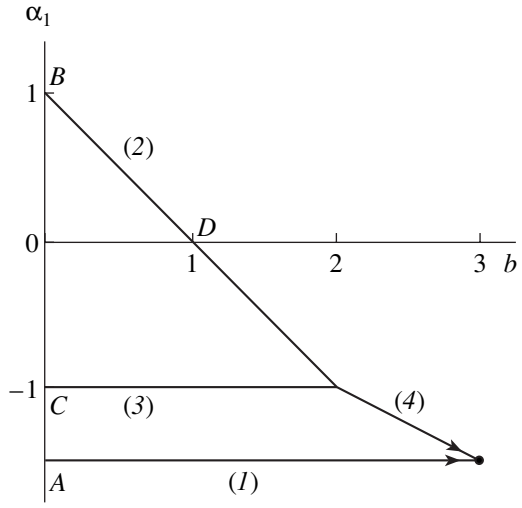

Figure.

is separated by regime C for Re ≈ 8.4, in which filling occurs in a finite time, but $Q \sim -\frac{1}{R}$ for $R \longrightarrow 0$ ($R \sim \sqrt{t^* - t}$ for $t \longrightarrow t^*$).

For an ideal viscous medium, Eq. (12) has no integrals similar to Eq. (14). The plots of $Q(R)$ and $R(t)$ for viscous and viscoplastic media can be drawn numerically. We seek power asymptotic formulas for solutions of the problem given by Eqs. (12) and (13) near the point $R = 0$ by taking, for definiteness, $\tau(r) = \frac{\tau}{r^\beta}$, $\beta > 0$ in Eq. (11), i.e.,

$$T(R) = \frac{2\sqrt{3}\tau}{\beta R^\beta}. \tag{15}$$

Let

$$Q(R) = q_1 R^{\alpha_1} + q_2 R^{\alpha_2} + \ldots, \quad \alpha_1 < \alpha_2 < \ldots. \tag{16}$$

Substituting Eq. (14) into Eqs. (12) and making some transformations, we obtain

$$\left(\alpha_1 + \frac{3}{2}\right) q_1^2 R^{2\alpha_1} + (\alpha_1 + \alpha_2 + 3) q_1 q_2 R^{\alpha_1 + \alpha_2} + \ldots$$

$$= -\frac{4}{\mathrm{Re}}(q_1 R^{\alpha_1 - 1} + q_2 R^{\alpha_2 - 1} + \ldots) + \frac{2\sqrt{3}\tau}{\beta R^\beta} + \frac{c}{R^{3\gamma}} - 1. \tag{17}$$

We denote $b = \max\{\beta, 3\gamma\} > 0$. For compensation of low powers of R in each of the series entering into Eq. (17), the leading term of asymptotic formula (16) can be taken several ways for various b (Fig. 1):

(i) $0 < b \le 2$, $\alpha_1^{(1)} = -\frac{3}{2}$, $\alpha_1^{(2)} = 1 - b$, $\alpha_1^{(3)} = -1$;

(ii) $2 < b < 3$, $\alpha_1^{(1)} = -\frac{3}{2}$, $\alpha_1^{(4)} = -\frac{b}{2}$; and

(iii) $b \ge 3$, in this case, the bubble does not collapse and power expansion (16) is invalid.

Points A, B, and C in Fig. 1 correspond to the three respective asymptotic regimes in the Zababakhin problem. The velocity at the collapse time is equal to zero in interval BD, to a negative constant at point D, and to minus infinity at all other points of branches (1)–(4). As in the Zababakhin problem, branch (1) is realized for Re values larger than a certain critical value and branches (2) and (4) are realized for Re values lower than this critical value.

3. We note that, if $v_0 = 0$ and $c = 1 \pm T(1)$, rest $R(t) \equiv 1$ is a solution of the problem given by Eqs. (10) and (16). Motion is absent in the range $1 - T(1) < c < 1 + T(1)$, because the pressure drop between infinity and inside the bubble is insufficient for the beginning of deformation. The beginning of deformation and motion toward and out from the center occur when $c < 1 - T(1)$ and $c > 1 + T(1)$, respectively. We analyze the behavior of the system near the rest state in two cases, taking first v_0 and then $c - 1 \mp T(1)$ as asymptotically small parameters.

Let $0 < \varepsilon_1 = v_0 \ll 1$, $c = 1 + T(1)$. Then, the bubble begins to expand immediately for $t > 0$, and $\mathrm{sgn}\dot{R} = 1$ should be taken in Eq. (10):

$$R\ddot{R} + \frac{3}{2}\dot{R}^2 = -\frac{4\dot{R}}{R\mathrm{Re}} - T(R) + \frac{1 + T(1)}{R^{3\gamma}} - 1, \tag{18}$$

$$\dot{R} > 0,$$

$$R(0) = 1, \quad \dot{R}(0) = \varepsilon_1. \tag{19}$$

Seeking a solution of the problem given by Eqs. (18) and (19) in the form of the power series in ε_1:

$$R(t) = 1 + \varepsilon_1 R_1(t) + \varepsilon_1^2 R_2(t) + \ldots \tag{20}$$

we arrive at the following linear problem with constant coefficients for function $R_1(t)$:

$$\ddot{R}_1 + \frac{4}{\mathrm{Re}}\dot{R}_1 + BR_1 = 0, \quad \dot{R}_1 > 0, \tag{21}$$

$$R_1(0) = 0, \quad \dot{R}_1(0) = 1, \tag{22}$$

where $B = T'(1) + 3\gamma(1 + T(1))$. For example,

$$B = 3\gamma\left(1 + \frac{2\sqrt{3}\tau}{\beta}\right) - 2\sqrt{3}\tau$$

for Eq. (15); i.e., coefficient B can be both positive and negative.

We indicate five possible ranges with qualitatively different behaviors of the system.

(i) $B < 0$. The solution

$$R_1 = \frac{e^{\lambda_1 t} - e^{\lambda_2 t}}{\lambda_1 - \lambda_2}, \quad \lambda_{1,2} = -\frac{2}{\mathrm{Re}} \pm \sqrt{\frac{4}{\mathrm{Re}^2} - B}, \quad (23)$$

of the problem given by Eqs. (21) and (22) increases monotonically and unboundedly for $t \longrightarrow \infty$, because $\lambda_1 > 0$. This means that a small initial-velocity perturbation of the equilibrium position $R \equiv 1$ leads to finite deviation from this position; i.e., this equilibrium position is unstable. Asymptotic formula (20) is valid only for a finite time interval.

(ii) $B = 0$. In this case, $\lambda_1 = 0$ and $\lambda_2 = -\frac{4}{\mathrm{Re}}$. Therefore,

$$R_1(t) = \frac{\mathrm{Re}}{4}(1 - e^{-4t/\mathrm{Re}}). \quad (24)$$

This solution is valid in the entire time interval, because $\dot{R}_1 > 0$. Moreover, $\lim_{t \to \infty} R(t) = 1 + \frac{\varepsilon_1 \mathrm{Re}}{4} + O(\varepsilon_1^2)$.

(iii) $0 < B < \frac{4}{\mathrm{Re}^2}$. Solution (23) exists from $t = 0$ only to

$$t_* = \frac{1}{\lambda_1 - \lambda_2} \ln \frac{\lambda_2}{\lambda_1}, \quad (25)$$

when $\dot{R}_1(t_*) = 0$. Reaching radius $R_* = R(t_*) = 1 - \frac{\varepsilon_1 e^{\lambda_1 t_*}}{\lambda_2} + O(\varepsilon_1^2)$ to $t = t_* = 0$, the bubble ceases to change.

(iv) $B = \frac{4}{\mathrm{Re}^2}$. In this case,

$$R_1(t) = te^{-2t/\mathrm{Re}}, \quad t_* = \frac{\mathrm{Re}}{2}, \quad R_1(t_*) = \frac{\mathrm{Re}}{2e}. \quad (26)$$

(v) $B > \frac{4}{\mathrm{Re}^2}$. In this case,

$$R_1(t) = \frac{1}{\lambda} e^{-2t/\mathrm{Re}} \sin(\lambda t), \quad \lambda = \sqrt{B - \frac{4}{\mathrm{Re}^2}}, \quad t_* = \frac{1}{\lambda} \arctan \frac{\lambda \mathrm{Re}}{2}. \quad (27)$$

Asymptotic formulas for the case $v_0 < 0$, $|v_0| \ll 1$, and $c = 1 - T(1) > 0$ are derived similarly. One should take $\mathrm{sgn}\dot{R} = -1$ in Eq. (10) in this case.

We briefly discuss the other asymptotic case, $v_0 = 0$, $0 < \varepsilon_2 = c - 1 - T(1) \ll 1$; i.e., the bubble expands ($\mathrm{sgn}\dot{R} = 1$) for times close to the initial time. Seeking a solution of the Cauchy problem

$$R\ddot{R} + \frac{3}{2}\dot{R}^2 = -\frac{4\dot{R}}{R\mathrm{Re}} - T(R) + \frac{1 + T(1) + \varepsilon_2}{R^{3\gamma}} - 1, \quad \dot{R} > 0, \quad (28)$$

$$R(0) = 1, \quad \dot{R}(0) = 0, \quad (29)$$

which follows from Eqs. (10) and (6), in the form of series (20), we arrive at the following problem, which is similar to the problem given by Eqs. (21) and (22):

$$\ddot{R}_1 + \frac{4}{\mathrm{Re}}\dot{R}_1 + BR_1 = 1, \quad \dot{R}_1 > 0, \quad (30)$$

$$R_1(0) = 0, \quad \dot{R}_1(0) = 0. \quad (31)$$

For this problem, one can analyze the above five cases for parameter B and represent the corresponding solutions of the linear problem given by Eqs. (30) and (31) in the explicit form.

Thus, it has been shown that the number and form of asymptotic expansions for both the time of the beginning of the bubble deformation and the time of its collapse depend significantly on dimensionless parameters of the medium Re, $\tau(r)$, filling gas c, and initial velocity v_0. Qualitatively different expansions correspond to different behaviors upon collapse (cavitation collapse or slow filling in infinite time) and the beginning of deformation (instability of the initial position, monotonic motion over an infinite time interval, and motion over a finite time interval up to complete stop of motion).

ACKNOWLEDGMENTS

This work was supported by the Russian Foundation for Basic Research, project nos. 02-01-00780 and 02-01-00567.

REFERENCES

1. H. Lamb, *Lehrbuch der Hydrodynamik* (Teubner, Leipzig, 1931).
2. H. Poritsky, in *Proceedings of the 1st US National Congress on Applied Mechanics* (Ann Arbor. Mich., 1951), pp. 812–821.

3. E. I. Zababakhin, Prikl. Mat. Mekh. **24**, 1129 (1960).
4. R. D. Ivany and F. G. Hammitt, ASME J. Basic Eng. **87**, 977 (1965).
5. A. Prosperetti, J. Fluid Mech. **100** (2), 333 (1980).
6. V. G. Grigor'ev, S. Z. Dunin, and V. V. Surkov, Izv. Akad. Nauk SSSR, Mekh. Tverd. Tela, No. 1, 199 (1981).
7. G. Ryskin, J. Fluid Mech. **218**, 239 (1990).
8. M. A. Brutyan and P. L. Krapivskiĭ, Itogi Nauki Tekh., Ser. Kompl. Spets. Razd. Mekh. **4**, 3 (1991).
9. D. V. Georgievskiĭ, Izv. Akad. Nauk, Ser. Mekh. Zhidk. Gaza, No. 2, 181 (1994).
10. E. H. Trinh, D. B. Thiessen, and R. G. Holt, J. Fluid Mech. **364**, 253 (1998).
11. A. A. Aganin, R. I. Nigmatulin, M. A. Il'gamov, and I. Sh. Akhatov, Dokl. Akad. Nauk **369** (2), 182 (1999) [Dokl. Phys. **44**, 734 (1999)].
12. R. I. Nigmatulin, I. Sh. Akhatov, N. K. Vakhitova, and R. T. Lahey, J. Fluid Mech. **414**, 47 (2000).
13. R. T. Knapp, J. W. Daily, and F. G. Hammitt, *Cavitation* (McGraw-Hill, New York, 1970; Mir, Moscow, 1974).

Translated by R. Tyapaev

Doklady Physics, Vol. 49, No. 11, 2004, pp. 673–679. From Doklady Akademii Nauk, Vol. 399, No. 2, 2004, pp. 192–198.

MECHANICS

Exact Solutions to the Principal Variational Inverse Boundary Value Problem of Aerohydrodynamics[1]

A. M. Elizarov and D. A. Fokin

Presented by Academician G.G. Chernyĭ April 29, 2004

Received April 29, 2004

INTRODUCTION

The problems discussed in this paper are related to a general question of aerohydrodynamics, which can be formulated in the following manner: what maximum lift can be attained by an isolated airfoil, and what should be the shape of the airfoil? The exact solution to the lift-optimization problem for an infinitely thin airfoil with a given length and limited curvature for a flow of an ideal incompressible fluid (IIF) is obtained in [1]. It is proved that the extremal airfoil shape is a circular segment. A review of methods and results related to the design of high-lift airfoils is available in [2]. A numerical approach to lift maximization for airfoils with sharp trailing edge and a specified contour perimeter under the condition of flow continuity is proposed in [3]. It is stated (without proof) that, for a smooth airfoil contour, the maximum lift is attained for a circle. A particular case of this is proved in [4]. Under additional conditions (e.g., the condition of viscous flow continuity on the airfoil contour, the allowance for flow compressibility, etc.), the optimized solutions significantly differ from a circle and the airfoil shape can be obtained only by numerical calculation (see, e.g., [5–7]). Nevertheless, the circle is an extremal analytical solution obtained under a minimum number of constraints stipulated by a mathematical flow model. Correspondingly, this solution yields the exact upper estimate of the maximum lift coefficient for the model based on an IIF.

The problems investigated in [4–7] (see also [8]) relate to the class of variational inverse boundary value problems of aerohydrodynamics (IBVPA). Formulations and methods of solving these types of problems in the framework of the classical models of fluid mechanics and gas mechanics under isoperimetric constraints are discussed in [9]. There are also estimates of the maximum lift coefficient for the class of airfoils with smooth closed contours in continuous of IIF flows without separation. Special cases are distinguished when the extremal solution is a circle or not a circle. Realization of the exact solution of the lift-maximization problem in the case when the optimal solution is not a circle remains still opened. The present study is an attempt to answer this question.

PRINCIPAL VARIATIONAL IBVPA

Among the possible formulations of the variational IBVPA, we distinguish a problem with a solution that directly answers the question formulated in the Introduction. The exact solution to this problem obtained in the framework of the IIF model yields an extremal value of the lift coefficient and its upper estimate, provided that additional conditions are taken into account. This is why we call this problem the principal problem. We now formulate it for the case of an IIF.

PHYSICAL FORMULATION OF THE PROBLEM

We consider a steady-state IIF flow without separation around an isolated impermeable airfoil in the physical plane $z = x + iy$. The contour of the airfoil is smooth everywhere except the sharp trailing edge B ($z = 0$) (Fig. 1) with the external angle $\varepsilon\pi$ ($1 \le \varepsilon \le 2$). In particular, for $\varepsilon = 1$, the contour has a perimeter of $l = 2$ and it is smooth everywhere. The flow at infinity is uniform and directed horizontally, the flow velocity and incom-

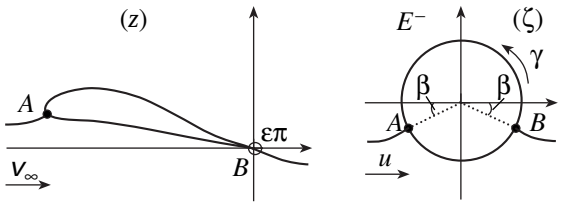

Fig. 1. Class of optimized contours.

[1] This article was submitted by the authors in English.

Chebotarev Institute of Mathematics and Mechanics, Kazan State University, Kazan, Russia
e-mail: elizarov@ksu.ru, dfokin@ksu.ru

1028-3358/04/4911-0673$26.00 © 2004 MAIK “Nauka/Interperiodica”

pressible-fluid density being $v_\infty = 1$ and $\rho = 1$, respectively. The trailing point corresponds to $z = 0$ (for $\varepsilon \neq 1$, in accordance with Zhukovskiĭ's hypothesis, this is the sharp edge B). As a reference length, we choose the contour semiperimeter (for actual airfoils, it does not differ too much from the airfoil's chord length). It is required to determine the airfoil shape that provides the maximum lift coefficient C_y under the condition that the maximum velocity on the contour does not exceed a given value $v_{\max}$, $v_{\max} > 1$.

THE MATHEMATICAL MODEL AND THE CLASS OF CONTOURS BEING OPTIMIZED

Following [9], we write out the basic equation corresponding to the mathematical model that describes the problem.

The flow around an airfoil in a physical plane is completely determined by the following pair of quantities: (*1*) 2π-periodic function $P(\gamma) \in L_2[0, 2\pi]$($L_2[0, 2\pi]$ is the space of functions (the function squared is integrable within the segment $[0, 2\pi]$)) that satisfy certain additional conditions discussed below, and (*2*) the parameter $\beta \in \left[-\frac{\pi}{2}, \frac{\pi}{2}\right]$ (so-called theoretical angle of attack). We determine a domain $E^- = \{\zeta: |\zeta| > 1\}$ in an auxiliary plane ζ (Fig. 1) and consider an IIF flow around a unit circle with flow velocity u directed horizontally. Critical points $B = e^{-i\beta}$ and $A = -e^{i\beta}$ of the flow (at which the flow velocity is zero) are symmetric with respect to the vertical axis.

We specify a class of closed, piecewise smooth, and impermeable contours **L** with a fixed perimeter $l = 2$ (Fig. 1) and, possibly, one sharp edge B with the external angle $\varepsilon\pi$ as a set of images of a unit circle at conformal mappings $z = z_P(\zeta)$, $\zeta \in E^-$. The mappings are normalized in accordance with the conditions $z_P(\infty) = \infty$, $z_P(e^{-i\beta}) = 0$ and are determined by the control function $P(\gamma)$, $\gamma \in [0, 2\pi]$ and by the theoretical angle of attack $\beta \in \left[0, \frac{\pi}{2}\right]$. The ideal incompressible fluid flows around the airfoil contour at a velocity v_∞ directed horizontally.

Then, the following representation is valid:

$$z_P'(\zeta) = u\exp[-\chi(\zeta)]\left(1 - \frac{e^{-i\beta}}{\zeta}\right)^{\varepsilon - 1}. \qquad (1)$$

Moreover, by virtue of the normalization of the mapping function and closure of the contours, the equalities

$$A_0(P) \equiv \int_0^{2\pi} P(\tau)d\tau = B_0, \quad B_0 = 0, \qquad (2)$$

$$A_1(P) + iA_2(P) \equiv \int_0^{2\pi} P(\tau)e^{i\tau}d\tau = B_1 + iB_2,$$
$$B_1 + iB_2 = -\pi(\varepsilon - 1)\exp(-i\beta) \qquad (3)$$

hold.

The coordinates x, y of the airfoil contour are determined from (1) in the parametric form $x(\gamma) + iy(\gamma) = z_P(e^{i\gamma})$ as a function of the parameter $\gamma \in [0, 2\pi]$:

$$z_P(e^{i\gamma}) = u\int_{-\beta}^{\gamma}\left|2\sin\frac{\tau + \beta}{2}\right|^{\varepsilon - 1}$$
$$\times \exp\left\{P(\tau) + i\left[Q(\tau) + (\varepsilon - 1)\frac{\tau + \beta + \pi}{2}\right]\right\}d\tau.$$

Here, the singular integral is

$$Q(\gamma) = -\frac{1}{2\pi}\int_0^{2\pi} P(\tau)\cot\frac{\tau - \gamma}{2}d\tau.$$

To provide the existence of this integral, we require that the function $P(\gamma)$ be a Hölder continuous function with fixed coefficient and exponent. These functions form a compact set U in the $L_2[0, 2\pi]$ space.

Finally, the class **L** of the contours under consideration is determined by the conformal mappings $z = z_P(\zeta)$, obtained from (1), where the control function $P(\gamma)$ satisfies the conditions described above, including additional conditions (2) and (3).

The distribution of the flow velocity over the airfoil contour can be presented in the parametric form

$$v(\gamma) = 2\cos\frac{\gamma - \beta}{2}\left|2\sin\frac{\gamma + \beta}{2}\right|^{2 - \varepsilon}\exp P(\gamma).$$

For convenience, we take these value as being positive and negative on the upper $\gamma \in [-\beta, \pi + \beta]$ and lower $\gamma \in [\pi + \beta, 2\pi - \beta]$ airfoil surfaces, respectively. The limitation of the maximum velocity on the airfoil contour by a given value $v_{\max}$ is expressed with the aid of a control function $P(\gamma)$ and of the parameter β in the form

$$P(\gamma) \le H_0(\gamma, \beta) \equiv \ln\left[\frac{v_{\max}}{M(\gamma, \beta)}\right]$$
$$+ (\varepsilon - 1)\ln\left|2\sin\frac{\gamma + \beta}{2}\right|, \qquad (4)$$
$$M(\gamma, \beta) = |2(\sin\gamma + \sin\beta)|.$$

In this case,

$$C_y = \frac{16\pi\sin\beta}{I_0(P)}, \quad u = \frac{2}{I_0(P)},$$
$$I_0(P) = \int_0^{2\pi} e^{-P(\tau)}\left|2\sin\frac{\tau+\beta}{2}\right|^{\varepsilon-1} d\tau. \tag{5}$$

Thus, the maximization of the lift coefficient C_y corresponds to the minimization of the functional $J_0(P, \beta) = I_0(P)\operatorname{cosec}\beta$ under constraints (2)–(4).

THE EXISTENCE AND UNIQUENESS OF THE SOLUTION

The following theorems are valid.

Theorem 1 [9]. *Let C_y^* and β^* be correspondingly the absolute maximum of C_y and extremal value of β; $v_{\max}^* = \exp(\sin\beta)$, $v_{\max}^{**} = 2(1+\sin\beta)$. Then, the principal variational IBVPA has a solution and $\sin\beta^* < \ln v_{\max}$, $C_y^* < 2\ln v_{\max}$. In addition,*

(1) for $v_{\max} \geq 4$, the only extremal solution is a circle and $C_y^* = 8$, $\beta^* = \frac{\pi}{2}$;

(2) for $1 < v_{\max} < 4$, the extremal solution is not a circle and $C_y^* \geq v_{\max} - 2$ and $\beta^* \geq \arcsin\left(\frac{v_{\max}}{2} - 1\right)$ for $2 < v_{\max} \leq 4$; and

(3) for a given value $\beta = \beta_0$, the inequality $v_{\max} \geq v_{\max}^*$ is the necessary condition of solvability. Moreover, if $v_{\max} \geq v_{\max}^{**}$, then the circle is again the only extremal solution. If $v_{\max}^* \leq v_{\max} < v_{\max}^{**}$, then the extremal solution is not a circle.

Note that, if the value of $\beta = \beta_0$ is given, then we have principal variational IBVPA with an additional constraint. The latter statement is equivalent to finding a 2π-periodic Hölder continuous function $P(\gamma)$ that satisfies conditions (2)–(4), which provides the minimum of the functional $I_0(P)$ for a given $\beta = \beta_0$.

The following theorem is also valid.

Theorem 2. *If the subset $U_0 \subset U$ of the Hölder continuous functions $P(\gamma)$ satisfying conditions* (2)–(4) *is not empty and $\sin\beta_0 < \ln v_{\max}$, then, for $\beta = \beta_0$, the principal variational IBVPA has a unique solution.*

The validity of Theorem 2 is proved by the strict convexity of functional (5) in Theorem 1, by the compactness of the set U_0 (if it is not empty) in the space $L_2[0, 2\pi]$, and by the linearity of constraints (2)–(4).

THE EXACT SOLUTION TO THE PROBLEM

The form of the extremal function $P^*(\gamma)$ is given by the Kuhn–Tucker theorem (see, e.g., [10, Sect. 1.1.2]). We now construct the extended functional.

$$\Psi(P) = \int_0^{2\pi} F(P, \tau)d\tau \equiv I_0(P) + \mu_0[A_0(P) - B_0]$$
$$+ \mu_1[A_1(P) - B_1] + \mu_2[A_2(P) - B_2]$$
$$+ \int_0^{2\pi} \mu(\tau)[P(\tau) - H_0(\tau, \beta)]d\tau.$$

The parameters μ_0, μ_1, and μ_2 should be chosen in such a manner that conditions (2) and (3) will be fulfilled. The quantity $\mu(\gamma)$ is a nonnegative function (Kuhn–Tucker multiplier) that allows condition (4) to be satisfied. By virtue of the necessary extremum condition, the function $P^*(\gamma)$ is determined from the equation $\frac{\partial F}{\partial P} = 0$:

$$P^*(\gamma) = (\varepsilon - 1)\ln\left|2\sin\frac{\gamma+\beta}{2}\right| - \ln g(\mu_0, \mu_1, \mu_2, \mu, \gamma), \tag{6}$$
$$g(\mu_0, \mu_1, \mu_2, \mu, \gamma) \equiv \mu_0 + \mu_1\cos\gamma + \mu_2\sin\gamma + \mu(\gamma).$$

The parameters μ_0, μ_1, μ_2 and function $\mu(\gamma)$ are chosen in a manner such that $g(\mu_0, \mu_1, \mu_2, \mu; \gamma) \geq 0$. In accordance with the Kuhn–Tucker method, the function $\mu(\gamma) \geq 0$ should be found from the condition of the so-called complementary stackness. As a result, we arrive at

$$\mu = \mu^*(\gamma) = \max\{0, v_{\max}^{-1}M(\gamma, \beta) - \mu_0 - \mu_1\cos\gamma - \mu_2\sin\gamma\}.$$

The velocity distribution that corresponds to $P^*(\gamma)$ is found as

$$|v^*(\gamma)| = \min\left\{v_{\max}; \left|\frac{M(\gamma, \beta)}{\mu_0 + \mu_1\cos\gamma + \mu_2\sin\gamma}\right|\right\}. \tag{7}$$

The minimal value of the functional is

$$I^* = I_0(P^*) = 2\pi\mu_0 + \int_0^{2\pi} \mu^*(\tau)d\tau > 0.$$

We rewrite conditions (2) and (3) for the extremal

function $P^*(\gamma)$ in the form

$$\int_0^{2\pi} \ln g(\mu_0, \mu_1, \mu_2, \mu^*; \gamma) d\gamma = 0, \tag{8}$$

$$\begin{aligned} &\int_0^{2\pi} \ln g(\mu_0, \mu_1, \mu_2, \mu^*; \gamma) \cos\gamma d\gamma = 0, \\ &\int_0^{2\pi} \ln g(\mu_0, \mu_1, \mu_2, \mu^*; \gamma) \sin\gamma d\gamma = 0. \end{aligned} \tag{9}$$

The value I^*, the functions $\mu^*(\gamma)$, $v^*(\gamma)$, and Eqs. (8) and (9) do not contain the quantity ε that determines the profile opening angle in the airfoil trailing edge. Hence, the extremal solution obtained is the same for all airfoils with a sharp ($\varepsilon > 1$) and smooth ($\varepsilon = 1$) trailing edges. From (6), it follows that, in the first case, the function $P^*(\gamma)$ has a singularity at $\gamma = -\beta$. This implies that the solution obtained does not belong to the chosen class of functions and yields only the upper estimate of the maximal lift coefficient. For the smooth trailing edge, it is possible to construct an airfoil for which the maximum is attained.

SYMMETRY OF THE OPTIMUM SOLUTION AND MONOTONICITY OF THE CORRESPONDING VELOCITY DISTRIBUTION

First, we prove that, from the uniqueness of the solution to the problem under study, (see Theorem 2) it follows $\mu_1 = 0$.

Suppose that we have managed to find a set of parameters μ_0, $\mu_1 > 0$, μ_2, which satisfy conditions (8) and (9), and to construct both the corresponding function $\mu^*(\gamma)$ and the velocity distribution $v^*(\gamma)$. Replacing the variables $\tau = \pi - \gamma$ in (8) and (9), we can see that the solvability conditions are also satisfied for the new set of the parameters μ_0, $-\mu_1 < 0$, μ_2 and for the new function

$$\begin{aligned} \mu_1(\gamma) = \mu^*(\pi - \gamma) = \max\{0, v_{\max}^{-1} M(\gamma, \beta) \\ - \mu_0 + \mu_1 \cos\gamma - \mu_2 \sin\gamma\}. \end{aligned}$$

Furthermore, the velocity $v_1^*(\gamma)$ that corresponds to the new set of parameters satisfies the condition of limitation of the maximal velocity. Finally, substituting μ_0, $-\mu_1$, μ_2 and corresponding function $\mu_1(\gamma)$ into the necessary extremum condition, we find that this set of parameters provides the global minimum of the functional I_0. Thus, the set of parameters μ_0, $-\mu_1 < 0$, μ_2 is also a solution of the extremal problem under consideration, which contradicts the uniqueness of the solution. Therefore, $\mu_1 = 0$. This also implies that $\mu^*(\gamma) = \mu^*(\pi - \gamma)$, and it is sufficient to consider the interval $\gamma \in \left[-\frac{\pi}{2}, \frac{\pi}{2}\right]$. For the rest of the circle, the solution can be obtained from symmetry considerations. The other important consequence of symmetry is that the first condition in (9) is fulfilled automatically. Note that, for $\varepsilon = 1$, the equation $\mu_1 = 0$ provides symmetry of the corresponding contour with respect to the vertical axis and the monotonic increase in the velocity distribution $v^*(\gamma)$ [see (7)] within the interval $\gamma \in \left[-\frac{\pi}{2}, \frac{\pi}{2}\right]$. In this case, if $2(1 + \sin\beta) > v_{\max}(\mu_0 + \mu_2)$, then, for $\left[t, \frac{\pi}{2}\right]$, $t = \arcsin\left(\frac{\mu_0 v_{\max} - 2\sin\beta}{2 - \mu_2 v_{\max}}\right)$, we have a "roof-top" velocity distribution $v = v_{\max}$.

Numerical experiments have shown that, for optimal airfoils corresponding to velocity distributions (7) at $\beta > 0$, the simultaneous presence of the velocity "roof tops" on the lower and upper airfoil surfaces is not possible. However, this requires an exact proof, which has not been obtained so far. If this hypothesis is correct, then we always have

$$v^*(\gamma) = v_1^*(\gamma) \equiv \frac{2(\sin\gamma + \sin\beta)}{\mu_0 + \mu_2 \sin\gamma},$$

$$\gamma \in \left[-\frac{\pi}{2}, t\right], \; v^*(\gamma) = v_2^*(\gamma) \equiv v_{\max}, \; \gamma \in \left[t, \frac{\pi}{2}\right],$$

where $t = \frac{\pi}{2}$ for $2(1 + \sin\beta) < v_{\max}(\mu_0 + \mu_2)$. Thus, the set of nonlinear equations for seeking two unknown parameters μ_0 and μ_2 with allowance made for symmetry of the optimal-velocity distribution takes the form

$$\begin{aligned} &\int_{-\pi/2}^{\pi/2} \ln|v^*(\gamma)| d\gamma = 0, \\ &\int_{-\pi/2}^{\pi/2} \ln|v^*(\gamma)| \sin\gamma d\gamma = \pi \sin\beta. \end{aligned} \tag{10}$$

If constraint (4) is ignored, then $\mu(\gamma) \equiv 0$, and $\mu_2 = 0$, $\mu_0 = 1$ is the solution of set (10). Then, $g(\mu_0, \mu_1, \mu_2, \mu^*; \gamma) \equiv 1$, $P^*(\gamma) = (\varepsilon - 1)\ln\left|2\sin\frac{\gamma + \beta}{2}\right|$, $I^* = 2\pi$, and the optimal solution is again a circle determined by a conformal mapping $z_{P^*}(\gamma) = \frac{\zeta + i}{\pi}$ (cf. [4]).

ON SOLVABILITY OF THE SET OF EQUATIONS (10)

We now schematically describe the proof of the solvability of set (10).

It is rigorously proved that the case $\mu_2 = 0$ is possible only if $v_{max} = 2(1 + \sin\beta)$. This optimal solution is again a circle (see Theorem 1). We consider the case $\mu_2 \neq 0$ and denote $q = \mu_2 \frac{v_{max}}{2}$, $m = \frac{\mu_0}{\mu_2}$. Thus,

$$F_1(t, m) = \int_t^{\pi/2} \ln\left|\frac{\sin\gamma + m}{\sin\gamma + \sin\beta}\right| d\gamma,$$

$$F_2(t, m) = \int_t^{\pi/2} \ln\left|\frac{\sin\gamma + m}{\sin\gamma + \sin\beta}\right| \sin\gamma d\gamma,$$

where $m > -\sin t \le -\sin\beta$. We assume that the "roof-top" velocity distribution can exist only for the upper surface of the optimized airfoil. Then, we have an explicit representation of q in terms of t and m:

$$|q| = \exp\left[\frac{F_1(t, m) + \pi \ln v_{max}}{\pi/2 + t}\right], \quad (11)$$

and the equation for finding m at a given t is

$$\pi m = \Phi_0(t, m),$$

$$\Phi_0(t, m) \equiv \left(\frac{\pi}{2} + t\right)^{-1} \quad (12)$$

$$\times \cos t[F_1(t, m) + \pi \ln v_{max}] + F_2(t, m).$$

Theorem 3. *Let $t \ge 0$. If $\Phi_0(t, -\sin t) < -\pi \sin t$, then, for an arbitrary t,* Eq. (12) *has no more than two roots. If*

$$\Phi_0(t, -\sin t) \ge -\pi \sin t, \quad (13)$$

then Eq. (12) *has a unique solution.*

Numerical calculations have shown that, for arbitrary t (not only positive), inequality (13) holds and solution $m^* = m^*(t)$ to Eq. (12) is unique and continuously depends on t. From (11), we determine $q = q^*(t)$ as a function of t and obtain the equation for finding t:

$$\sin t = R(t), \quad R(t) \equiv \frac{q^*(t)m^*(t) - \sin\beta}{1 - q^*(t)}. \quad (14)$$

Equation (14) can be solved numerically. Calculations have shown that the equation can be resolved uniquely. Now, when all the parameters are known, it is possible to find the shapes of the optimal airfoils.

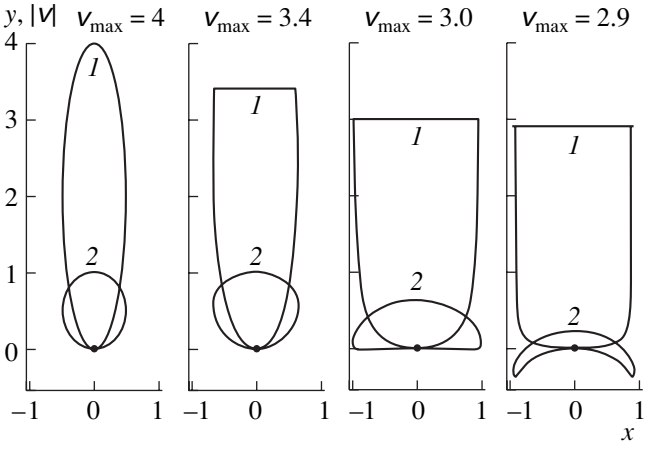

Fig. 2. Exact solutions for $\varepsilon = 1$, $\beta = 90°$, and different v_{max}.

Figure 2 shows the exact shapes of the optimal airfoils and corresponding velocity distributions at $\beta = 90°$ and different v_{max}. In this case, $v_{max} = 1.15$, $v^{**}_{max} = 2.28$. In Figs. 3, 4, the corresponding contours are marked by number 2, and corresponding chord diagrams—by number 1. Small black circles on the contours indicate the branching and trailing points (in the given case, these points coincide). As is seen, the exact solutions have only the vertical symmetry axis. Other characteristics of the optimal solutions are presented in the left part of Table 1.

By virtue of Theorem 1 for a given value $\beta = \beta_0$, the problem has a unique "noncircular" extremal solution only if $v^*_{max} \le v_{max} < v^{**}_{max}$ (for $v_{max} > v^{**}_{max}$, the extremum is again a circle). For a given v_{max}, the unique

Table 1. Characteristics of exact solutions in the case of $\varepsilon = 1$: for $\beta_0 = 90°$ and different v_{max}, for $v_{max} = 1.4$ and different $\beta = \beta_0$, and for $\beta_0 = 8°$ and different v_{max}

$\beta_0 = 90°$			$v_{max} = 1.4$			$\beta = 8°$		
v_{max}	t_{max}	C_v	β	t_{max}	C_v	v_{max}	t_{max}	C_v
4	1.0	8.0	8°	0.2717	1.0025	1.3	0.0903	0.9358
3.4	1.0	7.9528	10°	0.1456	1.2062	1.5	0.3565	1.0478
3.0	0.6317	7.3921	14°	0.008	1.5086	1.8	0.728	1.1036
2.9	0.2176	6.6228				2.28	1.0	1.1134

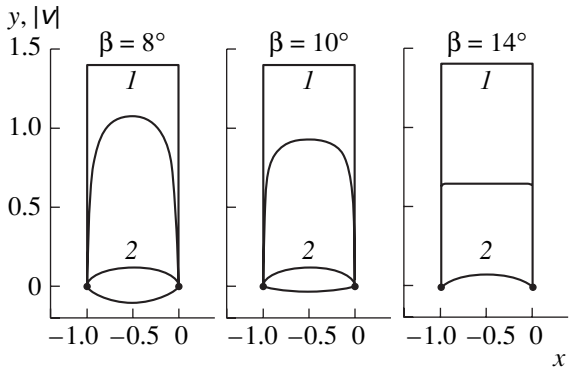

Fig. 3. Exact solutions for $\varepsilon = 1$, $v_{max} = 1.4$, and different $\beta = \beta_0$.

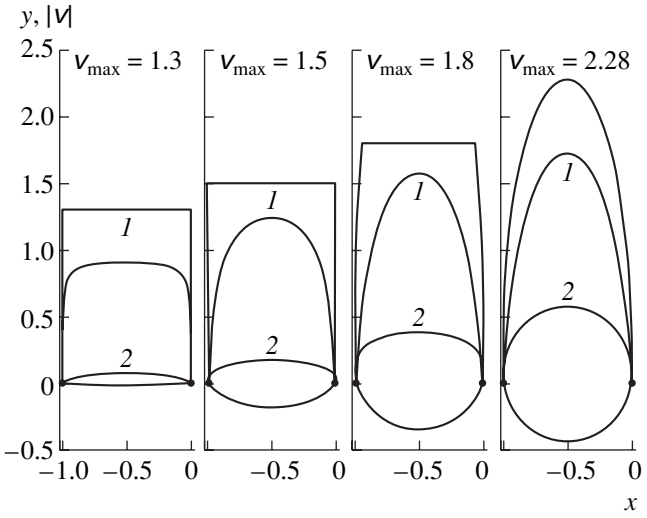

Fig. 4. Exact solutions for $\varepsilon = 1$, $\beta_0 = 8°$, and different v_{max}.

noncircular solution is provided if $\beta \le \beta_{max} = \arcsin(\ln v_{max})$. Thus, there exists an admissible region of the parameter variation, which corresponds to "noncircular" solutions. This region is bounded from above and from below by the curves $v_{max} = 2(1 + \sin\beta)$ and $v_{max} = \exp(\sin\beta)$, respectively. Figures 3 and 4 and Tables 1 and 2 demonstrate the tendencies of variation of the optimal shapes and characteristics for these two cases. Note that $v^*_{max} = e$ for $\beta = \frac{\pi}{2}$. Therefore, the last example presented in Fig. 2 is the ultimate case.

Table 2. Characteristics of optimized numerical solutions (for $\varepsilon = 2$), exact analytical solutions (for $\varepsilon = 1$), and for $v_{max} = 1.8$ and different β

β	ε = 2		ε = 1	
	t_{max}	C_y	t_{max}	C_y
8°	0.6752	1.0874	0.7279	1.1043
10°	0.6231	1.3507	0.6633	1.3715
15°	0.4501	1.9728	0.4884	2.0029
20°	0.2817	2.4882	0.302	2.535

Figure 3 and the middle part of Table 1 show exact solutions for $\varepsilon = 1$, $v_{max} = 1.4$, and different $\beta = \beta_0$. We see that, as the value of β increases, the airfoil thickness decreases and approaches a circular arc (e.g., $\beta = 14°$). A further increase in β results in a multivalent solution (self-crossing contours). Note that, in the given case, $\beta_{max} = 19.65°$.

Figure 4 and the right-hand side of Table 1 demonstrate the exact solutions for $\beta = 8°$, $\varepsilon = 1$, and different values of v_{max}. For the given case, $v^*_{max} = 1.15$, $v^{**}_{max} = 2.28$.

In addition, numerical optimization was also performed for several values of v_{max} in the N-parametric class of functions

$$P_N(\gamma) = \sum_{k=2}^{N+1} (a_k \cos k\gamma + b_k \sin k\gamma).$$

In this case, the coefficients a_k and b_k were varied with conditions (2)–(4) taken into account in order to obtain an airfoil with a maximum lift. Dependences of the maximum value of C_{ymax} on v_{max} for several β_0 were obtained. It has been found that, for decreasing values of v_{max}, the values of $C_{y\,max}$ also decrease. In addition, according to Theorem 1, for each value of β_0, there exists a minimal value $v^*_{max} = \exp(\sin\beta_0)$ of the maximum velocity on the airfoil contour, the values of $C_{y\,max}$ decreasing by no more than 8%. Note that the solution in a narrowed class of functions $P_N(\gamma)$ yields a lower estimate for the dependence $C_{y\,max} = C_{y\,max}(v_{max})$.

Actual airfoils usually have a sharp trailing edge. Numerical optimization of an airfoil with the sharp trailing edge ($\varepsilon \in (1, 2]$) for several values of v_{max} and β_0 obtained by A.N. Ikhsanova have shown that characteristics of the numerically optimized airfoils are close to the exact values obtained analytically. Moreover, in the close vicinity of the exact solutions, there are many approximate solutions (i.e., realistic airfoils with sharp or smooth trailing edges). They provide the values of the minimized functional, which are close to the minimum obtained analytically. However, the shapes of the airfoils corresponding to these approximate solutions may be strongly distinguished from the analytical optimal contours. For example, Table 2 presents characteristics of solutions obtained as a result of numerical calculations (for $\varepsilon = 2$, left-hand part of the table) and exact analytical (for $\varepsilon = 1$, right-hand part of the table). These airfoils are optimized for $v_{max} = 1.8$ and different β_0 (here, t_{max} is the maximal airfoil thickness). Note that

both numerical and analytical optimal solutions have "roof-top" velocity distributions.

ACKNOWLEDGMENTS

The work was supported by the Russian Foundation for Basic Research (project no. 03-01-00015) and by the Program "Universities of Russia" (project no. UR 04.01.009).

REFERENCES

1. M. A. Lavrentyev, Trudy TsAGI im. N.E. Zhukovskogo, No. 155, 41 (1934).
2. R. H. Liebeck, J. Aircraft. **15** (9), 547 (1978).
3. V. I. Zubov, Zh. Vych. Mat. Mat. Fiz. **20** (1), 241 (1980).
4. A. M. Elizarov, Izv. Vuzov, Ser. Mat., No. 10, 71 (1988).
5. A. M. Elizarov and E. V. Fedorov, Prikl. Mat. Mekh. **54** (4), 571 (1990).
6. A. M. Elizarov and E. V. Fedorov, Prikl. Mat. Tekh. Fiz., No. 2, 73 (1993).
7. A. M. Elizarov, E. V. Fedorov, and D. A. Fokin, Zh. Vych. Mat. Mat. Fiz. **33** (6), 958 (1993).
8. A. M. Elizarov, N. B. Il'inskiĭ, and A. V. Potashev, *Inverse Boundary Value Problems of Aerohydrodynamics: Theory and Methods for Airfoil Design and Optimization* (Fizmatlit, Moscow, 1994).
9. A. M. Elizarov and D. A. Fokin, Dokl. Akad. Nauk **377**, 758 (2001) [Dokl. Phys. **46**, 280 (2001)].
10. F. D. Ioffe and V. M. Tihomirov, *Theory of Extremal Problems* (Nauka, Moscow, 1974).

Doklady Physics, Vol. 49, No. 11, 2004, pp. 680–682. Translated from Doklady Akademii Nauk, Vol. 399, No. 2, 2004, pp. 199–201.

MECHANICS

Characteristic Elements of a Fractured Solid in Supersonic Flow

I. A. Zhdan, V. P. Stulov, and P. V. Stulov

Presented by Academician G.G. Chernyĭ June 8, 2004

Received June 9, 2004

The study of the behavior of solids in supersonic flows is of interest in various branches of mechanics, e.g., motion of multiphase media, meteoritic astronomy, and applied mechanics. In this paper, we describe the results of numerical experiments with supersonic flows around certain regular configurations containing a small number of spheres.

The goal of our calculations is the determination of aerodynamic coefficients for the spheres and investigation of the variation of the shock wave structure as a function of the distance between solids. These data, in particular, promote the understanding of mechanics of dispersing fragments after a solid has been fractured in supersonic flow.

In this study, we have chosen the four configurations shown in Fig. 1. The sphere centers and the velocity vector of incident flow lie in the same plane. The measure of the configuration size is the quantity h equal to the half-distance between the two closest points of two neighboring spheres, which is normalized to sphere radius R. Throughout the paper, for the sake of convenience, we use the sphere numbering shown in Fig. 1. Comparison of aerodynamic properties of the configurations *a–d* apparently makes it possible to draw a general conclusion on flows around systems of solids in more complicated cases. We are implying cases of irregular configurations of systems composed of several solids as well as cases of certain variations in their shapes. In this study, all the calculations are carried out for systems of solids placed in perfect-gas flows with the adiabatic index and Mach number equal to $\gamma = 1.4$ and $M = 6$, respectively.

Configuration *b* was analyzed in detail in a previous study [1] in which drag coefficient c_x and transverse-force coefficient c_y were determined. It was also proved that the largest distance between the spheres, when the transverse-force coefficient becomes small, corresponds to the tangency of the sphere and the reflected shock wave.

Flows of the type *a* are known in the literature as flows around a solid in the wake of another solid [2]. Previously, the problem was solved mainly for relatively small distances between solids and for solid shapes corresponding to various applied purposes (e.g., separation of rocket stages, release of protector caps, etc.). Here, we consider flows around two spheres with the centerline directed along the flow.

As our calculations have shown, the drag coefficient for the front sphere initially slightly increases with h but, from $h \approx 2$, it takes values corresponding to flow around a single sphere. This distance is close to two calibers of the solid and, approximately, corresponds to the lower downstream boundary of the near wake beyond the front sphere [3]. With further increasing of h, drag coefficients c_x remain virtually constant. In other words, the flow around the front sphere is no longer dependent on the presence of another solid in its wake. At the same time, the drag coefficient c_x for the second (rear) sphere rises very slowly nonmonotonically from a certain rather small value ($\sim 0.1 c_{x1}$) at $h = 0$. For example, at $h = 10$, we have $c_{x4} = 0.115$. For configuration *a*, the calculated values c_{x1} and c_{x4} as functions of h are shown in Fig. 2.

We should note that, in the downstream-boundary region of the near wake beyond the front sphere ($h \approx 2$), significant oscillations of the calculated c_{x4} values are observed. Figure 2 shows the average values of c_x for a random sampling, the deviations from the average values being marked by vertical segments. The values of c_{x1} also fluctuate, but with a considerably smaller

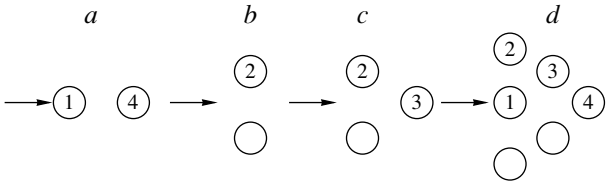

Fig. 1. Disposition of spheres in configurations *a*, *b*, *c*, and *d*.

Research Institute of Mechanics, Moscow State University, Vorob'evy gory, Moscow, 119899 Russia
e-mail: djo@access.izba.ru; stulov@imec.msu.ru; pstulov@imec.msu.ru

1028-3358/04/4911-0680$26.00 © 2004 MAIK "Nauka/Interperiodica"

amplitude. The possibility of a hysteresis in the pattern for the flow around the rear sphere under the specified conditions was indicated in [2]. For $h < 2$ and $h > 2$, oscillations of the coefficients c_x are virtually absent.

Aerodynamics of system *c* (Fig. 1) was compared to the results of studies of flows around system *b* [1]. Drag coefficient c_{x2} and transverse-force coefficient c_{y2} of sphere 2, as well as drag coefficient c_{x3}, for sphere 3 are plotted in Fig. 3 by solid lines. For comparison, values of c_{x2} and c_{y2} in configuration *b* are shown in this figure by dashed lines. As is seen, the presence of the third sphere only negligibly changes the conditions for the flow around the front spheres. This small variation is manifested as a certain decrease in both c_x and c_y for the front sphere due to the increase in the bottom pressure, which is associated with the existence of the third sphere. The shape of the leading shock wave in front of the two front spheres is almost invariable in this case.

We now discuss the flow near sphere 3. When distances *h* are small, a shock wave is formed in front of sphere 3. This wave is limited in its amplitude due to the inhomogeneity of the incident flow. The amplitude of the shock wave increases with *h*, and the drag coefficient c_{x3} monotonically rises. The situation remains constant up to distances for which the interaction of the front spheres ceases, i.e., for $h > 0.5$. With increasing *h*, the reflected shock wave hits the front part of sphere 3 so that the coefficient c_{x3} continues to rise. With further increasing *h*, the reflection point and, furthermore, the lateral part of the leading shock waves of spheres 1 and 2 turn out to be on the leading shock wave of sphere 3. During the entire period of the interaction with sphere 3 of the shock waves from the front spheres, drag coefficient c_{x3} exceeds that of a single sphere. This is illustrated by Fig. 3, where, starting from $2h \geq 1.0$, the linear scale along the *x* axis is replaced by a logarithmic scale. Here, we note a new aspect of the interaction in the system under consideration of supersonic flows around solids, namely, that the interaction of reflected shock waves with solids results not only in the appearance of a transverse force but also of a significant increase in the drag.

The pattern of flows around configuration *d* (Fig. 1) repeats the tendencies considered above. For example, the flow around the set of spheres 1, 2, and 3 is similar to the flow around system *c*. This fact justifies employing the term *characteristic elements*. The drag coefficients and the transverse-force coefficients for spheres 2 and 3 and the drag coefficients for spheres 1 and 4 are represented in Fig. 3 by symbols. Here, we observe a more noticeable drag reduction for sphere 1 rather than for sphere 2, for which this reduction virtually repeats the decrease in c_{x2} for system *c*. This occurs by virtue of a large elevation of the bottom pressure on sphere 1 due to the existence of a third layer composed by sphere 4 entering into configuration *d*. At the same time, the drag related to sphere 4 increases with *h* more slowly than the resistance of sphere 3 (in both systems *d* and *c*).

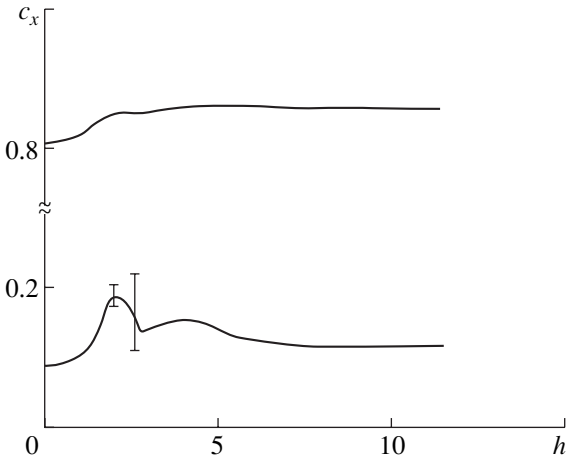

Fig. 2. Drag coefficient for spheres in configuration *a*.

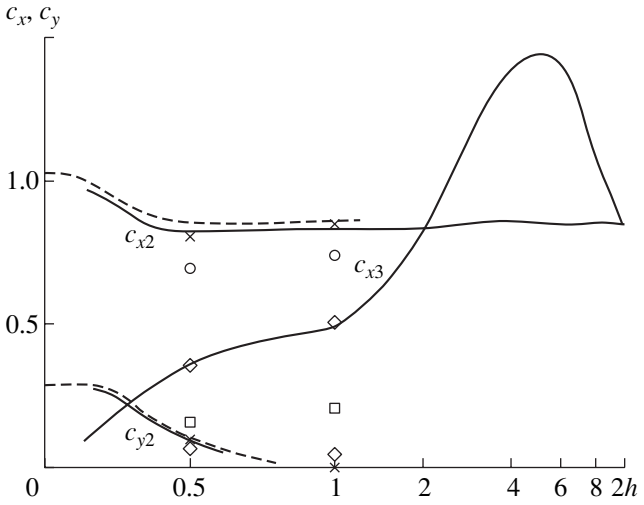

Fig. 3. Drag coefficients and transverse-force coefficients in configurations: (*b*) dashed lines; (*c*) solid lines; and (*d*) [symbols: (○) c_{x1}, (×) c_{x2}, c_{y2}; (◇) c_{x3}, c_{y3}; and (□) c_{x4}].

The shape of the leading shock wave varies with *h* practically in the same manner as for configurations *b* and *c*. The transformation of a common shock wave in front of the system into individual shock waves in front of each sphere occurs in the head part of the system. It is evident that the above-mentioned aspect of the interaction of reflected shock waves with leading shocks in front of the spheres of rear rows also exists and results in a noticeable increase in the drag for these spheres.

The pattern of flows around system *d* for $h = 0.5$ is shown in Fig. 4. The principal features of the flow repeat the preceding cases.

The basic conclusion of this study is that, in the case of a supersonic flow around a system of solids, the flow distortions stipulated by the collective nature of an obstacle drift, as it were, downstream. A slight decrease in the drag of head spheres is caused by increasing bottom pressure. However, this virtually does not affect the

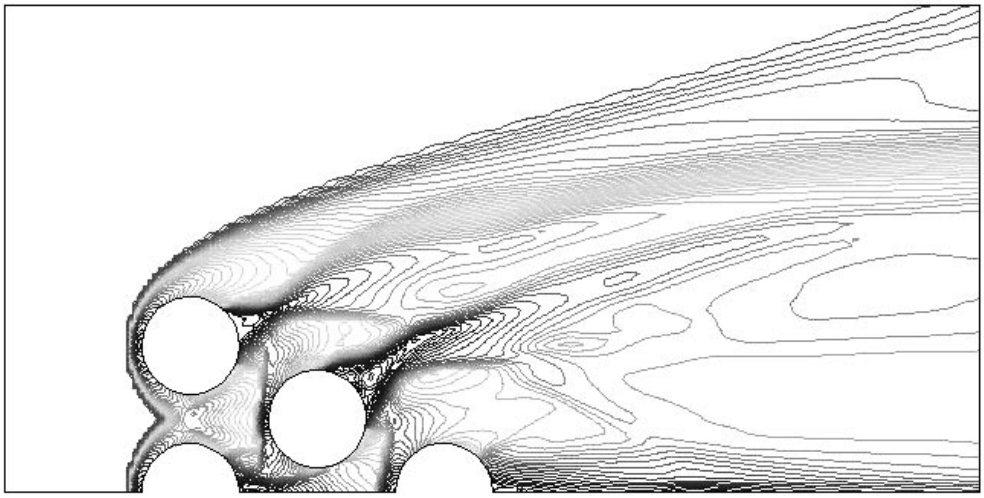

Fig. 4. Pattern of flow around solids in configuration *d* (*h* = 0.5).

reconstruction of the leading shock wave, which monotonically decays into individual shock waves with an increase in the distance between the spheres. The characteristic distance between solids, which corresponds to this decay, also remains invariable and entirely corresponds to the simple case of flow around a pair of spheres with their centerline aligned across the flow.

ACKNOWLEDGMENTS

This work was supported by the Russian Foundation for Basic Research, project no. 02-01-00204.

REFERENCES

1. I. A. Zhdan, V. P. Stulov, and P. V. Stulov, Dokl. Akad. Nauk **396**, 191 (2004) [Dokl. Phys. **49**, 315 (2004)].
2. I. G. Eremeĭtsev, N. N. Pilyugin, V. S. Khlebnikov, *et al.*, *Studies of Aerodynamic Characteristics and Heat Exchange in Nonequilibrium Supersonic Gas Flows* (Izd. Mos. Gos. Univ., Moscow, 1988).
3. A. I. Shvets and I. T. Shvets, *Gas Dynamics of Near Wake* (Naukova Dumka, Kiev, 1076).

Translated by G. Merzon

Doklady Physics, Vol. 49, No. 11, 2004, pp. 683–685. Translated from Doklady Akademii Nauk, Vol. 399, No. 3, 2004, pp. 339–341.

MECHANICS

Wave Generation under High-Speed Collision of a Plate with a Cone

B. A. Boĭko, A. E. Dubinov, and V. D. Selemir

Presented by Academician G.G. Chernyĭ June 16, 2004

Received June 30, 2004

In this paper, results of experimental studies of wave generation in a contact melted layer under axial collisions of metallic plates with metallic bodies made in the form of truncated right circular cones are presented. In this case, a closed regular structure of the contact layer was formed for the first time as a series (train) of long waves on the exterior surfaces of copper and aluminum cones. It is found that the dependence of the measured wavelength on the group velocity corresponds to the rising branch of the wave dispersion law.

The phenomenon of wave generation on contact layers in high-speed collisions of metallic bodies is studied for a long time. (We imply both fundamental studies, e.g., analysis of hydrodynamic instability of viscoplastic flows in contact melted layers in the collision zone and industrial applications, e.g., the plating and welding explosion technologies [1–4].) Investigation of waves generated on the contact surface of metallic screens under high-speed collision with a body is important for the development of methods for efficient protection of objects in space against meteorite impacts. In a large degree, the interest in the process of wave generation is also caused by the possibility to study wave phenomena from the standpoint of general wave theory, as the contact layer is a medium in which the effects of dispersion and nonlinearity manifest themselves in full measure. These waves can be observed during and after a collision, and their shapes store information on the evolutionary stages of contact layers.

Up to now, wave generation has been studied only for oblique incidence of flat plates when the collision angles are acute and strongly limited ($\gamma \le 20°$), whereas the wavelengths of the waves being produced are small ($\lambda \le 1$ mm) and are determined by the capillary tension of the contact surface. In this case, as is known from [5], the dispersion law for the phase $v_p(\lambda)$ and group $v_g(\lambda)$ velocities of capillary waves are determined by diminishing branches of the dependences $v_p(\lambda)$ and $v_g(\lambda)$.

Russian Federal Nuclear Centre,
Institute of Experimental Physics,
Sarov, Nizhni Novgorod oblast, Russia

One more feature of colliding flat plates is the significant effect of their edges, which complicates the wave pattern.

In this connection, it is of interest an advance into the region of large (even obtuse) collision angles and long wavelengths ($\lambda \ge 1$ mm). Then, wave generation is developed along the rising branch of the dependence $v_g(\lambda)$, and boundary distortions of the wave pattern by virtue of the formation of waves with a closed wave front are excluded. The latter requirement can be provided in the case of collisions with a body of special geometric shape, in particular, with a rod [1].

In the present paper, we describe the results of our experimental studies of wave generation in a contact melted layer. We consider axial collisions of metallic plates with metallic bodies in the form of truncated right circular cones. In this case, a closed regular structure in the form of a series (train) of long waves was formed for the first time on the exterior surfaces of copper and aluminum cones.

Scheme of the experiment. As shown in Fig. 1, between two square metallic plates *1*, a charge of a high explosive *2* based on plasticized RDX was placed. Truncated metallic cones *3* were installed outside of the plates so that the smaller-diameter bases of each of the cones closely adjoined the corresponding plate in its center. The cone axes coincided and were normal to the plate planes. Special traps filled with sand provided the preservation of the cones after the experiment (the traps are nor shown in Fig. 1).

Flat metallic plates of a size from 150 to 180 mm and 1 mm thick were used in the experiment. The explosive charges possessed sizes coinciding with those of the plates and thicknesses of 2, 4, and 6 mm. The truncated cones had the smaller diameter d_1 = 30–60 mm and larger diameter d_2 = 80–120 mm. To exclude the edge effects associated with plate boundaries and with explosion-product unloading at the plate edges, cone diameters d_2 always were smaller than the sizes of metallic plates and explosive charges. In the experiments, the angle α (Fig. 1) between the directrix of the smooth surface of the cone *3* and the plate *1* was 45°, 50°, 55°, 60°, and 65°. In this case, the collision

1028-3358/04/4911-0683$26.00

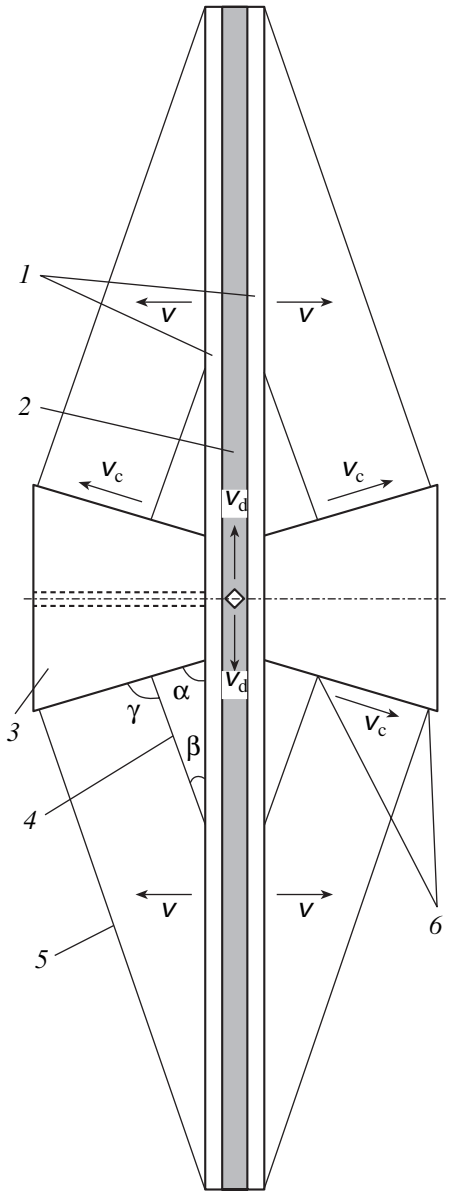

Fig. 1. Device for investigation of waves arising in collision of plates with two cones: (*1*) metallic plates in their initial positions (prior to the explosion); (*2*) explosive charge; (*3*) truncated metallic cones (d_1 and d_2 are the smaller and the larger base diameters, respectively); (*4*) plate boundary in the intermediate stage after explosion; (*5*) plate boundary after the experiment; (*6*) contact point of the plate and the cone: γ is the collision angle, α is the initial angle between the plate and the cone, β is the plate rotation angle under the action of explosion products v_d is the velocity of the detonation moving along the explosive, v is the plate velocity under the action of explosion-product pressure, $v_c(\lambda) \approx v_g(\lambda)$ is the contact-point velocity.

angle of the plate and the cone turned out to be obtuse and attained a value of $\gamma = \alpha + \beta$, where $\beta = \arctan\frac{v}{v_d}$ is the angle of the plate rotation under the action of explosion products, v is the velocity of plate motion (the velocity value depends on the ratio between the masses of the plate and of the explosive), and v_d is the detonation velocity. In our experiments, plate velocity v can vary within limits of 1–4 km s^{-1}. Displacement velocity v_c for the contact point can be calculated according to the formula $v_c = \frac{v}{\sin\alpha}$. As plate materials, we employed copper–copper (Cu–Cu) and aluminum–aluminum (Al–Al) pairs, etc. The explosive charge was placed in the center of the device.

In order to record collision dynamics and wave generation in our experiments, we used pulsed X-ray photography and ultrahigh-speed photography methods. After the experimental loading had been over, the states of the interface metal layers were studied in flat plates cut from the cones (Fig. 2) that were preserved in the trap. In order to investigate the contact-layer structure, the plates were grinded and polished up to the mirror luster. After etching, the microstructure of metal in the contact zone of the metallographic section was studied with a microscope. These studies made it possible to determine the depth of metal melting and reveal the nonlinear character of the wave (rise of crest steepness).

We measured amplitude a and wavelength λ in the longitudinal direction with respect to the contact-point motion and investigated the profile of the leading and trailing fronts of longitudinal waves. Wavelength λ was determined as the average distance between crests at a baseline of ten periods. In discussions of strain wavelength, we should take into account the flow evolution along the cone-directrix length. Similarly to in the case of flows in channels, we separated the initial segment and that of hydrodynamic stabilization. The stabilization segment was determined according to integral parameters such as the mean wavelength or mean wave amplitude. To increase the statistics of the experiment, a significant part of the experimental runs were performed under the same initial parameters at both sides of the explosive charges: identical material and identical angles of the cones and identical material and identical angles β of the plates, as well as identical material of the plates and cones. It should be noted that attaining a stabilized wave regime was independent of the plate thickness but depended on another linear scale (apparently, on the wave-flow thickness). This is why the stabilization of wave regimes occurred at short distances (λ–3λ) from the smaller cone base. Thus, in analyzing the wave regime, the evolutionary nature of the wave flow was noted and actual cone sizes were taken into account.

About one hundred experiments were performed. The accumulated experimental data made it possible to plot the dependence $v_c(\lambda) \approx v_g(\lambda)$ (Fig. 3). In particular, it follows from this dependence that, in our experiments, wave generation is realized that develops along the rising branch of the dependence $v_g(\lambda)$. The obtained regimes admit both the possibility of advancing into the

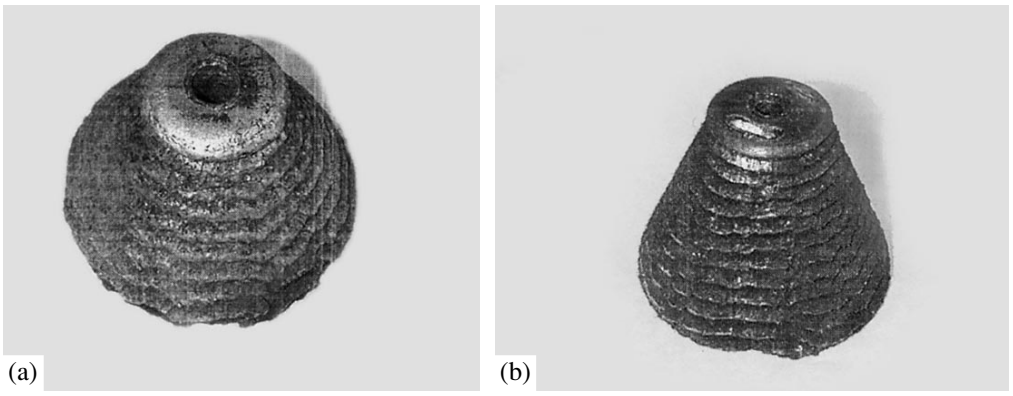

Fig. 2. Cone after ultrahigh-speed collision with plates: (a) aluminum cone; (b) copper cone.

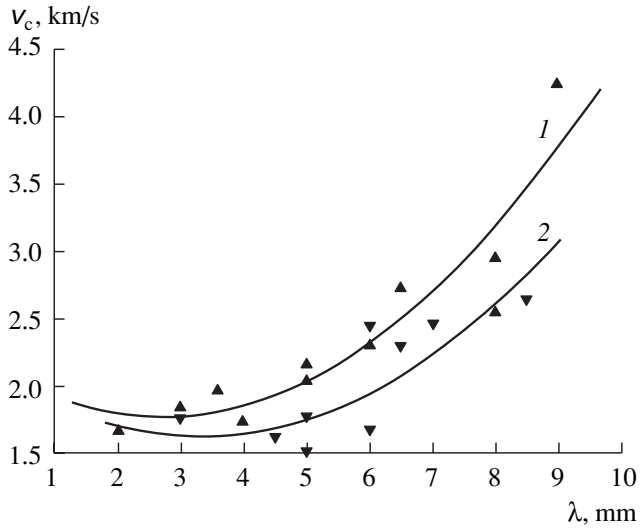

Fig. 3. Rising branch of dispersion law for the group velocity [$v_c(\lambda) \approx v_g(\lambda)$] as a function of the wavelength λ: (▲) Al–Al and (▼) Cu–Cu.

region of large angles γ (obtuse angles) and of excluding edge effects on the wave pattern. These facts allow us to conclude that, in the present study, a new method of investigating wave phenomena inherent in high-intensity pulsed processes has been developed.

REFERENCES

1. *Wave Generation at Oblique Collisions: Collective Papers* (Inst. Discr. Math. Informatics, Novosibirsk, 2000).
2. Yu. A. Gordopolov, A. N. Dremin, and A. N. Mikhaĭlov, Fiz. Goreniya Vzryva **10**, 288 (1977).
3. S. K. Godunov, A. A. Deribas, and N. S. Kozin, Prikl. Mat. Tekh. Fiz., No. 3, 63 (1971).
4. O. B. Drennov, A. L. Mikhaĭlov, P. N. Nizovtsev, *et al.*, Zh. Tekh. Fiz. **73** (8), 62 (2003).
5. S. V. Alekseenko, V. E. Nakoryakov, and B. G. Pokusaev, *Wave Flow of Fluid Films* (Nauka, Novosibirsk, 1992).
6. E. I. Bichenkov and V. A. Lobanov, Fiz. Goreniya Vzryva **10**, 292 (1974).

Translated by G. Merzon

Doklady Physics, Vol. 49, No. 11, 2004, pp. 686–690. Translated from Doklady Akademii Nauk, Vol. 399, No. 3, 2004, pp. 342–346.

MECHANICS

Formation and Growth of Perturbations while Throwing a Weakly Elastic Shell

A. N. Golubyatnikov*, S. I. Zonenko, and Academician G. G. Chernyĭ****

Received July 29, 2004

1. INTRODUCTION

Recently, experimental investigations of the motion of an initially almost plane layer made of an easily deformable material (in particular, a round copper plate with a correspondingly sized triangular-net pattern deposited onto it) that is thrown under the action of a large pressure drop were carried out [1]. These experiments resulted in an understanding of the fact that, under these conditions, a steadily, reproducible growth of perturbations with a certain wavelength on the order of several layer thicknesses occurred.

It was typical for the experiments performed that the pressure drop much exceeded the elasticity limit of a material but is lower than the Young's modulus. In the present study, for describing the behavior of a shell under these conditions, we propose a model of a weakly elastic material. This model generalizes the pure inertial model of [1] and well describes the totality of available experimental data. Without touching upon the physical essence of proceeding elastoplastic processes, we assume that, at the initial acceleration stage, the shell acquires an efficient longitudinal elasticity, with the modulus proportional to the acting pressure (weak elasticity). Such a weak elasticity prevents only expansion of the shell and is similar to the model of three-dimensional Treloar medium found as a result of statistically substantiated observations of the structure of rubber, which were described in [2].

In the model of a weakly elastic shell as in the inertial-motion model [1, 3], the plane problem is reduced to a set of linear equations and, thus, can be efficiently investigated. In particular, for a homogeneous shell, the qualitative behavior of solutions is specified by the corresponding dispersion equation. From this equation, it follows that the process of the development of short waves occurs in an oscillatory mode. It should be remembered that the theory can be applied when the actual wavelength greatly exceeds the characteristic shell thickness, which constrains the wavelength spectrum from below. Furthermore, there exists a critical wavelength for which the vibration frequency vanishes, whereas perturbations with a wavelength exceeding the critical one increase. In turn, the wavelength range involves a (resonance) wavelength equal to the double critical wavelength with the largest growth increment. With further increase in the wavelength, the increment decreases to zero.

In the spatial case, the set of equations is quadratically nonlinear. The experimentally observed effect [1] when six depressions appear on an obstacle and are regularly located with respect to its center corresponds to the three-wave resonance characteristic of the quadratic nonlinearity. A decrease by half in the thickness of a round plate (and, correspondingly, in the step of the deposited net) under the same other parameters results in the appearance of the second row of 18 depressions with correspondingly smaller depths and half the distance between their centers.

It is characteristic that depositing a pattern adequate to the critical or somewhat smaller wavelength promotes a more stable plate speed up, which results in a single wide depression with a plane bottom on an obstacle. Moreover, for a plate thickness comparable to the obstacle diameter, this results in spallation from the plate's opposite side.

Correct understanding of the dynamic processes that proceed in the case of motion of easily deformed shells makes it possible to improve the reproducibility and to increase the efficiency of various explosive devices that often operate in an unstable way [4].

2. EQUATIONS OF MOTION FOR A SHELL

The equations of motion for a weakly elastic shell have the form

$$\sigma \mathbf{r}_{tt} = p\mathbf{n} + \nabla_\alpha(\sigma c^2 a_0^{\alpha\beta}\mathbf{r}_\beta), \qquad (1)$$

where $\mathbf{r}$ is the radius vector of the shell particles with Cartesian Eulerian components x^i and $\mathbf{n}$ is the vector of a unit normal directed toward the reduced pressure. The

* *Mechanical and Mathematical Faculty, Moscow State University, Vorob'evy gory, Moscow, 119192 Russia*

e-mail: golubiat@mech.mat.msu.su

** *Institute of Mechanics, Moscow State University, Michurinskiĭ pr. 1, Moscow, 119192 Russia*

1028-3358/04/4911-0686$26.00

subscript t implies the derivative with respect to time for the constant Lagrangian coordinates ξ^α, $\alpha = 1, 2$, and the subscript β denotes a derivative with respect to ξ^β. The symbol ∇ corresponds to the covariant derivative over a surface, and σ is the surface density.

Below, pressure p is considered as constant and equal to the initial pressure p_0; in the general case, we can assume it to be a function of t as well. We also assume the square of the effective velocity of sound in a shell material to be $c^2 = \frac{\kappa p_0}{\rho}$, where $\rho(\xi^\alpha)$ is the density of a shell material (considered as incompressible), κ is the dimensionless factor (for metallic shells, it is close to unity). It is also useful to introduce the shell thickness by the formula $h = \frac{\sigma}{\rho}$.

Let $a_{\alpha\beta}$ be the components of the metric tensor of the shell surface,

$$a_{\alpha\beta} = \delta_{ij} x^i_\alpha x^j_\beta, \quad x^i_\alpha = \frac{\partial x^i}{\partial \xi^\alpha}, \tag{2}$$

x^i_α represent the components of the vectors $\mathbf{r}_\alpha$ tangential to the surface so that $\mathbf{n} = \frac{\mathbf{r}_1 \times \mathbf{r}_2}{|\mathbf{r}_1 \times \mathbf{r}_2|}$; and $|\mathbf{r}_1 \times \mathbf{r}_2| = \sqrt{\det(a_{\alpha\beta})} \equiv \sqrt{a}$.

Symbols $a_0^{\alpha\beta}$ denote the initial contravariant components of the surface metric tensor, which are used with the factor c^2 as the components of the specific elastic-constant tensor. It should be noted that, here, we consequently take into account all the elements of the shell finite-deformation theory without linearization, although the elastic term finally turns out to be linear.

Indeed, by virtue of the law of conservation of mass, the Lagrange formula

$$\sigma = \sigma_0 \sqrt{\frac{a_0}{a}} \tag{3}$$

is valid. As above, zero subscripts denote the corresponding initial values of the functions ξ^α. Using formulas (1) and (3), we obtain the vector equation

$$\sigma_0 \sqrt{a_0} \mathbf{r}_{tt} = p_0 (\mathbf{r}_1 \times \mathbf{r}_2) + (\sqrt{a_0} \sigma_0 c^2 a_0^{\alpha\beta} \mathbf{r}_\beta)_\alpha. \tag{4}$$

In the case of the shell with an edge, to get rid of the possibility of gas leaking onto the forward shell surface and of analysis of the edge rarefaction waves arising in this case, we consider the shell as being placed into a channel of the corresponding shape. Thus, the shell is considered as a deformable piston. In the case of intersection of trajectories of shell particles, we make use of a model of perfectly inelastic impact corresponding to summing the vector momenta of colliding material points. In this case, depending on the collision configuration, both new surfaces and rods, or even individual material points can be formed.

3. SPHERICALLY SYMMETRIC SOLUTIONS

Ignoring the pressure drop of pushing gas, we study the acceleration of a shell with zero initial velocity. We consider focusing on a homogeneous shell corresponding to the external surface of a spherical segment of mass M into a point under the action of an external constant pressure p_0. Let $r_0 \gg h_0$ be the initial radius. Then, Eq. (4), with allowance made for the spherical radial coordinate $r(t)$, yields

$$\ddot{r} = -\frac{p_0 r^2}{\sigma_0 r_0^2} - \frac{2c^2 r}{r_0^2}, \quad \sigma = \frac{\sigma_0 r_0^2}{r^2} \tag{5}$$

with the initial data $\dot{r}(0) = 0$ and $r(0) = r_0$. Equation (5) has the energy integral

$$\frac{\dot{r}^2}{2} + \frac{p_0}{3\sigma_0 r_0^2}(r^3 - r_0^3) + \frac{c^2}{r_0^2}(r^2 - r_0^2) = 0, \tag{6}$$

which can be used for representing the solution in the quadrature form, $t(r)$.

It should be noted that, by virtue of the assumption $c^2 = \frac{\kappa p_0 h_0}{\sigma_0}$, the term containing c^2 in Eq. (5) is small. In addition, the incompressibility of the shell material renders it impossible to approach the center $r = 0$, and it is necessary to be constrained by the radii $r > h \sim (h_0 r_0^2)^{1/3}$.

The collapse time is determined by the relation

$$t_* = \sqrt{\frac{3\sigma_0 r_0}{2p_0}} \int_0^1 \frac{dx}{\sqrt{1 - x^3 + \delta(1 - x^2)}}, \quad \delta = \frac{3\kappa h_0}{r_0}. \tag{7}$$

After the collapse, according to the model of perfectly inelastic impact, lumped mass M moves along a straight line. In addition, in the absence of a pressure force due to the zero surface area, the motion occurs at a constant velocity.

Thus, by virtue of the inequality $r_0 \gg h_0$, introduction of elasticity plays a negligible role and makes it possible to use the results of [3]. In particular, the results of optimization of the collapsing-segment momentum with respect to the segment opening angle, generally speaking, remain unchanged.

Based on the Hugoniot solution for the acceleration of a plane piston, which is accompanied by the formation of a rarefaction wave, we present the estimate of applicability of the p_0-steadiness condition up to the

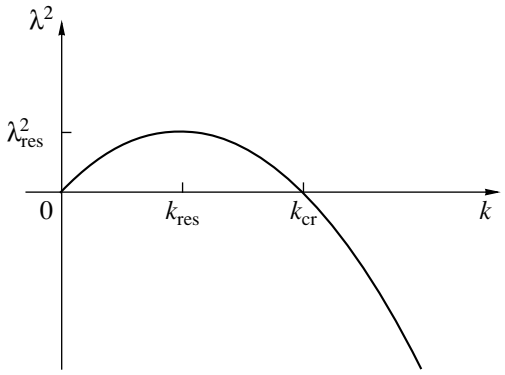

Fig. 1. Dispersion curve.

instant of shell collapse. From Eq. (7), we obtain the condition $\frac{\rho}{\rho_g} \gg \frac{r_0}{h_0}$, where ρ_g is the throwing-gas density, which is quite feasible for a reasonably dense material and a not-too-thin shell.

We also consider the problem of the motion of a spherical segment in a perfectly rigid pipe. In this case, it is necessary only to change the sign in Eq. (5) ahead of the pressure term p_0. We will show that an unlimited energy accumulation takes place under the expansion.

Let a hemisphere of radius r_0 be enclosed in a pipe of the same radius at the initial instant of time $t = 0$. Then, the hemisphere starts to accelerate under the action of the pressure p_0 (we ignore the shell elasticity). A fraction of the shell material is pressed onto the pipe surface, so that only a segment of radius $r(t) = \frac{r_0}{\sin\theta(t)}$, where θ is the segment half-opening angle, remains free at the current instant of time. Furthermore, motion of a cylindrical layer along the wall is not considered; this motion depends on the conditions of the layer–wall interaction. The segment area is $S = 4\pi r^2 \sin^2\frac{\theta}{2}$.

The calculation of the mass and energy of the segment under consideration yields, respectively,

$$M = \sigma S = 4\pi\sigma_0 r_0^2 \sin^2\frac{\theta}{2},$$
$$E = M\frac{\dot r^2}{2} = \frac{4\pi p_0 r_0^3}{3}\left(\frac{1}{\sin^3\theta} - 1\right)\sin^2\frac{\theta}{2}. \quad (8)$$

Thus, we have $\theta \longrightarrow 0$, $M \longrightarrow 0$, and $E \longrightarrow \frac{1}{\sqrt{M}} \longrightarrow \infty$ as $r \longrightarrow \infty$ ($S \longrightarrow \pi r_0^2$). It should be noted that the segment axial momentum tends to zero: $P = \sqrt{2ME} \sim M^{1/4} \longrightarrow 0$.

As $r \longrightarrow \infty$, the asymptotic law of motion has the form

$$r \approx \frac{6\sigma_0 r_0^2}{p_0}\frac{1}{(t - t_\infty)^2}, \quad t_\infty = 3.013\sqrt{\frac{\sigma_0 r_0}{p_0}}. \quad (9)$$

The spherically symmetric solutions and their asymptotic behavior also play an important role in studying internal resonances. In addition, these solutions can serve as tests for the approbation of various approximate methods.

4. THE PLANE PROBLEM

In the case of a plane problem, we have $x^3 = \xi^3$, all other variables being functions of ξ^1 and t. We introduce the complex Eulerian variable $z = x^1 + ix^2$ and also use the mass variable $\mu = \int \sigma_0\sqrt{a_0}\, d\xi^1 p_0^{-1}$ as the Lagrangian coordinate to simplify the equations. Thus, $\sigma = \frac{p_0}{|z_\mu|}$. The dimension of the variable μ is equal to that of t^2.

Then, the equations of motion take the form

$$z_{tt} = iz_\mu + (\tilde c^2(\mu) z_\mu)_\mu, \quad \tilde c^2 = \frac{\kappa\rho h_0^2}{p_0}. \quad (10)$$

It should be noted that material density ρ and initial thickness h_0 can vary.

Complex Eq. (10) represents a set of two hyperbolic equations. However, even for a constant value of $\tilde c$, it has a strong dispersion, which in many respects characterizes the unusual behavior of solutions with different initial data.

We consider an elementary solution in the case $\tilde c$ = const, which locally corresponds to the cylinder expansion. Let $z = A_0\exp(\lambda t - ik\mu)$, where A and λ are complex constants, and $k > 0$ is a real number. Then, we arrive at the following dispersion equation:

$$\lambda^2 = k - \tilde c^2 k^2, \quad (11)$$

which shows that, in particular, there is a critical wave number $k_{cr} = \frac{1}{\tilde c^2}$ corresponding to the equilibrium state $\lambda = 0$ (Fig. 1).

For the wave numbers $k < k_{cr}$, the quantity λ is real. This corresponds to either the growth or attenuation with time of wave amplitude $A_0\exp(\lambda t)$, therewith only one maximum for $|\lambda|$ at $k = \frac{k_{cr}}{2}$ takes place. Thus, there is a wave with the mass length $4\pi\tilde c^2$ (which we, hereinafter, will call the resonance length) and the most rapidly growing amplitude. This resonance length charac-

terizes the maximal instability of the process. In conventional variables, this yields the relation

$$\int_0^{l_{res}} \sigma_0\sqrt{a_0}d\xi^1 = 4\pi\kappa\sigma_0 h_0 = \text{const}, \quad (12)$$

which approximately (because, generally speaking, $\sigma_0\sqrt{a_0}$ is not constant) corresponds to the wavelength $l_{res} \approx 4\pi\kappa h_0$. The amplitude growth rate decreases down to zero as $k \longrightarrow 0$. For example, at the constant σ_0 and a small initial perturbation of the plane, quantity $\sigma_0\sqrt{a_0}$ differs from a constant by a value of the second order of smallness.

In the case of $k > k_{cr}$, the parameter λ becomes purely imaginary, $\lambda = i\omega$, where ω is the vibration frequency of the amplitude being time periodic.

Evidently, each of the solutions of the indicated type has a cylindrical symmetry and can describe a monotonic expansion or compression, as well as the vibration or equilibrium of a cylindrical shell. By virtue of the linearity and uniformity of Eqs. (10), it is also possible to complement their solution with a solution adequate to the solid-state motion. Then, it is possible to speak about the more complicated motion of a corrugated shell (this solution was indicated in [1]). In this case, deviations of the shell shape from a plane, even if they are initially small, grow exponentially near the resonance wavelength, anticipating the average motion with a constant acceleration.

5. THE THREE-WAVE RESONANCE

As the example of spherically symmetric solution (9) shows, a shell speed up even more rapid than the exponential one [about $\frac{1}{(\Delta t)^2}$)$_2$] is possible. Could small perturbations of a plane lead to such a growth? In particular, the experiment with a thrown round plate symmetrically divided into six sectors indicates the formation of six depressions on an obstacle [1]. This fact, as can be assumed, qualitatively corresponds to the wavelength of a vibration with an extremely rapidly increasing amplitude. This implies the presence of a three-wave internal resonance characteristic of quadratic nonlinearity [5]. We now show that this resonance results in a shell acceleration of the same order of magnitude as in the spherical solution.

We assume that the initial perturbations are reasonably small, so the coefficients in Eq. (4) can be considered as constant. Thus, we have

$$\mathbf{r}_{tt} = g_0(\mathbf{r}_1 \times \mathbf{r}_2) + c^2\delta^{\alpha\beta}\mathbf{r}_{\alpha\beta}, \quad g_0 = \frac{p_0}{\sigma_0}. \quad (13)$$

We consider the problem of throwing a plane on which a symmetric pattern of three standing waves is realized. The perturbed part of the solution is expanded in terms of the three-periodic functions adequate to a triangular lattice in sites on which, for example, the maxima of vertical (along $\mathbf{e}_3$) perturbations are located. Thus, there is a group of the sixth-order rotations leaving the given site at rest, along with a group of the corresponding translations.

The solution has the form

$$\mathbf{r} = \mathbf{r}_0 + \mathbf{r}_I + \mathbf{r}_{II}, \quad \mathbf{r}_0 = \mathbf{e}_\alpha\xi^\alpha + \frac{\mathbf{e}_3 g_0 t^2}{2},$$

$$\mathbf{r}_I = \frac{1}{2}\sum_{p=1}^{3}(A(t)\mathbf{e}_3 - iB(t)\mathbf{k}_p)E^p(\xi^\alpha) + \text{c.c.}, \quad (14)$$

$$E^p = \exp(ikk_\alpha^{(p)}\xi^\alpha),$$

where the c.c. implies complex conjugation.

Here, it is accepted everywhere that $k = k_{res} = \frac{g_0}{2c^2} = \frac{1}{2h_0\kappa}$, which corresponds to plane waves with the most rapidly increasing amplitude. The vectors $\mathbf{k}_p = \mathbf{e}_\alpha k_{(p)}^\alpha$ (the sum of which is zero) are

$$\mathbf{k}_1 = (1, 0, 0), \quad \mathbf{k}_2 = \left(-\frac{1}{2}, \frac{\sqrt{3}}{2}, 0\right),$$

$$\mathbf{k}_3 = \left(-\frac{1}{2}, -\frac{\sqrt{3}}{2}, 0\right).$$

It is clear that the term $\mathbf{r}_I$ is invariant with respect to permutations of vectors $\mathbf{k}_p$. The component $\mathbf{r}_{II}$ corresponds to the sum of higher nonresonance harmonics that increase more slowly. They appear as a result of quadratic interaction between plane waves. In the case of a single wave, $A = B = A_0\cosh\lambda t$ and $\lambda = \frac{g_0}{2c}$.

After substituting these formulas into Eq. (13) and reducing similar terms in the expressions for the functions E^p, we obtain two equations for the complex functions A and B,

$$\ddot{A} = g_0 k\left(B - \frac{1}{2}A + \frac{3}{8}k\bar{B}^2\right),$$
$$\ddot{B} = g_0 k\left(A - \frac{1}{2}B + \frac{3}{4}k\overline{AB}\right), \quad (15)$$

where the bar symbol implies complex conjugation.

The initial conditions are

$$A(0) = B(0) = A_0, \quad \dot{A}(0) = \dot{B}(0) = 0,$$

which corresponds to symmetric interaction between originally three plane waves of a small amplitude A_0.

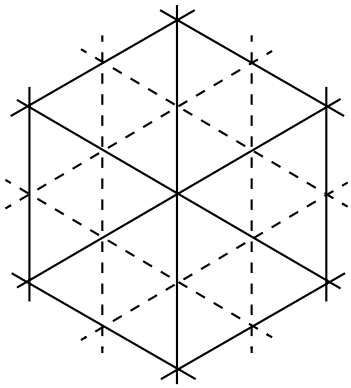

Fig. 2. Schematic arrangement of lines of extrema composing the shell heights.

It is clear that the best case of organizing shell acceleration is, in particular, a real positive A_0. In this case, the solution to Eqs. (15) is also both real and positive. For complex $A_0 = |A_0|e^{i\alpha}$, the effect of the argument α, generally speaking, results in the absence of an intersection between three lines of maxima of the functions $\cos(kk_\beta^{(p)}\xi^\beta + \alpha)$. For a real negative A_0, we obviously have the threefold minimum at the point $\xi^\beta = 0$.

Equations (15) have the energy integral

$$\frac{1}{2}(|\dot{A}|^2 + |\dot{B}|^2) - \frac{g_0 k}{2}\left(B\bar{A} + A\bar{B} - \frac{1}{2}(|A|^2 + |B|^2)\right.$$

$$\left. + \frac{3k}{8}(AB^2 + \overline{AB^2})\right) = E_0$$

and can be solved numerically.

Let $\alpha = 0$. Then, it is also possible to propose a simple approximation of the solution by elementary functions with allowance made for asymptotic behaviors as $t \longrightarrow 0, \infty$. In the dimensionless form, we have $a = kA$, $b = kB$, and $\tau = \sqrt{g_0 k}\, t$,

$$a = a_0 + \frac{a_0\tau^2}{\left(2 - \left(\frac{a_0}{2}\right)^{1/4}\tau\right)^2},$$

$$b = a_0 + \frac{a_0\sqrt{2}\tau^2}{\left(2 - \left(\frac{a_0}{2}\right)^{1/4}\tau\right)^2} - \frac{a_0(\sqrt{2}-1)\tau^2}{4}.$$

The dimensionless time of attaining infinity is $\tau_\infty = 2\left(\frac{2}{a_0}\right)^{1/4}$.

The analysis of the solution shows that, at the points corresponding to the lines of minima of the functions $\cos kk_\beta^{(p)}\xi^\beta$ in which there is a backward convexity in the initial profile, the collapse takes place, and the material plane strips lagging from the basic surface are formed. In Fig. 2, the solid lines are the lines for the maximum of the functions $\cos kk_\beta^{(p)}\xi^\beta$ and the dashed lines represent those for the minimum of $\cos kk_\beta^{(p)}\xi^\beta$. These formations carry a momentum acting on an obstacle. Comparison with the breakdown data obtained in the above experiment enables us to find the quantity $l_{\text{res}} = 4\pi\kappa h_0$ and, hence, to determine the constant κ for copper, which, in this experiment, attained the value $\kappa \approx 1.03$.

ACKNOWLEDGMENTS

This work was supported by grant no. MK-1904.2003.01 of the President of Russian Federation; by the Program of the Council of the President of the Russian Federation for Support of Leading Scientific Schools (project nos. NSh-1481.2003.1 and NSh-1625.2003.1) and by the Russian Foundation for Basic Research (project nos. 02-01-00109 and 02-01-00613).

REFERENCES

1. S. I. Zonenko and G. G. Chernyĭ, Dokl. Akad. Nauk **390**, 46 (2003) [Dokl. Phys. **48**, 239 (2003)].
2. L. Treloar, *Physics of Elasticity of Rubber* (Izd. Inostr. Liter., Moscow, 1953).
3. A. N. Golubyatnikov, S. I. Zonenko, and G. G. Chernyĭ, Dokl. Akad. Nauk **395**, 348 (2004) [Dokl. Phys. **49**, 199 (2004)].
4. *Physics of Explosion*, Ed. by L. P. Orlenko (Fizmatlit, Moscow, 2002), Vol. 2.
5. S. K. Zhdanov and B. A. Trubnikov, *Quasi-Gaseous Unstable Media* (Nauka, Moscow, 1991).

Translated by V. Bukhanov

Doklady Physics, Vol. 49, No. 11, 2004, pp. 691–696. Translated from Doklady Akademii Nauk, Vol. 399, No. 3, 2004, pp. 347–352.

MECHANICS

Nonlinear Oscillations of a Swinging Spring

M. N. Zaripov and A. G. Petrov

Presented by Academician V.F. Zhuravlev June 15, 2004

Received June 17, 2004

INTRODUCTION

We propose to investigate nonlinear oscillations of a swinging spring by the Poincàré–Birkhoff normal-form method. As is well known, the system Hamiltonian can be represented using this method [1, 2] as a quadratic (unperturbed) part and a sum of terms with a power higher than two. Using the canonical transformations, the Hamiltonian system can be simplified in a manner such that it becomes integrable up to the fourth-order terms and higher. Thus, we obtain an asymptotic solution to the nonlinear problem. Conventional normalization methods for a system with two degrees of freedom are very cumbersome and require time-consuming calculations [2–6]. The change of variables is performed either with the help of generating functions or using a generating Hamiltonian.

In this study, we use the definition of the invariant normal form given by Zhuravlev [7, 8], which requires no separation into autonomous–nonautonomous or resonant–nonresonant cases and is realized in the framework of a unified approach. The asymptotic behavior of the normal form is obtained by consecutive calculation of quadratures. In contrast to the Zhuravlev method, we employ a parameterized generating function [9, 10] instead of the generator method and the generating Hamiltonian.

DESCRIPTION OF THE INVARIANT-NORMALIZATION ALGORITHM

First, we give definitions necessary for the desired algorithm. The function $f(t)$, representable as a finite sum of harmonics,

$$f(t) = f_0 + \sum_i (a_i \cos\omega_i t + b_i \sin\omega_i t),$$

is called the quasiperiodic function.

We introduce two linear operators $L(f)$ and $L_1(f)$ defined on the set of quasi-periodic functions $f(t)$,

$$L(f(t)) = f_0, \quad L_1(f(t)) = \sum_i \frac{b_i}{\omega_i}. \tag{1}$$

Let the Hamiltonian be given as:

$$H(\mathbf{q}, \mathbf{p}, \varepsilon) = H_0(\mathbf{q}, \mathbf{p}) + F(\mathbf{q}, \mathbf{p}, \varepsilon),$$

$$F(\mathbf{q}, \mathbf{p}, \varepsilon) = \varepsilon F_1(t, \mathbf{q}, \mathbf{p}) + \varepsilon^2 F_2(\mathbf{q}, \mathbf{p}) + \ldots,$$

which needs to be reduced to the normal form. Then, for determining the normal form,

$$\bar{H}(\mathbf{Q}, \mathbf{P}) = H_0(\mathbf{Q}, \mathbf{P}) + \bar{F}(\mathbf{Q}, \mathbf{P}, \varepsilon),$$

$$\bar{F}(\mathbf{Q}, \mathbf{P}, \varepsilon) = \varepsilon \bar{F}_1(\mathbf{Q}, \mathbf{P}) + \varepsilon^2 \bar{F}_2(\mathbf{Q}, \mathbf{P}) + \ldots$$

and the canonical change of variables, it is required to perform the following operations.

(*1*) To solve the Cauchy problem for the unperturbed Hamiltonian H_0 and to present it as

$$\begin{aligned} \mathbf{q} &= \mathbf{q}(t, \mathbf{X}, \mathbf{Y}), \quad \mathbf{p} = \mathbf{p}(t, \mathbf{X}, \mathbf{Y}), \\ \mathbf{q}(0, \mathbf{X}, \mathbf{Y}) &= \mathbf{X}, \quad \mathbf{p}(0, \mathbf{X}, \mathbf{Y}) = \mathbf{Y}. \end{aligned} \tag{2}$$

(*2*) To find the expansion coefficients for the normal form $\bar{F}_i$ and for the function Ψ_i:

$$\bar{F}_i(\mathbf{Q}, \mathbf{P}) = L(R_i(\mathbf{q}(t, \mathbf{Q}, \mathbf{P}), \mathbf{p}(t, \mathbf{Q}, \mathbf{P})),$$

$$\bar{\Psi}_i(\mathbf{Q}, \mathbf{P}) = L_1(R_i(\mathbf{q}(t, \mathbf{Q}, \mathbf{P}), \mathbf{p}(t, \mathbf{Q}, \mathbf{P})), \quad i = 1, 2, \ldots,$$

where the values of R_i are calculated for the ith approximation from the functions found in previous approximations. The formulas for the first two approximations are the following:

$$R_1(\mathbf{Q}, \mathbf{P}) = F_1(\mathbf{Q}, \mathbf{P}),$$

$$R_1(\mathbf{Q}, \mathbf{P}) = F_2(\mathbf{Q}, \mathbf{P}) + \frac{1}{2}\{F_1 + \bar{F}_1, \Psi_1\}.$$

(*3*) We present the formulas for constructing the solution after the first two approximations of the nor-

Institute for Problems in Mechanics,
Russian Academy of Sciences,
pr. Vernadskogo 101, Moscow, 119526 Russia
e-mail: mikezmn@mail.ru

1028-3358/04/4911-0691$26.00 © 2004 MAIK “Nauka/Interperiodica”

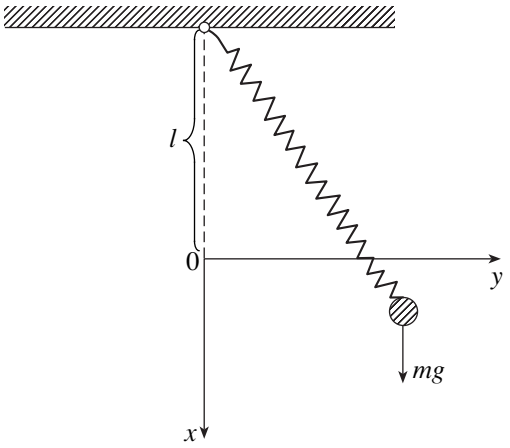

Fig. 1. Formulation of the problem. A pendulum with two degrees of freedom: a heavy point mass swinging in a vertical plane on a weightless spring.

mal form $\Psi = \varepsilon\Psi_1 = \varepsilon^2\Psi_2$ and the function $\bar{F} = \varepsilon F_1 = \varepsilon^2 \bar{F}_2$ have been found.

Let $\mathbf{X} = \mathbf{X}(t, \mathbf{Q}_0, \mathbf{P}_0)$ and $\mathbf{Y} = \mathbf{Y}(t, \mathbf{Q}_0, \mathbf{P}_0)$ be the solution to the set of equations with the Hamiltonian $\bar{F}(\mathbf{X}, \mathbf{Y})$,

$$\dot{\mathbf{X}} = \frac{\partial \bar{\mathbf{F}}}{\partial \mathbf{Y}}, \quad \dot{\mathbf{Y}} = -\frac{\partial \bar{F}}{\partial \mathbf{X}}, \quad \mathbf{X}(0) = Q_0, \quad \mathbf{Y}_0(0) = \mathbf{P}_0.$$

Then, according to the Zhuravlev theorem and using the substitution of this solution into solution (2) with the unperturbed Hamiltonian, we obtain the solution to the set with the Hamiltonian $\bar{H}(\mathbf{Q}, \mathbf{P})$:

$$\mathbf{Q} = \mathbf{q}(t, \mathbf{X}(t, \mathbf{Q}_0, \mathbf{P}_0), \mathbf{Y}(t, \mathbf{Q}_0, \mathbf{P}_0)),$$

$$\mathbf{P} = \mathbf{p}(t, \mathbf{X}(t, \mathbf{Q}_0, \mathbf{P}_0), \mathbf{Y}(t, \mathbf{Q}_0, \mathbf{P}_0)).$$

The solution in terms of the initial variables is obtained after the canonical change of the variables $\mathbf{Q}$, $\mathbf{P} \longrightarrow \mathbf{q}$, and $\mathbf{p}$ in the parametric form

$$\begin{aligned} \mathbf{q} &= \mathbf{x} - \frac{1}{2}\Psi_{\mathbf{y}}, \quad \mathbf{Q} = \mathbf{x} + \frac{1}{2}\Psi_{\mathbf{y}}, \\ \mathbf{p} &= \mathbf{y} + \frac{1}{2}\Psi_{\mathbf{x}}, \quad \mathbf{P} = \mathbf{y} - \frac{1}{2}\Psi_{\mathbf{x}}. \end{aligned} \tag{3}$$

Excluding parameters $\mathbf{x}$ and $\mathbf{y}$, we find the explicit form of the transformation of variables on the order of smallness ε^3:

$$\begin{aligned} \mathbf{q}(\mathbf{Q}, \mathbf{P}) &= \mathbf{Q} - \Psi_{\mathbf{P}}(\mathbf{Q}, \mathbf{P}) + \frac{1}{2}\{\Psi, \Psi_{\mathbf{P}}\} + \ldots, \\ \mathbf{p}(\mathbf{Q}, \mathbf{P}) &= \mathbf{P} + \Psi_{\mathbf{Q}}(\mathbf{Q}, \mathbf{P}) - \frac{1}{2}\{\Psi, \Psi_{\mathbf{Q}}\} + \ldots. \end{aligned} \tag{4}$$

FORMULATION OF THE PROBLEM ON A SWINGING SPRING

We consider a pendulum with two degrees of freedom: a heavy point mass swinging in the vertical plane on a spring (Fig. 1), the spring being weightless.

The formulation of this problem is presented, for example, in [11, 12], in which methods of investigation of the problem and certain results are described. Because of the extreme complexity of the methods, it is difficult to make a complete analysis. We here propose a solution to this problem based on the method of invariant normalization using the parametric change of variables.

We apply the following notation: k is the spring rigidity, l is the spring length in the rest position of the load, and m is the load mass. We also assume that $\omega = \sqrt{\frac{g}{l}}$ is the frequency of small oscillations for a mathematical pendulum of length l and

$$\mu = \sqrt{\frac{k}{mg} + 1}.$$

We introduce a Cartesian coordinate system with the origin at the point O (the load rest position) and with the axes directed along vertical and horizontal lines (see Fig. 4), lx and ly being the load coordinates. The spring length is lR, where

$$R = \sqrt{(1 + x)^2 + y^2}.$$

The spring tension is $T = k\left(\frac{l}{l_0}\right)R - k$, where l_0 is the length of the unloaded spring. On the other hand, $k\left(\frac{l}{l_0}\right) - k = mg$, because l is the rest-position length. Substituting $l_0 = k\left(\frac{l}{l_0}\right) = k + mg$ into expression for T, we have $T = (k + mg)R - k$. Therefore, it is clear that $\sqrt{\frac{k + mg}{ml}}$ is the frequency of load oscillations for the undeflected spring, and μ is the ratio of this frequency to ω.

The components of the force acting on the load can be written as

$$F_x = mg - \frac{T(1 + x)}{R}, \quad F_y = -\frac{Ty}{R}.$$

The Newton equations of motion are

$$ml\ddot{x} = F_x, \quad ml\ddot{y} = F_y.$$

We also introduce dimensionless time τ,

$$\tau = \omega t, \quad \omega = \sqrt{\frac{g}{l}}.$$

Then, the equations are written in the form

$$\frac{d^2x}{d\tau^2} = -\mu^2 x - (\mu^2 - 1)\left(1 - \frac{\partial R}{\partial x}\right),$$

$$\frac{d^2y}{d\tau^2} = -\mu^2 y + (\mu^2 - 1)\frac{\partial R}{\partial y}.$$

Assuming $u = \frac{dx}{d\tau}$ and $v = \frac{dy}{d\tau}$, we pass to the set of first-order equations, which turns out to be the Hamiltonian set,

$$\frac{dx}{d\tau} = \frac{\partial H}{\partial u}, \quad \frac{du}{d\tau} = -\frac{\partial H}{\partial x}, \quad \frac{dy}{d\tau} = \frac{\partial H}{\partial v}, \quad \frac{\partial v}{\partial \tau} = -\frac{\partial H}{\partial y}$$

with the Hamiltonian

$$H = \frac{1}{2}(u^2 + v^2) + \frac{\mu^2}{2}(R^2 - 1) - (\mu^2 - 1)(R - 1) - x.$$

The constant in H is chosen in such a manner that $H(0, 0, 0) = 0$.

We study spring motion near the rest position at large times τ.

After replacement of x, y, u, and v by εx, εy, εu, and εv and H by $\varepsilon^2 H$, the Hamiltonian set remains in the previous form, whereas H is transformed into

$$H = H_0 + \varepsilon F_1 + \varepsilon^2 F_2 + O(\varepsilon^3),$$

$$H_0 = \frac{1}{2}(u^2 + v^2 + \mu^2 x^2 + y^2), \quad F_1 = \frac{1}{2}(\mu^2 - 1)xy^2,$$

$$F_2 = \frac{1}{2}(\mu^2 - 1)\left(\frac{y^4}{4} - x^2y^2\right).$$

THE NORMAL FORM

According to the algorithm described, we find the general solution to the unperturbed set with the Hamiltonian H_0,

$$x(t) = X\cos\mu t + \frac{U}{\mu}\sin\mu t, \quad y(t) = Y\cos t + V\sin t,$$
$$u(t) = U\cos\mu t - \mu X\sin\mu t, \quad v(t) = V\cos t - Y\sin t. \tag{5}$$

First approximation. We substitute the solution to the unperturbed set into the function $R_1 = F_1 = \frac{\mu^2 - 1}{2} xy^2$. As a result, we obtain the quasiperiodic (with respect to time) function $R_1(t, X, Y, U, V)$. Then, using the operators L and L_1, we find the normal form and the function Ψ in a first approximation:

$$\bar{F}_1 = L(R_1(t, X, Y, U, V)) = 0,$$

$$\Psi_1 = L_1(R_1(t, X, Y, U, V)) \tag{6}$$

$$= \frac{(\mu^2 - 1)(-2UV^2 - 2VXY\mu^2 + UY^2(\mu^2 - 2))}{2\mu^2(\mu^2 - 4)}.$$

Second approximation. We find the function $R_2 = F_2 + \frac{1}{2}\{F_1, \Psi_1\}$, where the braces correspond to the Poisson brackets $\{f, q\} = f_u g_x + f_v g_y - f_x g_u - f_y g_v$. As a result, we arrive at

$$\frac{R_2(x, y, u, v)}{\mu^2 - 1} = \frac{1}{2}\left(\frac{y^4}{4} - x^2y^2\right) + \frac{\mu^2 - 1}{8(\mu^4 - 4\mu^2)}$$
$$\times[-y^4\mu^2 + 2y^2v^2 + 2y^4 + 4x^2y^2\mu^2 + 8xyuv].$$

Instead of the arguments x, y, u, and v, we substitute the solution of unperturbed set (5). Then, we obtain the quasiperiodic (with respect to time) function $R_2(t, X, Y, U, V)$. The values of the operators $L(R_2)$ and $L_1(R_2)$ determine the next approximation of the normal form,

$$\bar{F}_2 = L(R_2(t, X, Y, U, V))$$
$$= \frac{3(\mu^2 - 1)(\mu^2X^2 + U^2)(Y^2 + V^2)}{8\mu^2(\mu^2 - 4)}$$
$$- \frac{(\mu^2 - 1)(8 + \mu^2)(Y^2 + V^2)^2}{64\mu^2(\mu^2 - 4)},$$

$$\Psi_2 = L_1(R_2(t, X, Y, U, V)) = \frac{-1}{64\mu^2(\mu^2 - 4)} \tag{7}$$
$$\times(8UV^2X + 16U^2VY - 8V^3Y + 40UXY^2$$
$$- 8VY^3 + 16UV^2X\mu^2 - 40U^2VY\mu^2 + 7V^3Y\mu^2$$
$$+ 32VX^2Y\mu^2 - 64UXY^2\mu^2 + VY^3\mu^2$$
$$+ V^3Y\mu^4 - 8VX^2Y\mu^4 + 7VY^3\mu^4).$$

AN INTEGRAL FOR THE SET OF EQUATIONS OF THE NORMAL FORM

We integrate the set in new variables X, Y, U, and V with the Hamiltonian $H_0(X, Y, U, V) + \bar{F}(X, Y, U, V)$. It follows from the Zhuravlev theorem that it is sufficient

to find the integral of the set with the Hamiltonian $\bar{F} = \varepsilon^2 F_2(X, Y, U, V)$. The set of equations for it has the form

$$\dot{X} = \frac{\omega_1}{\mu}U, \quad \dot{U} = -\mu\omega_1 X,$$

$$\dot{Y} = \omega_2 V,$$

$$\dot{V} = -\omega_2 Y,$$

$$Y^2 + V^2 = A, \quad \mu^2 X^2 + U^2 = B,$$

$$\omega_1 = A\frac{3(\mu^2-1)\varepsilon^2}{4\mu(\mu^2-4)},$$

$$\omega_2 = -B\frac{3(\mu^2-1)\varepsilon^2}{4\mu^2(\mu^2-4)} + A\frac{(\mu^2-1)(\mu^2+8)\varepsilon^2}{16\mu^2(\mu^2-4)}.$$

It is easy to verify that this set has two integrals, $Y^2 + V^2 = A$ and $\mu^2 X_2 + U^2 = B$. Therefore, we obtain a linear set with constant coefficients (to be more precise, with time-independent coefficients):

$$\ddot{X} + \omega_1^2 X = 0, \quad \ddot{Y} + \omega_2^2 Y = 0.$$

Its solution has the form

$$X = x_0\cos\omega_1 t + \frac{u_0}{\omega_1}\sin\omega_1 t,$$

$$U = -x_0\omega_1\sin\omega_1 t + u_0\cos\omega_1 t,$$

$$Y = y_0\cos\omega_2 t + \frac{v_0}{\omega_2}\sin\omega_2 t,$$

$$V = -y_0\omega_2\sin\omega_2 t + v_0\cos\omega_2 t.$$

To obtain the complete solution, it is sufficient to substitute the found functions into solution (5) of the unperturbed set. Thus, the solution is constructed with an accuracy to $O(\varepsilon^3)$. We write the final solution with the transformed variables X and Y with the initial conditions $X(0) = X_0$, $\dot{X}(0) = 0$, $Y(0) = Y_0$, and $\dot{Y}(0) = 0$ as

$$X = X_0\left(\cos\omega_1 t\cos\mu t - \frac{\omega_1}{\mu}\sin\omega_1 t\sin\mu t\right),$$

$$Y = Y_0(\cos\omega_2 t\cos t - \omega_2\sin\omega_2 t\sin t).$$

In the initial variables x and y, the law of motion is obtained by transforming the formulas for $X, Y \longrightarrow x, y$ into parametric form (3) or explicit form (4), in which the function Ψ is determined from the expansion $\Psi = \varepsilon\Psi_1 + \varepsilon^2\Psi_2 + \ldots$ with expansion coefficients given by (6) and (7).

THE RESONANCE CASE

We assume that $\mu^2 = 4$. Then, the expansion for the Hamiltonian of the initial set is

$$H = H_0 + \varepsilon F_1 + O(\varepsilon^2),$$

$$H_0 = \frac{1}{2}(u^2 + v^2 + 4x^2 + y^2), \quad F_1 = \frac{3}{2}xy^2 + 2x^2.$$

Here, the above algorithm is used. First, we find the general solution to the unperturbed set with the Hamiltonian H_0,

$$x(t) = X\cos 2t + \frac{U}{2}\sin 2t, \quad y(t) = Y\cos t + V\sin t,$$
$$u(t) = U\cos 2t - 2X\sin 2t, \quad v(t) = V\cos t - Y\sin t. \tag{8}$$

First approximation. We substitute the solution to the unperturbed set into the function $R_1 = F_1 = \frac{3}{2}x(t)y(t)^2 + 2x(t)^2$. As a result, we obtain the quasiperiodic (with respect to time) function $R_1(t, X, Y, U, V)$ and, using the operators L and L_1, find the normal form and the function Ψ in the first approximation:

$$\bar{F}_1 = L(R_1(t, X, Y, U, V)) = \frac{3}{8}(-V^2X + UVY + XY^2),$$
$$\Psi_1 = L_1(R_1(t, X, Y, U, V)) \tag{9}$$
$$= \frac{3}{64}(4XYV + 3UV^2 + 5Y^2U).$$

The integral of the set. It is convenient to integrate the set in the Birkhoff variables,

$$z_1 = \frac{1}{\sqrt{2}}U + \sqrt{2}iX, \quad z_2 = V + iY. \tag{10}$$

These relations are the canonical change with the valence $2i$. The normal form of the first approximation is $\tilde{H} = \tilde{H}_0 + \tilde{F}$,

$$\tilde{H}_0 = i(2z_1\bar{z}_1 + z_2\bar{z}_2), \quad \tilde{F} = -\varepsilon\frac{3\sqrt{2}}{16}(z_1\bar{z}_2^2 - \bar{z}_1 z_2^2).$$

The set of equations for the perturbed part of the Hamiltonian is

$$\dot{z}_1 = \frac{\partial\tilde{F}}{\partial\bar{z}_1} = \varepsilon\frac{3\sqrt{2}}{16}z_2^2, \quad \dot{z}_2 = -\frac{\partial\tilde{F}}{\partial\bar{z}_2} = \varepsilon\frac{3\sqrt{2}}{8}z_1\bar{z}_2. \tag{11}$$

This set has two integrals $H_0 = \text{const}$ and $\tilde{F} = \text{const}$. The first integral corresponds to the law of conservation of energy,

$$2|z_1|^2 + |z_2|^2 = C^2, \quad (12)$$

where $2|z_1|^2$ is the energy of the first mode (horizontal oscillations) and $|z_2|^2$ is the energy of the second mode (vertical oscillations).

To obtain the equation for the second-mode energy, we differentiate it twice and substitute the derivatives $\dot{z}_1$ and $\dot{z}_2$ from Eqs. (11):

$$\frac{d|z_2|^2}{dt} = \dot{z}_2\bar{z}_2 + \dot{\bar{z}}_2 z_2 = -\varepsilon\frac{3\sqrt{2}}{8}(z_1\bar{z}_2^2 + \bar{z}_1 z_2^2),$$

$$\frac{d^2|z_2|^2}{dt^2} = -\frac{3\sqrt{2}}{8}(2\dot{z}_1\bar{z}_2^2 + 4\dot{z}_2\bar{z}_1 z_2)$$

$$= \frac{9\varepsilon^2}{32}(-|z_2|^4 + 4|z_1|^2|z_2|^2).$$

With the help of the law of conservation of energy, we obtain the equation for the second-mode energy,

$$\frac{d^2|z_2|^2}{dt^2} = \frac{9\varepsilon^2}{32}(-3|z_2|^4 + 2C^2|z_2|^2).$$

This equation can be interpreted as the motion of a point mass under the action of a force with the potential $-\Pi(|z_2|^2)$ (motion in a potential well).

The equation has the integral of energy

$$\frac{1}{2}\left(\frac{d}{dt}|z_2|^2\right)^2 + \Pi = E, \quad \Pi = \frac{9\varepsilon^2}{32}(|z_2|^6 - C^2|z_2|^4).$$

At $|z_2|^2 = \frac{2}{3}C^2$, the potential energy attains a minimum equal to $-\frac{4}{27}C^6\varepsilon^2$. For $-\frac{4}{27}C^6\varepsilon^2 < E < 0$, the second-mode energy slowly periodically oscillates. For a small difference between E and its minimal value, the frequency $\tilde{\omega}$ of these oscillations is

$$\frac{\tilde{\omega}}{\omega} = \sqrt{\Pi''\frac{2}{3}C^2} = \frac{3}{4}\varepsilon C.$$

The first-mode energy varies with the same frequency, and, by virtue of the law of conservation of energy (12), the energy is alternately pumped from one mode to the other.

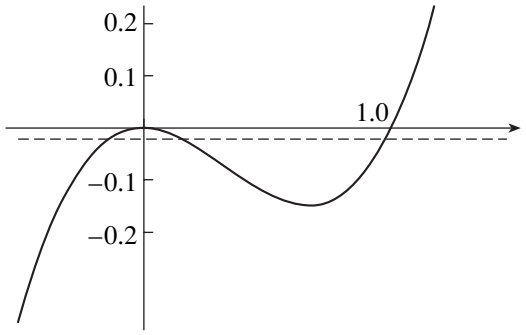

Fig. 2. Normalized potential energy for $C = 1$.

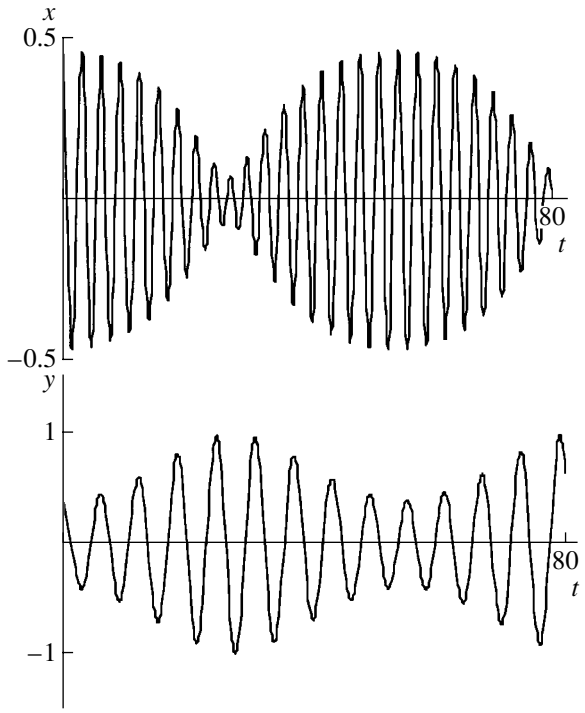

Fig. 3. Numerical solution to the normal-form equations for $X(t)$ and $Y(t)$.

In Fig. 2, we show the plot of the normalized potential energy $\frac{32\Pi}{9\varepsilon^2}$ for $C = 1$. Along the abscissa axis, we plot $|z_2|^2$. The dashed line presents an example of a typical value of the normalized energy $\frac{32E}{9\varepsilon^2} = -0.02$. Values $|z_2|^2$ of the second-mode energy are limited by two points of the intersection of solid and dashed lines. Calculating the coordinates of two extreme points, we find the energy-variation interval $0.154 < |z_2|^2 < 0.979$ for the second mode. According to the law of conservation of energy (12), the energy-variation interval for the first mode is $0.021 < 2|z_1|^2 < 0.846$.

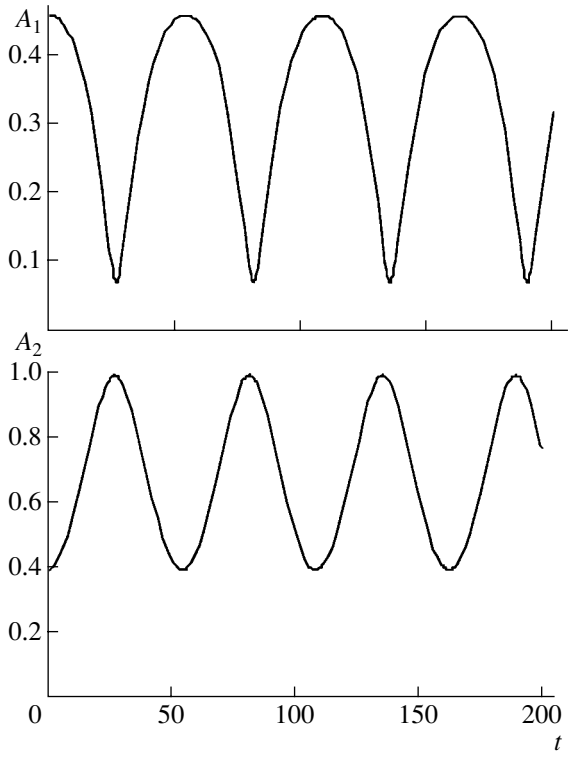

Fig. 4. Amplitudes A_1 and A_2 as functions of time.

In Fig. 3, we show the solution to the set of equations of the normal form for $X(t)$ and $Y(t)$ at $\varepsilon = 0.2$ with the initial data

$$X(0) = 0.46, \quad Y(0) = 0.392, \quad \dot{X}(0) = 0,$$
$$\dot{Y}(0) = 0.$$

These values correspond to the above values of constants C and E.

In Fig. 4, we show the dependences of amplitudes $A_1 = \sqrt{2}\,z_1 = \sqrt{X^2 + \frac{1}{4}U^2}$ and $A_2 = |z_2| = \sqrt{Y^2 + V^2}$ for the same example. According to the law of conservation of energy, the amplitudes are linked by the relation $4A_1^2 + A_2^2 = C^2$. The amplitudes vary within the range $0.07 < A_1 < 0.46$ and $0.392 < A_2 < 0.989$.

Figures 1–4 show how the energy of oscillations is pumped from one degree of freedom X to the other Y at the resonance of frequencies.

ACKNOWLEDGMENTS

The authors are grateful to V.F. Zhuravlev for fruitful discussions of the results obtained in the present study.

REFERENCES

1. A. Poincaré, *Selected Papers (in Three Volumes)* (Nauka, Moscow, 1972), Vol. 2.
2. J. D. Birkhoff, *Dynamical Systems* (Gostekhizdat, Moscow–Leningrad, 1941).
3. A. D. Brunot, *Limited Problem of Three Bodies* (Nauka, Moscow, 1990).
4. V. I. Arnold, *Mathematical Methods of Classical Mechanics* (Editorial URSS, Moscow, 2000).
5. V. I. Arnold, *Additional Chapters in Theory of Ordinary Differential Equations* (Nauka, Moscow, 1978).
6. V. I. Arnold, V. V. Kozlov, and A. I. Neishtadt, *Mathematical Aspects of Classical and Celestial Mechanics. Results of Science and Engineering. Modern Problems in Mathematics. Dynamical Systems* (VINITI, Moscow, 1985).
7. V. F. Zhuravlev, *Principles of Theoretical Mechanics* (Nauka, Moscow, 1997).
8. V. F. Zhuravlev, Prikl. Mat. Mekh. **66**, 356 (2002).
9. A. G. Petrov, Prikl. Mat. Mekh. **66**, 948 (2002).
10. A. G. Petrov, Dokl. Akad. Nauk **386**, 482 (2002) [Dokl. Phys. **47**, 742 (2002)].
11. V. N. Bogaevskiĭ and A. Ya. Povzner, *Algebraic Methods in Nonlinear Theory of Perturbations* (Nauka, Moscow, 1987).
12. A. H. Nayfeh, *Perturbation Methods* (J. Wiley, New York, 1973; Mir, Moscow, 1976).

Translated by V. Bukhanov